

ABSTRACT

Title of Dissertation: Novel Organic Polymeric and Molecular
Thin-Film Devices for Photonic Applications

Younggu Kim, Doctor of Philosophy, 2006

Dissertation directed by: Professor Chi H. Lee
Department of Electrical and
Computer Engineering

The primary objective of this thesis is to explore the functionalities of new classes of novel organic materials and investigate their technological feasibilities for becoming novel photonic components.

First, we discuss the unique polarization properties of optical chiral waveguides. Through a detailed experimental polarization analysis on planar waveguides, we show that eigenmodes in planar chiral-core waveguides are indeed elliptically polarized and demonstrate waveguides having modes with polarization eccentricity of 0.25, which agrees very well with recent theory. This is, to the best of our knowledge, the first experimental demonstration of the mode ellipticities of the chiral-core optical waveguides. In addition, we also examine organic magneto-optic

materials. Verdet constants are measured using balanced homodyne detection, and we demonstrate organic materials with Verdet constants of 10.4 and 4.2 rad/T · m at 1300 nm and 1550 nm, respectively.

Second, we present low-loss waveguides and microring resonators fabricated from perfluorocyclobutyl copolymer. Design, fabrication and characterization of these devices are addressed. We demonstrate straight waveguides with propagation losses of 0.3 dB/cm and 1.1 dB/cm for a buried channel and pedestal structures, respectively, and a microring resonator with a maximum extinction ratio of 4.87 dB, quality factor $Q = 8554$, and finesse $\mathcal{F} = 55$. In addition, from a microring-loaded Mach-Zehnder interferometer, we demonstrate a modulation response width of 30 ps and a maximum modulation depth of 3.8 dB from an optical pump with a pulse duration of 100 fs and a pulse energy of 500 pJ when the signal wavelength is initially tuned close to one of the ring resonances.

Finally, we investigate a highly efficient organic bulk heterojunction photodetector fabricated from a blend of P3HT and C₆₀. The effect of multilayer thin film interference on the external quantum efficiency is discussed based on numerical modeling. We experimentally demonstrate an external quantum efficiency $\eta_{\text{EQE}} = 87 \pm 2\%$ under an applied bias voltage $V = -10$ V, leading to an internal quantum efficiency $\eta_{\text{IQE}} \approx 97\%$. These results show that the charge collection efficiency across the intervening energy barriers can indeed reach near 100% under a strong electric field.

Novel Organic Polymeric and Molecular Thin-Film Devices
for Photonic Applications

by

Younggu Kim

Dissertation submitted to the Faculty of the Graduate School of the
University of Maryland, College Park in partial fulfillment
of the requirements for the degree of
Doctor of Philosophy
2006

Advisory Committee:

Professor Chi H. Lee, Advisor/Chair
Doctor Warren N. Herman, Co-advisor
Professor Julius Goldhar
Professor Christopher C. Davis
Professor James R. Anderson

© Copyright by

Younggu Kim

2006

DEDICATION

To the loving memory of my father,
and my mother

ACKNOWLEDGMENTS

I am truly grateful for the advice, support, friendship, criticism, and collaboration that I have received over the years during my graduate study at the University of Maryland and my research on polymer photonics at the Laboratory for Physical Sciences. LPS has been a really fascinating place to conduct research because of the wonderful facilities and equipment as well as the many talented scientists and engineers.

First of all, I am particularly indebted to Prof. Chi Lee for his advice throughout my Ph.D research, and the tremendous amount of support and encouragement when I would get stuck. His great enthusiasm for research and for playing tennis impressed me often considering his age, and he sometimes reminded me of my father who would be the same age as he. I am deeply grateful to Dr. Warren Herman at the LPS who introduced me to this wonderful area of research on polymer photonics and optoelectronics. He has been extremely patient in answering my countless questions. Without a doubt, every single piece of knowledge on organic polymer optics I have acquired has benefited from daily interaction with him. Along the way of my Ph.D study, I was lucky enough to have a second academic advisor, Prof. Julius Goldhar. I am grateful for his fruitful insights and comments on the experiments I have conducted. I will miss his sense of humor as well. I

am also grateful to Prof. Chris Davis and Prof. Bob Anderson who agreed to serve on my dissertation committee. When I was new to optics, I learned a lot through classes I took from Prof. Davis. He was also generous enough to extend my final exam when I had to go back to Korea for my father’s funeral.

I also would like to thank Prof. Victor Granastein who gave me a research opportunity for the first year of my graduate study. He is a genuine gentleman whom everybody loves. I deeply appreciate his support even after I left his group. I have also benefited from many stimulating discussions with Prof. Tom Murphy on a few numerical simulations. His Matlab codes were exceptionally helpful to design ring resonator devices. In addition, his class on “Optical Communication Systems” was definitely the best among the classes I took at the University of Maryland. I also want to thank Dr. Danilo Romero, an expert on organic optoelectronic devices. He not only fabricated a series of devices for my research but also patiently taught me a lot on the physics of organic semiconductors.

All the thesis work described here would not have been possible without the support and encouragement of my colleagues at the University of Maryland and LPS: Toby Olver, Dan Hinkel, Steve Brown, Scott Horst, Lisa Lucas, Sal Martinez, Mike Khbeis, George de la Vergne, J.B. Dottellis, Russell Frizzell, Leslie Lorenz, Mark Thornton, Greg Latini, Dr. Chris Richardson, Dr. Charles Krafft, Prof. P. T. Ho, Dr. Rohit Grover, Dr. Vien Van, Dr. Kuldeep Amarnath, Victor Yun, Dr. Yongzhang Leng, Dr. Paul Petruzzi, Dr. Wei-Lou Cao, Dr. Jungwhan Kim, Min Du, and Yi-Hsing Peng, and more. Special thanks go to cleanroom manager

Toby who has never turned down my request for help and made my work in the cleanroom a lot easier, Dan who was truly helpful for device fabrication and SEM-ing, Steve whom I bothered almost every day for stepper use, Dr. Cao who helped me conduct various experiments, and Dr. Krafft who provided useful tips on the experimental setup to measure the Faraday rotation.

Most of the work in my thesis has been done in strong collaboration with other researchers outside of the University of Maryland and LPS. I would like to thank Prof. Mark Green, Dr. Myungjin Lee and Dr. Henry Teng at N.Y. Polytechnic University, Prof. Andrzej Rajca at the University of Nebraska, Prof. Lin Pu at the University of Virginia, Prof. Dennis Smith and Shengrong Chen at Clemson University, Prof. Seth Marder at Georgia Tech, Dr. Cheng Zhang at Norfolk University, Dr. William Diffey at the US Army, Dr. Andy Guenthner at NAWC China Lake.

I am grateful to Shuo-Yen Tseng, Glenn Hutchinson, Mike Bowen, Ricardo Pizarro, Dyan Ali, Arthur Liu, and more, especially to Shuo-Yen and Glenn for the time we spent together not only at LPS but also at Hard Times and Starbucks. I will particularly miss the happy hour a lot. I also would like to thank several fellow Korean friends in the department including Dong Hun Park, Soo Bum Lee, Woochul Jeon, Jusub Kim, and Seokjin Kim for the occasional wonderful parties and the time we spent on the tennis court, and Kyuyong Lee, Jeong-Nam Kim, Kiyong Kim, Seungjoon Lee, Joonhyuk Yoo, Seung-Jong Baek, Kyechong Kim, Sangchul Song, Inseok Choi, Hojin Kee, Jookyung Lee, and many more for their friendship. My graduate study would not have been nearly as much fun without

them. Additionally, I want to thank Jeong-II Oh who did not mind driving down here from Boston when I was frustrated from work or life.

Most of all, I am deeply indebted to my family for their love, encouragement, and support (including monetary support, as ‘indebted’ means in a dictionary) over the years. No matter how many words I put here, it will never be sufficient to express my true gratefulness to my dad in heaven, mom, parents-in-law, brother, and sister. Finally, I would like to gratefully acknowledge Soyeon and Minju for their constant love, sacrifice, and tolerance of my irregular hours at home.

TABLE OF CONTENTS

Acknowledgments	iii
List of Figures	x
List of Abbreviations	xviii
1 Introduction	1
1.1 Motivation	1
1.2 Scope of thesis	3
2 Optical Chiral Waveguide	8
2.1 Organic chiral material and optical activity	8
2.2 Unique polarization properties of chiral-core planar waveguides . . .	11
2.2.1 Fields in bulk chiral media	12
2.2.2 Eigenmodes in asymmetric chiral planar waveguides	15
2.3 Chiral waveguides from amorphous binaphthyl films	25
2.4 Experimental polarization analysis	34
2.5 Other chiral materials	48

2.5.1	Binaphthyl polymer	49
2.5.2	Polymethine dyes	50
2.5.3	(7)Helicene	52
2.5.4	Bridged binaphthyl with chromophore	52
2.6	Summary	53
3	Organic Magneto-Optic Material	55
3.1	Magneto-optic effect	55
3.2	Balanced homodyne detection	58
3.3	Measurement of Verdet constant	63
3.4	Summary	72
4	Optical Waveguide and Microring Resonator from PFCB	74
4.1	Perfluorocyclobutyl (PFCB) copolymer	74
4.2	Low loss optical waveguide from PFCB copolymer	75
4.2.1	Eigenmodes in dielectric waveguides	77
4.2.2	Fabrication of PFCB waveguides	80
4.2.3	Loss measurement of straight waveguides	84
4.3	PFCB Microring resonators	87
4.3.1	Basic principles	88
4.3.2	Design considerations	94
4.3.3	Experimental characterization	100
4.3.4	Ultrafast all-optical switching experiment	106

4.4	Summary	114
5	Organic Thin-Film Photodetector based on Bulk Heterojunction	117
5.1	Basic principles	118
5.2	Fabrication of bulk heterojunction PDs	126
5.3	Device characteristics	131
5.4	Multilayer thin film interference effects	138
5.4.1	Optical properties of individual layers	138
5.4.2	Effect of multilayer thin film interference	140
5.5	Improvement of the external quantum efficiency	152
5.6	Summary	156
6	Conclusions	158
6.1	Summary and accomplishments	158
6.2	Future work	161
	Bibliography	165

LIST OF FIGURES

2.1	Structure of an asymmetric planar waveguide with an isotropic chiral core	16
2.2	Calculation of the mode effective index n_{eff} vs. waveguide thickness d	20
2.3	Calculation of the mode eccentricity parameter g vs. chirality γ for the lowest order elliptical modes, RHE ₀ and LHE ₀	23
2.4	Chemical structure of the single molecule binaphthyls, ML-224 and ML-226.	26
2.5	Optical rotatory dispersion (ORD) curves for ML-224 and ML-226 measured in solution.	27
2.6	Index of refraction dispersion measured with a Metricon TM for ML-224 and ML-226	28
2.7	Experimental setup for measurement of optical rotatory power.	29
2.8	Structure of chiral slab waveguides on GaAs substrates coated with SiON.	30

2.9 Calculation of n_{eff} with increasing waveguide core thickness, (a) ML-224 and (b) ML-226	32
2.10 Calculation of mode ellipticity of RHE_0 and LHE_0 of the asymmetric slab waveguide as a function of given material chirality γ	33
2.11 Experimental setup for polarization analysis for chiral waveguide.	35
2.12 Detected optical power as a function of rotating quarter waveplate orientation.	38
2.13 Continuous evolution of the polarization states on the Poincare sphere.	40
2.14 Evolution of polarization through the chiral waveguide fabricated from ML-224 and ML-226.	44
2.15 Calculation of mode ellipticity of RHE_0 and LHE_0 as a function of given material chirality γ for a symmetric and asymmetric chiral-core planar waveguides.	47
2.16 Chemical structure of the main chain binaphthyl polymer, Zhang-IV-37 with $\text{R} = \text{n-C}_6\text{H}_{13}$	49
2.17 Index of refraction dispersion measured with a Metricon TM for the polybinaphthyl Zhang-IV-37	50
2.18 UV-Vis-IR spectra measured with a Cary 5000 spectrophotometer for HT-dye14 in poly(butyl methacrylate-co-methyl methacrylate) copolymer.	51

3.1	Schematics of balanced homodyne detection.	60
3.2	Normalized intensities along the principal axes I_1 , I_2 , and difference $I_1 - I_2$	60
3.3	Experimental setup of balanced homodyne detection to measure the Verdet constant.	64
3.4	Calibration of the amplitude of alternating magnetic flux density inside the Helmholtz coil.	65
3.5	Optical bias curve without magnetic field applied for a 2 cm-long rod of TGG sample obtained at wavelength 633 nm	67
3.6	Faraday rotation measured from a 2 cm long rod of TGG at a wavelength of 633 nm by varying magnetic field flux densities and a fit to linear line.	68
3.7	Faraday rotation measured for a 2 cm-long rod of TGG at different wavelengths	68
3.8	Chemical structure of SJZ-87A	69
3.9	UV-Vis-IR transmission spectra measured with a Cary 5000 spectrophotometer for organic magneto-optic samples provided by Georgia Tech.	70
3.10	Faraday rotation measured for the substrates only and for the sample labelled SJZ-87A at wavelengths of 1300 nm and 1550 nm.	71

3.11	Faraday rotation measured for the substrates only and for the samples labelled TK1V1292A320-A and TK1V1292A320-N at a wavelength of 850 nm.	71
4.1	Thermal (a)polymerization and (b)copolymerization to PFCB-based polymer from trifluorovinylaryl ether monomers	76
4.2	Mode profile of the transverse electric field component $ e_x $ for the fundamental TE mode for a pedestal and buried channel	79
4.3	Outline of process steps to fabricate the PFCB waveguides.	82
4.4	Scanning electron micrograph of the PFCB pedestal waveguide.	85
4.5	Loss measurement of PFCB straight waveguides using cutback method for TE mode.	86
4.6	Schematic diagram of microring resonators. (a) all-pass and (b) add-drop configuration.	88
4.7	Calculation of a typical spectral response of all-pass filter.	91
4.8	Calculated phase response near a resonance in all-pass configuration	92
4.9	Calculation of a typical spectral response of add-drop filter	93
4.10	3D full vectorial calculation for bending loss.	96
4.11	Cross-sectional mode profile of two parallel waveguides separated by an edge-to-edge distance g	98
4.12	Calculation of coupling constant between two PFCB pedestal waveguides as a function of waveguide separation g	99

4.13	Scanning electron micrograph of PFCB ring resonator, with a radius $R = 25 \mu\text{m}$, and a coupling gap $g = 0.45 \mu\text{m}$	102
4.14	Experimental setup for microring characterization.	103
4.15	Measured spectral response at the drop port of a add-drop filter with a radius $25 \mu\text{m}$ with ASE input	104
4.16	Normalized signal of the device at the throughput and drop port at the resonance at 1531.05 nm from a tunable laser input.	105
4.17	(a) Resonance shift with increasing ASE input power. Maximum resonance shift 25 pm obtained. (b) Thermo-optic coefficient, $\text{d}n/\text{dT}$, measured using a Metricon TM that was custom outfitted with temperature control.	107
4.18	Schematic picture of all-optical switching experiment.	109
4.19	Spectral response of an MR-MZI with a length imbalance between two arms of the MZI.	111
4.20	Measured switching response of the MR-MZI from a optical pump, a 100 fs Ti:Sapphire laser pulse	113
4.21	Calculated phase response near a resonance in all-pass configuration when the ring is lossy and under-coupled	115
5.1	Schematic drawing illustrating photoinduced charge transfer between a conjugated polymer (P3HT) and a fullerene (PCBM-C ₆₀).	119

5.2	(a) Schematic energy level diagram of electrodes, donor and acceptor material (b) Schematic illustration of photocurrent generation in heterojunction PV cells and detectors.	122
5.3	Schematic diagram depicting conceptually the photoinduced charge transfer in (a)bilayer heterojunction and (b)bulk heterojunction . .	124
5.4	The chemical structure of the materials in bulk heterojunction layer for organic photodetector	127
5.5	Schematic diagram of the device configuration.	128
5.6	Atomic force microscopy (AFM) images for four different PCBM-C ₆₀ molar fractions x	130
5.7	Current density versus voltage (I - V) characteristics of the bulk heterojunction device of MEH-PPV copolymer and PCBM-C ₆₀ with a C ₆₀ molar fraction $x = 0.57$	133
5.8	Absorption spectra of the blend of P3HT/PCBM-C ₆₀	135
5.9	I - V characteristics of the bulk heterojunction device from P3HT and PCBM-C ₆₀ with a C ₆₀ /P3HT 1.1 in weight, (a) under AM 1.5 direct solar illumination (b) under different laser intensities at 532 nm. .	136
5.10	External quantum efficiency vs. bias voltage of the device of P3HT/PCBM-C ₆₀ at wavelength of 532 nm	137

5.11 (a) Real and imaginary index of refraction measured from the spectroscopic ellipsometric data and model fit with the Drude-Lorentz model. (b) Comparison between the estimated transmission using the n and k , and thickness from the best-fit model and the measured transmission from a spectrophotometer.	141
5.12 Optical properties of Al, PEDOT:PSS, and P3HT:C ₆₀	142
5.13 Schematic diagram of the multilayer device structure with the thicknesses and the optical electric fields in each layer, \mathbf{E}_i^+ and \mathbf{E}_i^-	143
5.14 Calculation of reflectivity R_D and absorption $A_D = 1 - R_D - T_D$ of the bulk heterojunction device of P3HT/C ₆₀ with a thickness of 100 nm.	147
5.15 Calculation of field distribution $ \mathbf{E}(x) ^2$ as a function of position. Modulus squared of the optical electric field $ \mathbf{E}(x) ^2$ is normalized to the incident light field $ \mathbf{E}_0^+ ^2$	148
5.16 Calculation of time-averaged absorbed power $Q(x)$ as a function of position.	150
5.17 Calculation of field distribution $ \mathbf{E}(x) ^2$ and time-averaged absorbed power $Q(x)$ as a function of position for the device structure of glass/ITO/P3HT:C ₆₀ /Al.	153
5.18 UV-Vis-IR transmission spectra for P3HT:C ₆₀ samples with three different thicknesses.	154

LIST OF ABBREVIATIONS

TE	Transverse electric
TM	Transverse magnetic
RHC	Right-handed circular
LHC	Left-handed circular
RHE	Right-handed elliptical
LHE	Left-handed elliptical
SOP	State of polarization
PECVD	Plasma enhanced chemical vapor deposition
RIE	Reactive ion etching
ICP-RIE	Inductive coupled plasma RIE
SEM	Scanning electron microscope
TGG	Terbium gallium garnet
PFCB	Perfluorocyclobutyl
BCB	Bisbenzocyclobutene
CTE	Coefficient of thermal expansion
FD	Finite difference
PDL	Polarization dependent loss

PML	Perfectly matched layer
OCDF	Optical channel dropping filter
OADF	Optical add-drop filter
MZI	Mach-Zehnder interferometer
MR-MZI	Microring-loaded Mach-Zehnder interferometer
ASE	Amplified spontaneous emission
EDFA	Erbium doped fiber amplifier
FWHM	Full width at half maximum
OPV	Organic photovoltaic
OPD	Organic photodetector
HOMO	Highest occupied molecular orbital
LUMO	Lowest unoccupied molecular orbital
OLED	Organic light emitting diode
EQE	External quantum efficiency
ICPE	Incident photon to current conversion efficiency
IQE	Internal quantum efficiency
PCE	Power conversion efficiency
ITO	Indium tin oxide
P3HT	Poly(3-hexylthiophene-2,5-diyl)
PCBM-C ₆₀	[6,6]-phenyl-C ₆₁ -butyric acid methyl ester
PEDOT	Poly(3,4-ethylenedioxythiophene)
PSS	Poly(styrenesulfonate)

CHAPTER 1

INTRODUCTION

1.1 Motivation

Organic polymers and molecules have emerged as one of the most promising class of materials for photonic and electronic applications due to their potential capabilities and advantages such as moderate to high functionality, fabrication flexibility, substrate compatibility, affordability, etc. While other material systems, such as inorganic semiconductors (e.g., silicon, gallium arsenide, and indium phosphide, etc.), glasses (e.g., silicon dioxide, silicon oxynitride, and silicon nitride, etc.), silicon on insulator (SOI), lithium niobate, sol-gels, etc. have widely been used, organic materials have become a new paradigm for various components in communication systems, displays, sensors, solar cells, and so on. During the past decade, there has been an explosive growth and development of both materials and devices. Representative examples include waveguide based integrated-optic devices for essential building blocks for optical communication systems based on linear/nonlinear optical properties of the materials: interconnectors, polarization converters, filters, switches, directional couplers, modulators, gratings [1, 2]. They also include opto-electronic and electronic devices based on electroluminescent and (semi)conducting

properties of the materials: LEDs, photodetectors, photovoltaic cells, lasers, radio-frequency identification (RFID) tags, field effect transistors (FETs) [3, 4].

Organic materials have great advantages in many aspects because of the ability to change the material properties synthetically by modifications in chemical structure and composition. Advantages include:

- tunability of index of refraction (range of 1.3 – 2) and birefringence control
- low coupling loss from and to the fiber due to small Fresnel reflection and mode mismatch
- low absorption loss at common telecommunication wavelength, 1310 nm and 1550 nm
- large class of 2nd and 3rd order nonlinear optical properties
- various optoelectronic properties such as photoluminescence, electroluminescence, and (semi)conductivity
- easily formed into thin films via spin-coating, inkjet printing, dipping, etc.
- wide variety of substrate compatibility, such as glass, quartz, semiconductor, printed circuit board, and even flexible ones
- fabrication flexibility – photolithography as well as non-conventional lithography such as laser ablation, nano-imprinting, multi-photon absorption, etc.

- affordability – inexpensive materials, simple fabrication processes, and fast turn-around time

On the other hand, organic devices have drawbacks in terms of environmental performance and reliability, such as thermal aging and photo-oxidation. Many research groups, including electrical engineers, chemists, and physicists, have been making efforts to overcome such problems through further chemical modification and extensive reliability testing, such that devices in some applications are already in the market (OLED, for example) and some are soon to be commercially available.

New classes of organic materials for various applications are synthesized every day. The primary objective of this thesis is to explore the functionalities of those materials and investigate their technological feasibilities for constructing novel photonic components.

1.2 Scope of thesis

This thesis is separated into three principal parts discussing different types of devices that are somewhat independent of each other, but can be integrated into single devices: chiral waveguides and magneto-optic materials, low-loss waveguides and microring devices from perfluorinated polymer, and organic bulk heterojunction photodetectors.

Chapter 2 will discuss the unique polarization properties of optical chiral waveguides that can be used for integrated-optic polarization converters or polarization modulators provided that low loss amorphous films of sufficient chirality can be

fabricated. In an achiral film, as is well known, the modes are transverse electric (TE) and transverse magnetic (TM). On the other hand, new modeling results for (a)symmetric planar waveguides with chiral cores showed that the eigenmodes are elliptically polarized modes, in general, with the polarization ellipticity depending on the chirality, which is related to the bulk rotatory power of material. For an important design consideration, dependence of mode ellipticity on cladding index is also discussed, and we propose and demonstrate a SiON layer for a cladding layer. Through a detailed experimental polarization analysis on asymmetric chiral-core planar waveguides fabricated from binaphthyl-based organic single molecules, the eigenmodes of chiral planar waveguides are characterized and their mode ellipticities are compared with the ones predicted in recent theory. We show that eigenmodes in planar chiral-core waveguides are indeed two orthonormal elliptical polarizations and demonstrate waveguides having modes with a polarization eccentricity of 0.25, which agrees very well with the theory. Although the achieved mode ellipticity is not large enough to meet the requirement – predominant circularly polarized modes – for practical applications, this is, to the best of our knowledge, the first experimental demonstration of the mode ellipticities for the transverse electric field of the chiral-core optical waveguides. Characterizations and feasibilities of several other chiral materials are also discussed. Unfortunately, none of these materials exhibit both appreciable material chirality and negligible linear birefringence at the same time. The design and synthesis of isotropic materials with high chirality is in progress.

Chapter 3 will examine organic magneto-optic materials, which can be viable alternatives to the chiral materials. In addition to polarization rotators, they also can potentially be used for integrated-optic isolators or circulators. The Faraday effect in magneto-optic materials in a magnetic field is another class of optical activity, and it is characterized by *Verdet* constant. Measuring the Verdet constants of thin ($10 - 100 \mu\text{m}$) organic samples under a moderate magnetic field ($< 100 \text{ Gauss}$) can be very challenging. For this reason, we discuss *balanced homodyne detection* that provides a highly sensitive technique to measure an angle of polarization rotation as small as $0.5 \times 10^{-6} \text{ rad}$. We demonstrate the Verdet constants of 10.4 and $4.2 \text{ rad/T} \cdot \text{m}$ at 1300 nm and 1550 nm , respectively, from an organic sample provided by Georgia Tech, which is comparable to that of terbium gallium garnet. This unique observation can lead to integrated-optic isolators or circulators from a simple fabrication methodology including spin-casting and photolithography.

Chapter 4 will present low-loss waveguides and polymer microring resonators fabricated from perfluorocyclobutyl (PFCB) copolymer. Among the many materials for passive waveguide devices, fluorinated polymers are particularly attractive because they have very low absorption loss at telecommunication wavelengths. Low-loss waveguides are one of the most important building blocks in integrated-optic communication systems because most passive and active devices consist of simple straight and curved waveguide segments. For example, microring resonator based devices have very simple configurations of straight waveguides and circular rings, and the loss present in the ring is the most important parameter deter-

mining the device performance. For these reasons, this chapter is devoted to the design, fabrication, and characterization of those devices using PFBCB. We demonstrate straight waveguides with propagation losses of 0.3 dB/cm and 1.1 dB/cm for a buried channel and pedestal structures, respectively, and a microring resonator with a maximum extinction ratio of 4.87 dB, quality factor $Q = 8554$, and finesse $\mathcal{F} = 55$. In addition, we demonstrate that all-optical switching with the PFBCB microring resonator is possible when it is optically pumped with a femtosecond laser pulse of a sufficient energy. From a microring-loaded Mach-Zehnder interferometer, we demonstrate a modulation response width of 30 ps and a maximum modulation depth of 3.8 dB from a optical pump with a pulse duration of 100 fs and pulse energy of 500 pJ when the signal wavelength is initially tuned close to one of the ring resonances.

Finally, chapter 5 will investigate a highly efficient organic bulk heterojunction photodetector fabricated from a blend of conjugated polymer (P3HT) and small molecule (fullerene C₆₀). Although the organic thin film photodetector shares fundamental photophysics with the organic photovoltaic cell in terms of the photocurrent generation process, the detector needs a slightly different approach from that used in a photovoltaic cell. We address the effect of multilayer thin film interference on the external quantum efficiency. From the numerical modelling to calculate the optical field distribution and absorption in the layers, based on the characterization of optical properties of individual layers comprising the detector, we propose a bulk heterojunction photodetector without the PEDOT:PSS and LiF

layers that are commonly used in photovoltaic cells to achieve high short-circuit current. Through the experimental I - V characterization, we demonstrate that it exhibits an external quantum efficiency $\eta_{\text{EQE}} = 87 \pm 2\%$ under an applied bias voltage $V = -10\text{ V}$, leading to an internal quantum efficiency $\eta_{\text{IQE}} \sim 97\%$. These results show that the charge collection efficiency across the intervening energy barriers can indeed reach near 100% under a strong electric field. The achieved external quantum efficiency is one of the highest values published so far.

CHAPTER 2

OPTICAL CHIRAL WAVEGUIDE

2.1 Organic chiral material and optical activity

When molecules do not possess a plane of symmetry so that they are not superimposable on their mirror images through rotation and translation, they are referred to as *optical isomers* or *enantiomers* and are said to be *chiral*. The word “chiral” is derived from Greek meaning ‘hand’: our hands are mirror images and they cannot be superimposed on each other no matter how hard we try.

Most of the physical and chemical properties of enantiomers are identical – melting point, boiling point, density, solubility, etc. – but they can interact differently in biological systems. For this reason, chiral molecules are of particular interest in the pharmaceutical industry; of their two forms, one is clinically very effective but the other is ineffective or even dangerous at times. One example is *thalidomide* that was used for pregnant women in aiding morning sickness. It was discovered, however, that one handedness of the molecule, (*S*)-thalidomide, relieved the woman’s nausea, but the other handedness, *R*-enantiomer, caused horrible birth defects. Another example of a chiral drug is *ibuprofen*, commonly found in over-the-counter pain relievers. (*R*)-ibuprofen in racemic mixture is not only 100

times less effective, but also substantially slows the rate at which *S*-enantiomer takes effect in the body [5, 6].

When these chiral materials interact with electromagnetic waves, the plane of polarization is rotated and they are said to be *optically active*. This optical activity has been the subject of investigation for a few decades, especially in the microwave and optics areas. Although quantum mechanics is required to give us a complete understanding of the origin of the optical activity, it can simply be explained as circular birefringence [7].

The modes in a chiral bulk material are right-handed circular polarization (RHC) and left-handed circular polarization (LHC). When a linearly polarized light enters into the chiral medium, it is decomposed into two orthogonal co-propagating circular polarizations, RHC and LHC, travelling at different speeds due to the circular birefringence. After propagating through the chiral material and recombining, the output is linearly polarized as well, but is rotated by a certain angle with respect to the plane of polarization of the incident wave. In general, how much a certain chiral material rotates a plane of polarization is described by *specific rotatory power* $[\alpha]_D^{25}$ in units of $[\frac{\text{deg}\cdot\text{cm}^2}{\text{dm}\cdot\text{g}}]$, where 25 and D represents a temperature of 25 °C and a wavelength of the sodium D line at 589 nm, respectively. The traditional sign convention for the optical activity in a chiral material is the following: with light propagation through a sample towards an observer, $\alpha > 0$ represents clockwise rotation and $\alpha < 0$ represents counter-clockwise rotation when viewed from the direction toward which the light is travelling (i.e. looking at the

light source). Sometimes, it is referred to as (+), right-handed or *dextro*-rotatory chiral when $\alpha > 0$, and (-), left-handed or *levo*-rotatory when $\alpha < 0$ ¹. It should be noted that this sign convention is exclusively used by chemists and the opposite convention is adopted in many physics or engineering text books.

Organic chiral materials that form amorphous isotropic thin solid films have potential use in optical waveguides for photonic applications. The recent theory [8] on chiral-core planar waveguide suggests that an optical waveguide device may be possible for novel applications, provided that low loss amorphous films of sufficient chirality can be fabricated.

Useful applications include passive TE/TM mode converters for rotating the output polarization of semiconductor lasers to optimize the polarization for downstream active waveguide devices in integrated optics, and active polarization control by combining an optically active waveguide segment with an electrooptic phase shifter. There is a distinct advantage to achieving polarization rotation by optical activity instead of linear birefringence. For a birefringent linear polarization rotator, the input polarization must be at a 45° angle with respect to the optic axis – a condition that is difficult to achieve in integrated optics. An optically active bulk material that is isotropic, on the other hand, will rotate a linearly polarized input of any orientation to a linearly polarized output.

To make use of this advantage in integrated optics, the eigenmodes of the chiral

¹*dextro* and *levo* are from Latin meaning right and left, quite often they are used as *d* and *l* in short, respectively.

waveguide must be circularly polarized. The challenge for this application is to synthesize polymer or macromolecular structures with a high degree of chirality, ultimately extending into the near infrared for telecommunication applications, that also form amorphous isotropic thin films with negligible linear birefringence. Large specific rotations on the order of 15,000 $\frac{\text{deg}\cdot\text{cm}^2}{\text{dm}\cdot\text{g}}$ have been realized, for example, with helicenes [9]. However, these molecules tend to aggregate in the formation of thin films, a feature which can cause increased optical loss.

Although there has been relatively recent interest in the nonlinear optical properties of chiral materials, novel chiral photonic waveguides from linear chiral optical effects are discussed here based on the development of chiral-core asymmetric slab waveguides from amorphous organic binaphthyl films.

2.2 Unique polarization properties of chiral-core planar waveguides

Chirality in a dielectric planar waveguide introduces considerable mathematical complexity, resulting in mode properties that can be significantly different from those of the achiral case. This section reviews the theoretical analysis of the chiral core planar (a)symmetric waveguides to provide a relatively comprehensive summary for later discussions. Although there are a number of theoretical papers published, this section will mainly focus on reference [8] because all the analysis performed in this chapter adopts the approach described there. It has the distinctive advantage that the modal eigenvalue equations contain, in relatively simple form, a pair of parameters determining the eccentricity of the polarization ellipse

for the transverse electric field.

2.2.1 Fields in bulk chiral media

When there are no “free” charges and currents inside the media ($\mathbf{J} = \rho = 0$), the electric and magnetic fields satisfy the Maxwell’s equations [10],

$$\nabla \times \mathbf{E} = -\frac{\partial \mathbf{B}}{\partial t}, \quad (2.1)$$

$$\nabla \times \mathbf{H} = \frac{\partial \mathbf{D}}{\partial t}, \quad (2.2)$$

$$\nabla \cdot \mathbf{D} = 0, \quad (2.3)$$

$$\nabla \cdot \mathbf{B} = 0. \quad (2.4)$$

The boundary conditions that must be satisfied by the electric and magnetic fields at the interface between two different dielectric materials, designated 1 and 2, can be expressed as

$$(\mathbf{E}_1 - \mathbf{E}_2) \times \hat{\mathbf{n}} = 0, \quad (2.5)$$

$$(\mathbf{H}_1 - \mathbf{H}_2) \times \hat{\mathbf{n}} = 0, \quad (2.6)$$

$$(\mathbf{D}_1 - \mathbf{D}_2) \cdot \hat{\mathbf{n}} = 0, \quad (2.7)$$

$$(\mathbf{H}_1 - \mathbf{H}_2) \cdot \hat{\mathbf{n}} = 0. \quad (2.8)$$

If we assume that all the field components have a time-dependence of $e^{j\omega t}$,

$$\mathbf{E}(\mathbf{r}, t) = \text{Re}\{\bar{\mathbf{E}}(\mathbf{r}) \exp(j\omega t)\}, \quad (2.9)$$

$$\mathbf{H}(\mathbf{r}, t) = \text{Re}\{\bar{\mathbf{H}}(\mathbf{r}) \exp(j\omega t)\}, \quad (2.10)$$

we can rewrite the equations involving time derivatives, Eqs. 2.1 and 2.2, in terms of complex field quantities.

$$\nabla \times \bar{\mathbf{E}} = -j\omega \bar{\mathbf{B}}, \quad (2.11)$$

$$\nabla \times \bar{\mathbf{H}} = j\omega \bar{\mathbf{D}}. \quad (2.12)$$

Next, we adopt the Drude-Born-Federov² constitutive relation in order to introduce material chirality from isotropic chiral media into Maxwell's equations [13].

$$\bar{\mathbf{D}} = \epsilon(\bar{\mathbf{E}} + \gamma \nabla \times \bar{\mathbf{E}}), \quad (2.13)$$

$$\bar{\mathbf{B}} = \mu(\bar{\mathbf{H}} + \gamma \nabla \times \bar{\mathbf{H}}), \quad (2.14)$$

where ϵ and μ are the permittivity and permeability, and γ is the chirality having the units of length. For reference, a chirality parameter γ of 1 pm corresponds to a bulk rotatory power ρ of 15 deg/mm at a wavelength of 633 nm with an average refractive index of 1.62. From Eq. 2.11–2.14, we can obtain

$$(1 - \omega^2 \mu \epsilon \gamma^2) \nabla \times \bar{\mathbf{E}} - \omega^2 \mu \epsilon \gamma \bar{\mathbf{E}} + j\omega \mu \bar{\mathbf{H}} = 0, \quad (2.15)$$

$$(1 - \omega^2 \mu \epsilon \gamma^2) \nabla \times \bar{\mathbf{H}} - \omega^2 \mu \epsilon \gamma \bar{\mathbf{H}} - j\omega \epsilon \bar{\mathbf{E}} = 0. \quad (2.16)$$

These coupled equations can be reduced to Helmholtz wave equations with Bohren's decomposition of $\bar{\mathbf{E}}$ and $\bar{\mathbf{H}}$,

$$\bar{\mathbf{F}}^\pm \equiv \bar{\mathbf{E}} \pm j\sqrt{\frac{\mu}{\epsilon}} \bar{\mathbf{H}}, \quad (2.17)$$

²Another choice for a constitutive relation describing isotropic chiral media may be the symmetrized Condon set, $\bar{\mathbf{D}} = \epsilon \bar{\mathbf{E}} - jg\omega \bar{\mathbf{H}}$ and $\bar{\mathbf{H}} = \mu \bar{\mathbf{H}} + jg\omega \bar{\mathbf{E}}$. However, two constitutive equations, Drude-Born-Federov and symmetrized Condon, are equivalent to first order in g and γ [11, 12].

or

$$\bar{\mathbf{E}} = \frac{1}{2}(\bar{\mathbf{F}}^+ + \bar{\mathbf{F}}^-), \quad (2.18)$$

$$\bar{\mathbf{H}} = \frac{1}{2j}\sqrt{\frac{\epsilon}{\mu}}(\bar{\mathbf{F}}^+ - \bar{\mathbf{F}}^-). \quad (2.19)$$

By using Eqs. 2.15 and 2.16, and from Eqs. 2.18 and 2.19, we can easily verify that

$$\nabla \times \bar{\mathbf{F}}^\pm = \mp k_0 n_\pm \bar{\mathbf{F}}^\pm, \quad (2.20)$$

$$n_\pm \equiv \frac{n_g}{1 \pm \delta}, \quad (2.21)$$

$$\delta \equiv \omega \sqrt{\mu \epsilon} \gamma = k_0 n_g \gamma, \quad (2.22)$$

where n_g is the index of refraction, $\sqrt{\epsilon/\epsilon_0}$, since we assume $\mu = \mu_0$, and k_0 is the free-space wave vector, $2\pi/\lambda_0$. Finally, we can obtain the Helmholtz equations for $\bar{\mathbf{F}}^\pm$ by computing the curl of Eq. 2.20.

$$\nabla^2 \bar{\mathbf{F}}^\pm + k_0^2 n_\pm^2 \bar{\mathbf{F}}^\pm = 0. \quad (2.23)$$

Note that, in bulk media, solutions of Eq. 2.20 have the form,

$$\bar{\mathbf{F}}^\pm = (\hat{\mathbf{x}} \pm j\hat{\mathbf{y}}) F_o \exp(-jk_0 n_\pm z), \quad (2.24)$$

representing plane waves with right-handed circular (RHC) and left-handed circular (LHC) polarization. In terms of handedness describing how the end point of the electric field vector traces a circle or ellipse on a plane perpendicular to the beam, there exist two opposing conventions. To avoid any confusion, we shall use the convention throughout this chapter as used in most optics books: for the RHC (LHC), the electric field vector rotates clockwise (counter-clockwise) in time at a

fixed position in space to an observer looking at the source of the light. In fact, this convention seems more natural since the rotation of the electric field vector and the direction of propagation form a right-handed screw (left-handed screw) in space at a fixed time for the RHC (LHC) in our definition here. It is important to note, however, that if $e^{-j\omega t}$ was used for a time dependence of field components instead of $e^{+j\omega t}$, the handedness would be reversed: $\bar{\mathbf{F}}^+$ for LHC and $\bar{\mathbf{F}}^-$ for RHC.

Optical rotatory power due to the circular birefringence is given by

$$\rho = \frac{\pi}{\lambda_o} (n_- - n_+) \quad (2.25)$$

$$\simeq k_0 n_g \delta, \quad \text{for } \delta \ll 1, \quad (2.26)$$

2.2.2 Eigenmodes in asymmetric chiral planar waveguides

As we discussed in section 2.2.1, the eigenmodes in bulk chiral media are RHC and LHC polarizations. In a waveguide structure, however, the eigenmodes are two orthonormal elliptically polarized modes in general – right-handed elliptical (RHE) and left-handed elliptical (LHE) polarizations – due to influence of the boundary conditions. This section describes in detail the polarization properties of eigenmodes in an asymmetric chiral planar waveguide, using eigenvalue equations in terms of a pair of parameters g and h corresponding to the ellipticity for the transverse electric field [8]. Hence it allows a detailed insight into the polarization properties.

Consider the planar waveguide structure shown in Fig. 2.1. The upper and lower cladding layers are not chiral having indices of refraction n_o and n_s , respec-

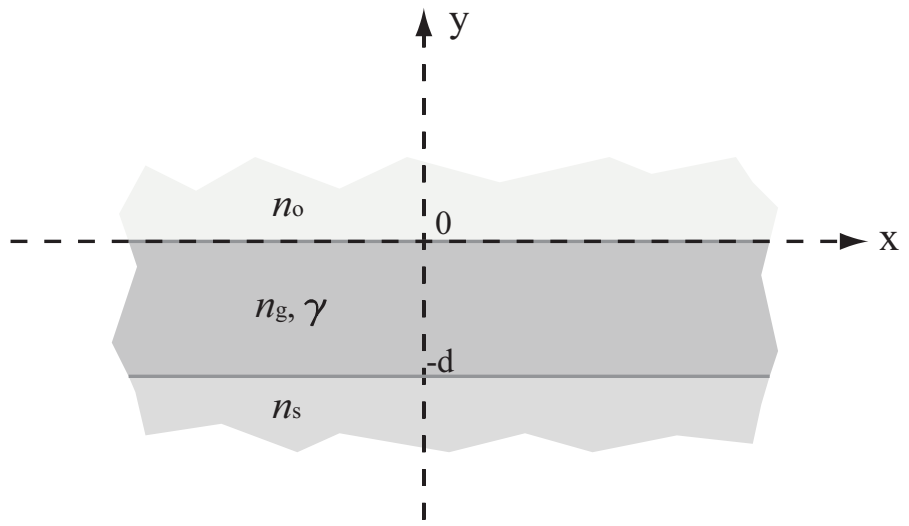


Figure 2.1: The structure of an asymmetric planar waveguide with an isotropic chiral core. The upper and lower cladding layers are not chiral having indices of refraction n_o and n_g , respectively, and the core layer has an index n_g , chirality γ , and thickness d . The coordinate axes have been oriented such that the waveguide points in the z -direction and is assumed to be infinite in the $\pm x$ -direction.

tively, and the core layer has an index n_g , chirality γ , and thickness d . The coordinate axes have been oriented such that the waveguide points in the z -direction and is assumed to be infinite in the $\pm x$ -direction. If we assume a solution for the Helmholtz wave equation of the form,

$$\bar{\mathbf{F}}^\pm(y, z) = \Psi^\pm(y) \exp(-jk_0 n_{\text{eff}} z), \quad (2.27)$$

where n_{eff} is the effective index of a mode propagating along the $+z$ -direction, then the cartesian x-component of Ψ^\pm satisfies the Helmholtz equation (putting $\frac{\partial}{\partial x} = 0$):

$$\frac{d\Psi_x^\pm(y)}{dy^2} + k_0^2(n_q^2 - n_{\text{eff}}^2)\Psi_x^\pm = 0, \quad (2.28)$$

where the subscript q in n_q denotes the waveguide layer, ‘ \pm ’ in the core, ‘ o ’ in the upper cladding, and ‘ s ’ in the lower cladding layer. As in the achiral slab waveguide, the solution to the above equation can be written as

$$y = \begin{cases} A^\pm \exp(-vy) & y \geq 0 \\ B^\pm \cos(u^\pm y + \phi^\pm) & 0 < y < -d \\ C^\pm \exp[w(y + d)] & y \leq -d \end{cases}, \quad (2.29)$$

where

$$\begin{aligned} u^\pm &\equiv k_0 \sqrt{n_\pm^2 - n_{\text{eff}}^2}, \\ v &\equiv k_0 \sqrt{n_{\text{eff}}^2 - n_o^2}, \\ w &\equiv k_0 \sqrt{n_{\text{eff}}^2 - n_s^2}. \end{aligned} \quad (2.30)$$

The y and z-component of Ψ^\pm can be obtained from Eq. 2.20 and $\Psi_x^\pm(y)$,

$$\Psi_y^\pm(y) = \pm j \frac{n_{\text{eff}}}{n_q} \Psi_x^\pm(y), \quad (2.31)$$

$$\Psi_z^\pm(y) = \pm \frac{1}{k_0 n_q} \frac{d\Psi_x^\pm(y)}{dy}. \quad (2.32)$$

From Eqs. 2.5 and 2.6 describing the boundary conditions that require continuity of the tangential components of $\bar{\mathbf{E}}$ and $\bar{\mathbf{H}}$ across the interface at $y = 0$ and $y = -d$, and using Eqs. 2.18–2.27, we can obtain a set of eight equations. Eliminating A^\pm from the four equations at $y = 0$, and C^\pm from the remaining four equations at $y = -d$ yields

$$B^+(\sigma_o^+ \sin \phi^+ - \cos \phi^+) + B^-(\sigma_o^- \sin \phi^- - \cos \phi^-) = 0, \quad (2.33)$$

$$B^+(r_o \sigma_o^+ \sin \phi^+ - \cos \phi^+) - B^-(r_o \sigma_o^- \sin \phi^- - \cos \phi^-) = 0, \quad (2.34)$$

$$\begin{aligned} & B^+[\sigma_s^+ \sin(u^+ d - \phi^+) - \cos(u^+ d - \phi^+)] \\ & + B^-[\sigma_s^- \sin(u^- d - \phi^-) - \cos(u^- d - \phi^-)] = 0, \end{aligned} \quad (2.35)$$

$$\begin{aligned} & B^+[r_s \sigma_s^+ \sin(u^+ d - \phi^+) - \cos(u^+ d - \phi^+)] \\ & - B^-[r_s \sigma_s^- \sin(u^- d - \phi^-) - \cos(u^- d - \phi^-)] = 0, \end{aligned} \quad (2.36)$$

where

$$\begin{aligned} \sigma_o^\pm & \equiv (1 \pm \delta) \frac{u^\pm}{v}, \\ \sigma_s^\pm & \equiv (1 \pm \delta) \frac{u^\pm}{w}, \\ r_p & \equiv \frac{n_p^2}{n_g^2}, \quad p = o \text{ or } s, \end{aligned} \quad (2.37)$$

By introducing two equations – which equivalently satisfy the conditions that the determinants of the coefficients B^+ and B^- in Eqs. 2.33 and 2.34, and Eqs. 2.35

and 2.36 are zeros – including new parameters g and h such that

$$\cot \phi^\pm = \sigma_o^\pm \left(\frac{r_o \pm g}{1 \pm g} \right), \quad (2.38)$$

$$\cot(u^\pm d - \phi^\pm) = \sigma_s^\pm \left(\frac{r_s \pm h}{1 \pm h} \right), \quad (2.39)$$

and solving for the determinant, the four equations (Eqs. 2.33–2.36) can give a single equation,

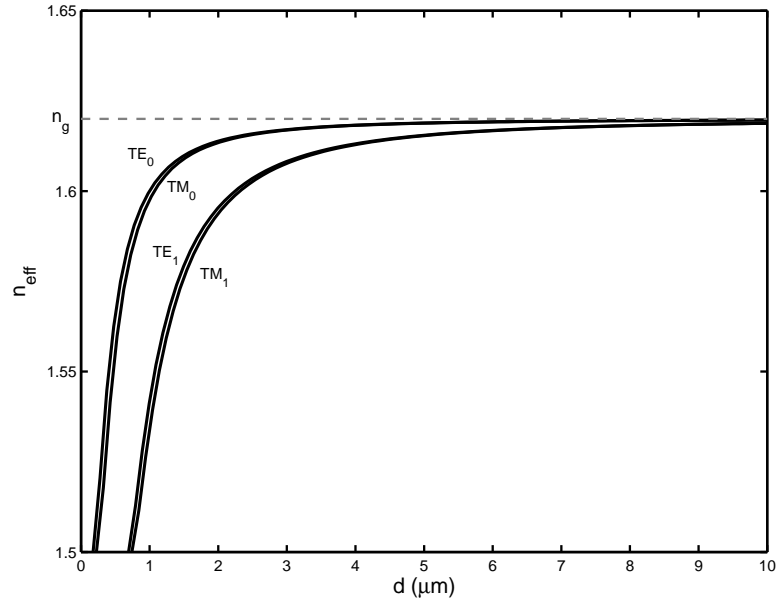
$$\frac{1+h}{1-h} = \frac{S_{r_o}^+ + S_{r_o}^+ g}{S_{r_o}^- + S_{r_o}^- g}. \quad (2.40)$$

Note that Eqs. 2.38, 2.39 and 2.40 represent five equations with five unknowns ϕ^\pm , g , h and n_{eff} , and equivalently state all the constraints imposed by the boundary conditions. We can eliminate ϕ^\pm in Eqs. 2.38 and 2.39, and solve Eq. 2.40 for h in order to obtain eigenvalue equations along with the mode eccentricity parameters g and h ,

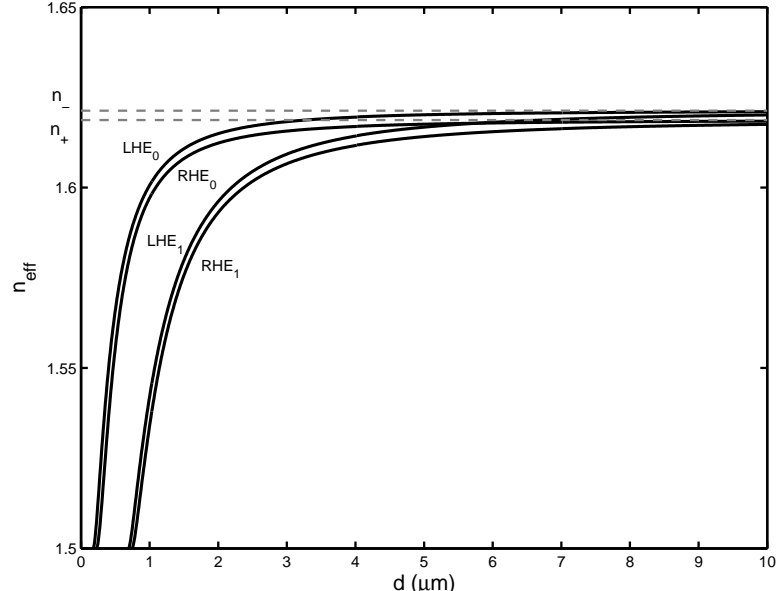
$$u^\pm d = \cot^{-1} \left(\sigma_o^\pm \frac{r_o \pm g}{1 \pm g} \right) + \cot^{-1} \left(\sigma_s^\pm \frac{r_s \pm h}{1 \pm h} \right) + m^\pm \pi, \quad (2.41)$$

$$h(g, n_{\text{eff}}) = \frac{(S_{r_o}^+ - S_{r_o}^-) + (S_o^+ - S_o^-)g}{(S_{r_o}^+ + S_{r_o}^-) + (S_o^+ - S_o^-)g}. \quad (2.42)$$

It is worth noting that Eq. 2.41 has an inverse-trigonometric form, similar to the achiral case that is familiar to us [14]. The two equations in Eq. 2.41 can be simultaneously solved for g and n_{eff} with Eq. 2.42. For an example, Fig. 2.2 shows the calculation for the mode effective index n_{eff} as a function of waveguide core thickness d at a wavelength $\lambda = 633$ nm for the fundamental and the first higher modes in an achiral ($\gamma = 0$) and a chiral ($\gamma = 50$ pm) asymmetric planar waveguide. The refractive index of the core layer is $n_g = 1.62$, and the upper and lower cladding



(a) Achiral ($\gamma = 0$)



(b) Chiral ($\gamma = 50 \text{ pm}$)

Figure 2.2: Calculation of the mode effective index n_{eff} vs. waveguide thickness d , for the fundamental and the first higher modes in (a) an achiral ($\gamma = 0$) and (b) a chiral ($\gamma = 50 \text{ pm}$) asymmetric planar waveguide. The refractive indices $n_g = 1.62$, $n_o = 1.00$, and $n_s = 1.50$ are used for this calculation.

indices are $n_o = 1.00$ and $n_s = 1.50$, respectively. The n_{eff} 's for TE and TM in the achiral case are asymptotic to the core index n_g with increasing thickness far from the cut-off. On the other hand, the n_{eff} 's for RHE and LHE in the chiral case are asymptotic to the core indices n_+ and n_- , respectively with increasing thickness [8, 15, 16].

Once g and n_{eff} are obtained, ϕ^\pm can be found from Eq. 2.38, and other remaining constants for field amplitudes in Eq. 2.29 can be found as,

$$B^+ = B^- \frac{g + r_o \cos \phi^-}{g - r_o \cos \phi^+}, \quad (2.43)$$

$$A^\pm = B^- \cos \phi^- \frac{g \pm \sqrt{r_o}}{g - r_o}, \quad (2.44)$$

$$C^\pm = B^- \cos(u^- d - \phi^-) \frac{h \pm \sqrt{r_s}}{h - r_s}. \quad (2.45)$$

From Eqs. 2.18 and 2.27, the transverse electric field is given by

$$\bar{\mathbf{E}}_T = \frac{1}{2} \left\{ [\Psi_y^+(y) - \Psi_y^-(y)] \hat{\mathbf{x}} + j n_{\text{eff}} \left[\frac{\Psi_y^+(y)}{n_q} - \frac{\Psi_y^-(y)}{n_q} \right] \hat{\mathbf{y}} \right\} \exp(-jk_0 n_{\text{eff}} z). \quad (2.46)$$

The polarization for the field given by the above equation is, in general, an elliptical polarization with major axes on either the x or y axis. The mode eccentricity – the ratio of the y -component to the x -component – in the upper cladding ($y \geq 0$) is given by

$$\left. \frac{E_y}{E_x} \right|_{y \geq 0} = j \frac{n_{\text{eff}}}{n_o} \frac{\sqrt{r_o}}{g} = j \frac{n_{\text{eff}}}{n_g} \frac{1}{g}, \quad (2.47)$$

and the mode eccentricity in the lower cladding ($y \leq 0$) is given by

$$\left. \frac{E_y}{E_x} \right|_{y \leq -d} = j \frac{n_{\text{eff}}}{n_s} \frac{\sqrt{r_s}}{h} = j \frac{n_{\text{eff}}}{n_g} \frac{1}{h}. \quad (2.48)$$

The polarization ellipse in the core is more complicated than in the cladding and varies with position in y , but considering the equation,

$$\frac{B^+}{B^-} = \frac{g+1}{g-1} \sqrt{\frac{\frac{1}{\sigma_o^{+2}} + \left(\frac{g+r_o}{g+1}\right)^2}{\frac{1}{\sigma_o^{-2}} + \left(\frac{g-r_o}{g-1}\right)^2}}, \quad (2.49)$$

gives an idea of the mode eccentricity. In limiting cases,

when $\gamma \rightarrow 0$,

$$B^- = B^+, \text{ as } g \rightarrow \pm\infty \longrightarrow \text{TE}$$

$$B^- = -B^+, \text{ as } g \rightarrow 0 \longrightarrow \text{TM},$$

when $\gamma \neq 0$,

$$B^+/B^- \rightarrow 1, \text{ as } g \rightarrow \pm\infty \longrightarrow \text{predominant TE}$$

$$B^+/B^- \rightarrow -1, \text{ as } g \rightarrow 0 \longrightarrow \text{predominant TM}$$

$$B^+/B^- \gg 1, \text{ as } g \rightarrow 1 \longrightarrow \text{predominant RHC}$$

$$B^+/B^- \ll 1, \text{ as } g \rightarrow -1 \longrightarrow \text{predominant LHC}.$$

Figure 2.3 illustrates the mode ellipticity parameter g as a function of chirality γ for the fundamental elliptical modes, RHE₀ and LHE₀, in the asymmetric planar waveguide with a $3 \mu\text{m}$ thick chiral-core, an average core refractive index $n_g = 1.62$, and upper and lower cladding indices of $n_o = 1.00$ and $n_s = 1.50$, respectively. When $\gamma > 0$, the RHE(LHE) modes evolve from TM(TE) at $\gamma = 0$ and become predominantly RHC(LHC) modes with increasing chirality.

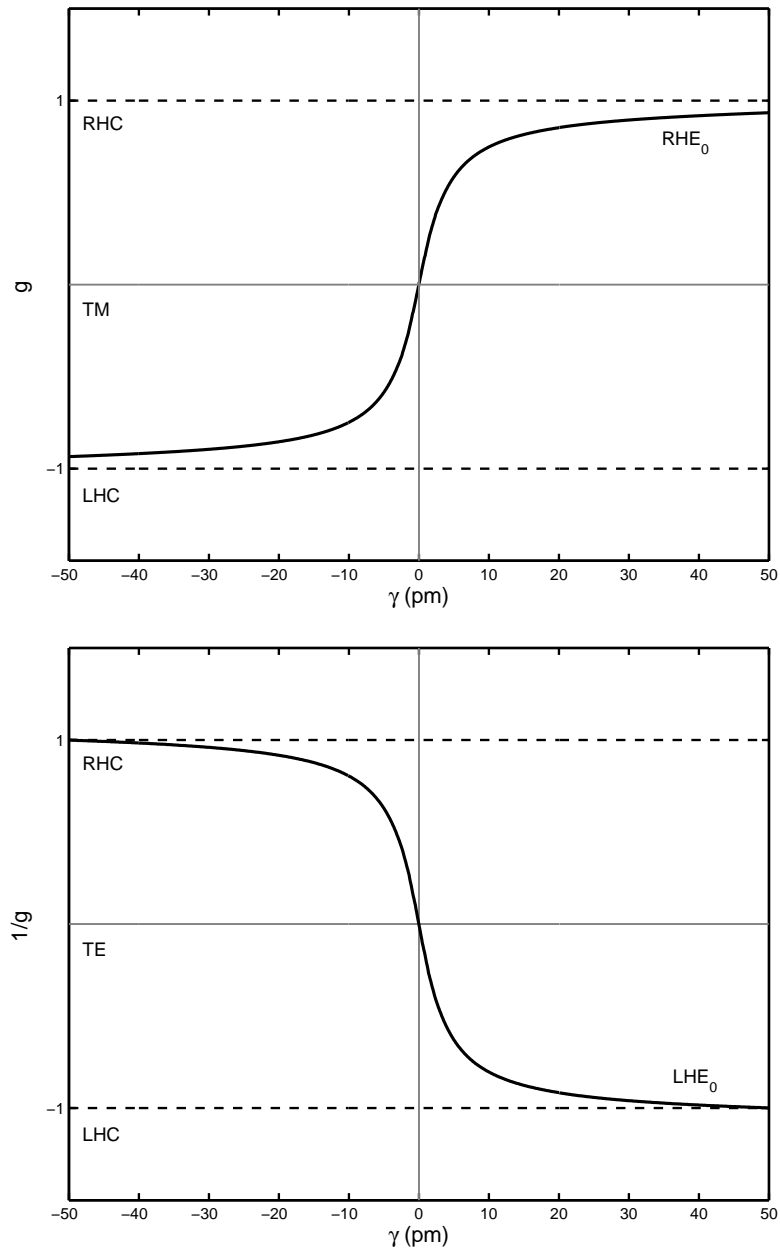


Figure 2.3: Calculation of the mode eccentricity parameter g vs. chirality γ for the lowest order elliptical modes, RHE_0 and LHE_0 , in an asymmetric planar waveguide with a $3\ \mu\text{m}$ thick chiral-core, and refractive indices $n_g = 1.62$, $n_o = 1.00$ and $n_s = 1.50$. When $\gamma > 0$, the $RHE(LHE)$ modes evolve from TM(TE) at $\gamma = 0$ and become predominantly RHC(LHC) modes with increasing chirality.

It should be noted that a small refractive index difference between the chiral-core and the cladding can effectively enhance the chirality effect. In other words, for a weakly guided waveguide structure, the mode ellipticity becomes close to unity – more nearly circular – for a given material chirality γ .

One way to look at this quantitatively is by considering the asymptotic limit of $|\sigma_s^\pm|$ in Eq. 2.37,

$$|\sigma_s^\pm| = \left| (1 \pm \delta) \frac{\sqrt{n_\pm^2 - n_{\text{eff}}^2}}{\sqrt{n_{\text{eff}}^2 - n_s^2}} \right| \quad (2.50)$$

$$\approx \sqrt{\frac{2\delta}{1 - r_s}}, \quad \text{for } n_{\text{eff}} \rightarrow n_g \text{ and } \delta \ll 1, \quad (2.51)$$

which is zero in the achiral case ($\delta = 0$), and increases either with increasing δ (proportional to the material chirality γ) or with increasing r_s , related to the index contrast Δn as

$$\Delta n = \frac{n_g - n_s}{n_g} = 1 - \frac{1}{\sqrt{r_s}}. \quad (2.52)$$

This can be explained qualitatively from the following: the mode in achiral waveguides are TE and TM in general. However, the critical angle for total internal reflection depends on the index difference between the core and cladding, therefore, in the weakly confined waveguides, only light at a grazing incidence angle that is bigger than the critical angle can be supported through the waveguide. This confined mode in the achiral case can be considered as approximately TEM in nature. Similarly, the RHE and LHE modes in chiral waveguides approximate as RHC and LHC in bulk for the weakly confined waveguides.

It should be noted that the mode ellipticity changes dramatically in the vicinity

of mode crossover points – where the curve of n_{eff} for the RHE modes successively cross over higher LHE modes, for example, n_{eff} for the RHE₀ with LHE₁ as in Fig. 2.2(b). In fact, in addition to those eccentricity parameters g and h , this is one of the most unique advantages using the theoretical developments in reference [8]. However, this does not concern us since we are primarily interested in a single mode waveguide that supports only the fundamental modes RHE₀ and LHE₀.

2.3 Chiral waveguides from amorphous binaphthyl films

Planar waveguides fabricated from chiral single molecules, identified as ML-224 and ML-226, synthesized by Prof. Green’s group at N. Y. Polytechnic University have been investigated for detailed experimental polarization analysis. Fig. 2.4 shows the chemical structures of both ML-224 and ML-226, which consist of binaphthyls attached to cis-1,3,5-cyclohexanetricarboxylic ester. These binaphthyl based chiral non-racemic compounds adopt a scheme designed to produce materials that form glassy isotropic thin solid films with negligible linear birefringence [17]. The bridged binaphthyls are based on work in [18], in which the thermal and photo-racemization of these materials were used to explore fundamental characteristics of the glassy state. The detailed synthetic work leading to ML-224 and ML-226 can be found in [19]. The glass transition temperature T_g measured with a differential scanning calorimeter (DSC) is in the range of 65–70 °C and 45–50 °C, and the specific rotatory power in solution measured with a polarimeter is $[\alpha]_D^{25} = +428 \text{ deg}$ and $[\alpha]_D^{25} = -468 \text{ deg}$, for ML-224 and ML-226, respectively. Note that ML-

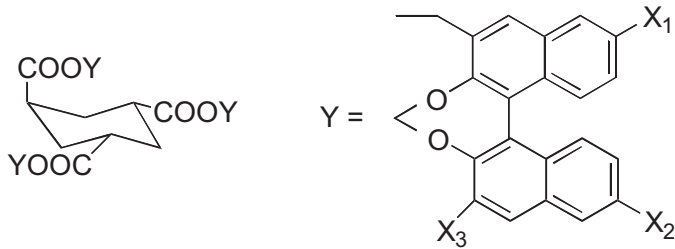


Figure 2.4: Chemical structure of the single molecule binaphthyls attached to cis-1,3,5-cyclohexanetricarboxylic ester. For ML-224, $X_1=H$, $X_2=H$ and $X_3=\text{CH}_2\text{O}-\text{heptyl}$, and for ML-226, $X_1=\text{heptyl}$, $X_2=\text{heptyl}$ and $X_3=H$.

224 is a right-handed (*d*-rotatory) chiral compound and ML-226 is a left-handed (*d*-rotatory) chiral compound as shown in Fig. 2.5 for optical rotatory dispersion (ORD) curves for both materials.

For thin solid films, the refractive index dispersion of these films was measured using a MetriconTM prism coupler, which determines the ordinary and extraordinary index of a film using two orthogonal linear polarizations at each of five discrete laser wavelengths. Figure 2.6 shows the measured refractive indices of the thin films fabricated from both ML-224 and ML-226, and curves fitted to the Sellmeier dispersion relation,

$$n^2 = A + B \frac{\lambda^2}{\lambda^2 - \lambda_o^2}, \quad (2.53)$$

where λ_o is the wavelength corresponding to the absorption peak in the material. As shown in the figure, both samples are isotropic within the experimental uncertainty (~ 0.0001). This isotropic property is extremely critical because even moderate amounts of linear birefringence can overpower the effects of optical ac-

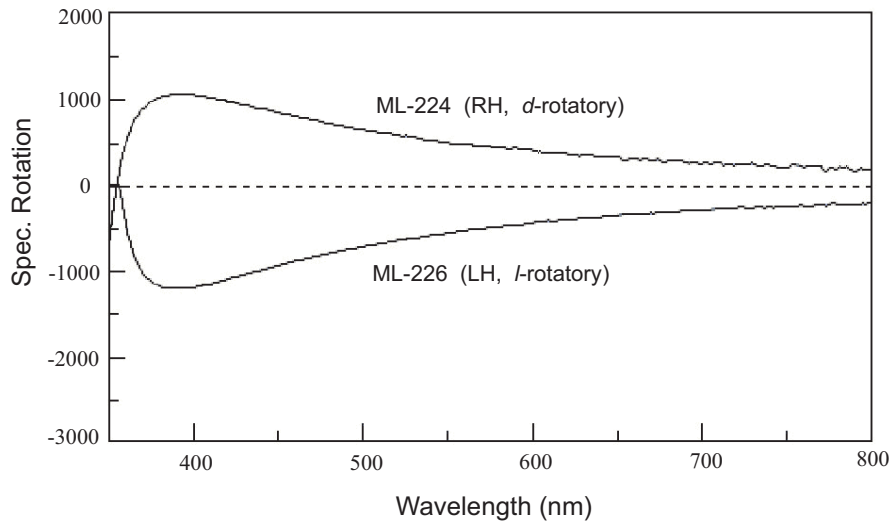


Figure 2.5: Optical rotatory dispersion (ORD) curves for ML-224 and ML-226. ML-224 has a right-handed chirality and ML-226 has a left-handed chirality.

tivity.

The optical activity of the solid films was measured using a 670 nm laser with the laser beam passing through the film at normal incidence. For these films, normal incidence corresponds to propagation along the optic axis, and therefore the circular birefringence can be measured independently of linear birefringence effects. The sample films, which are several microns thick on a fused quartz substrate, were placed between two Glan-Thompson polarizers in a polarizer-analyzer configuration, and the analyzer was rotated about the null position using a computer controlled precision rotation stage as depicted in Fig. 2.7. From a fit of the data to a sine-squared curve, the change in the null position of the film on a UV-grade fused quartz substrate was compared to the null for transmission through the

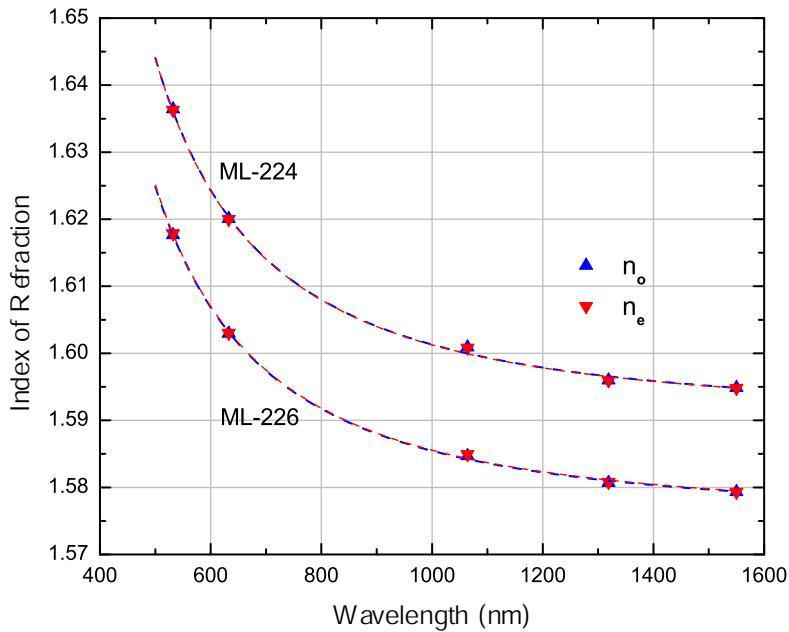


Figure 2.6: Index of refraction dispersion measured with a Metricron™ prism coupler for ML-224 and ML-226 in thin solid films. Both materials are isotropic within the experimental uncertainty (~ 0.0001).

substrate alone. Measured optical rotatory power at 670 nm is about 4–5 deg/mm for both ML-224 and ML-226, which is consistent with the specific rotatory power measured in solution.

Figure 2.8 depicts the structure of the asymmetric planar waveguide fabricated from ML-224 and ML-226 for a detailed study of the polarization properties of the eigenmodes. GaAs was used for a substrate simply due to its availability and ease of cleaving, and SiON was selected for the lower cladding layer because its refractive index can be easily tailored by controlling the ratio of the gas mixture in plasma-enhanced chemical vapor deposition (PECVD). Theoretically, the nitrogen-

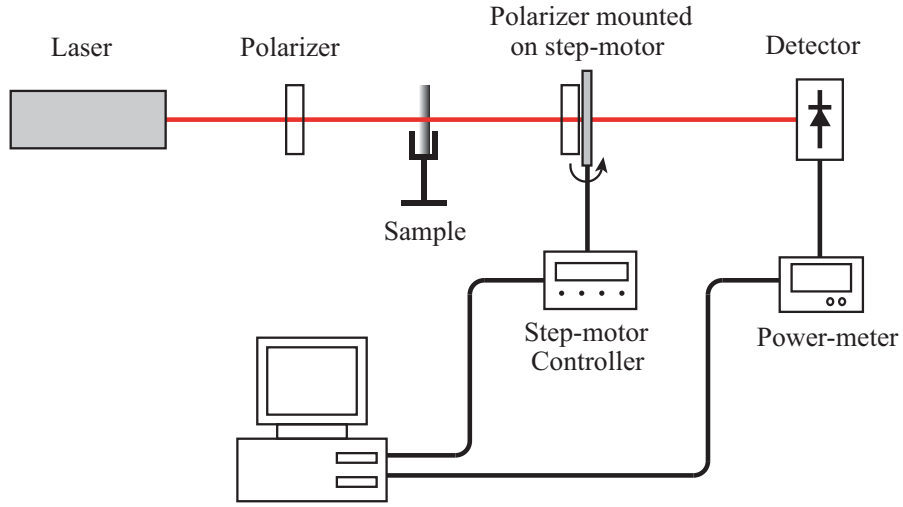


Figure 2.7: Experimental setup for measurement of optical rotatory power. The sample films were placed between two Glan-Thompson polarizers in a polarizer-analyzer configuration, and the analyzer was rotated about the null position using a computer controlled precision rotation stage.

to-oxygen ratio and hence the index of SiON can be varied over a significant range from ~ 1.46 , the index of silicon oxide, up to ~ 2.0 , the index of silicon nitride. For the SiON lower cladding, we used an Oxford Plasmalab PECVD with a chamber pressure of 300 mT and an RF power of 10 W at a substrate temperature of 300 °C. We fixed the flow rate of N₂O and SiH₄ to 12 sccm and 64 sccm, and varied the flow rate of NH₃ to reach the desired refractive index for the lower cladding, which results in a deposition rate of 95-105 Å/min.

After depositing the SiON layer on the GaAs substrate, to achieve approximately 3 μm thick films for single-mode waveguides, a solution of ML-224 and ML-226 dissolved in cyclohexanone ($\sim 27\%$ by weight) was spin-coated at 1000 RPM

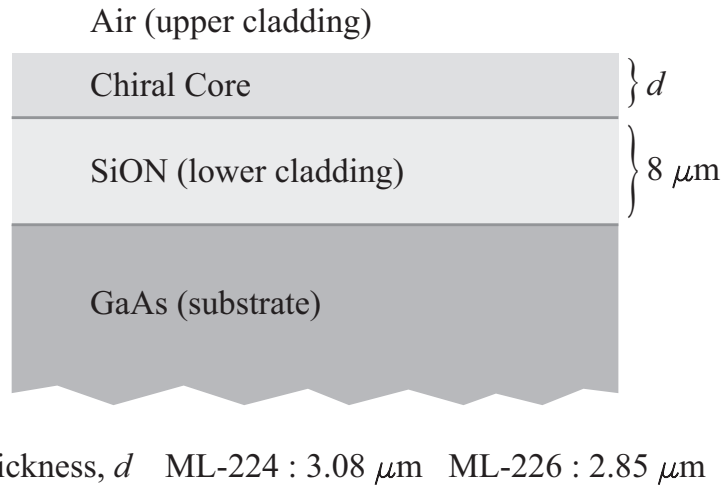


Figure 2.8: Structure of chiral slab waveguides on GaAs substrates coated with SiON.

Wavelength	ML-224		ML-226		SiON	
	n_o	n_e	n_o	n_e	for ML-224	for ML-226
633 nm	1.6201	1.6200	1.6030	1.6030	1.6135	1.5945

Table 2.1: Refractive indices of chiral-core layers from ML-224 and ML-226, and SiON lower cladding layers at 633 nm in the waveguide structure depicted in Fig. 2.8.

for 30 s on SiON, and then cured in a Fisher Scientific vacuum convection oven with N₂ environment. The temperature was elevated from room temperature up to T_g with a ramp rate of 3 °C/min, soaked for 30 min, and naturally cooled down to room temperature. For the final step, the waveguides were cleaved to form smooth end facets for input and output coupling.

Two critical design points should be noted at this point. First, the waveguide thickness was determined in order to satisfy single mode operation supporting the first two orthogonal modes RHE₀ and LHE₀ only. Figure 2.9 shows the calculation of mode effective index with increasing core thickness for each waveguide. The cut-off thickness of the first higher order elliptical mode is 3.15 μm for the waveguide from ML-224 and 2.8 μm for the waveguide from ML-226. Second, the refractive index of the SiON lower cladding layer was adjusted to be close to that of the chiral-core layer. As pointed out in section 2.2.2, a small index difference between the chiral-core and the cladding layer, n_g and n_s , respectively, is desirable because it can enhance the eccentricity of elliptical eigenmodes for a given amount of material chirality. The index contrast, $\Delta n = (n_g - n_s)/n_g$ at a wavelength of 633nm, was about 0.004-0.005 as shown in Tab. 2.1. Figure 2.10 shows the calculation of ellipticity of the fundamental modes, RHE₀ and LHE₀ as a function of chirality γ for three different lower cladding indices, 1.613, 1.550 and 1.500. When $\gamma = 1.0 \text{ pm}$, for example, the eccentricity parameter g almost doubles when n_s increases from 1.500 to 1.613.

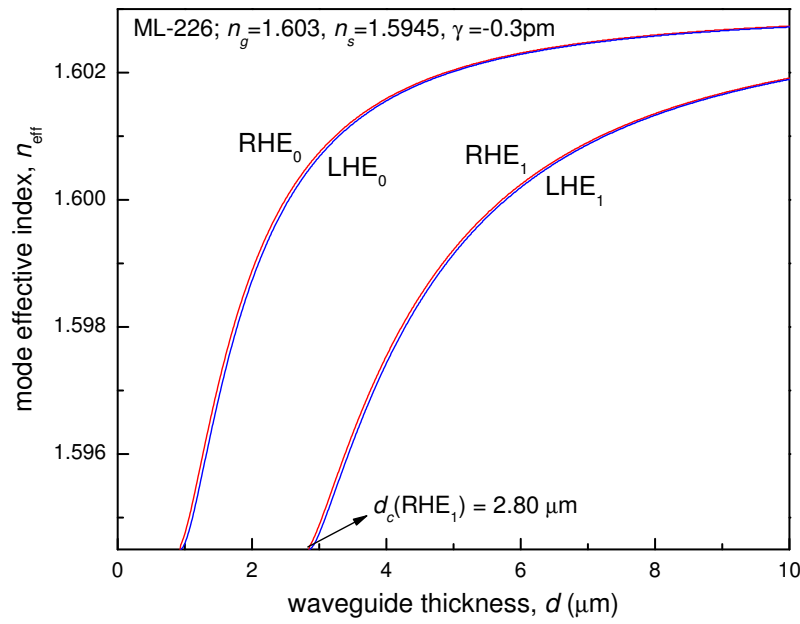
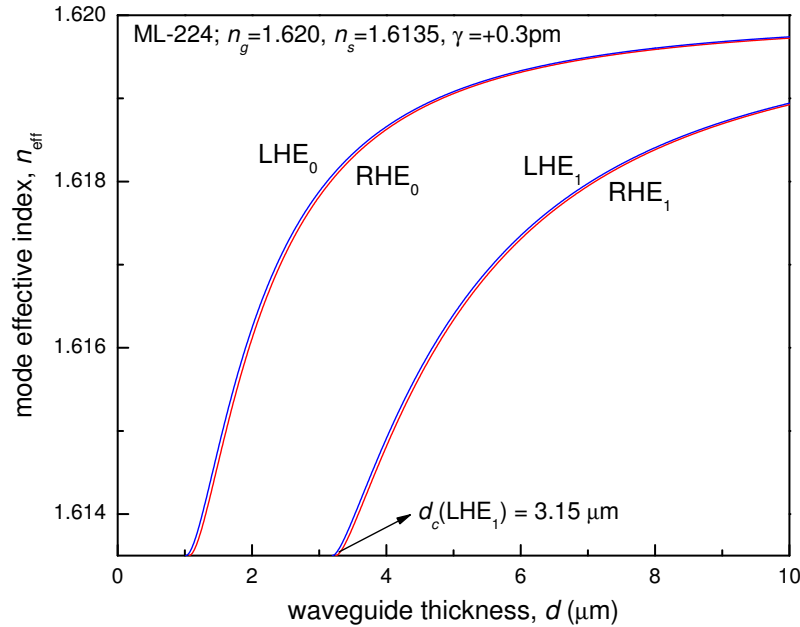


Figure 2.9: Calculation of n_{eff} with increasing waveguide core thickness. (a) The cut-off thickness of LHE₁ mode is about $3.15 \mu\text{m}$ for the waveguide from ML-224. (b) The cut-off thickness of RHE₁ mode is $2.8 \mu\text{m}$ for the waveguide from ML-226.

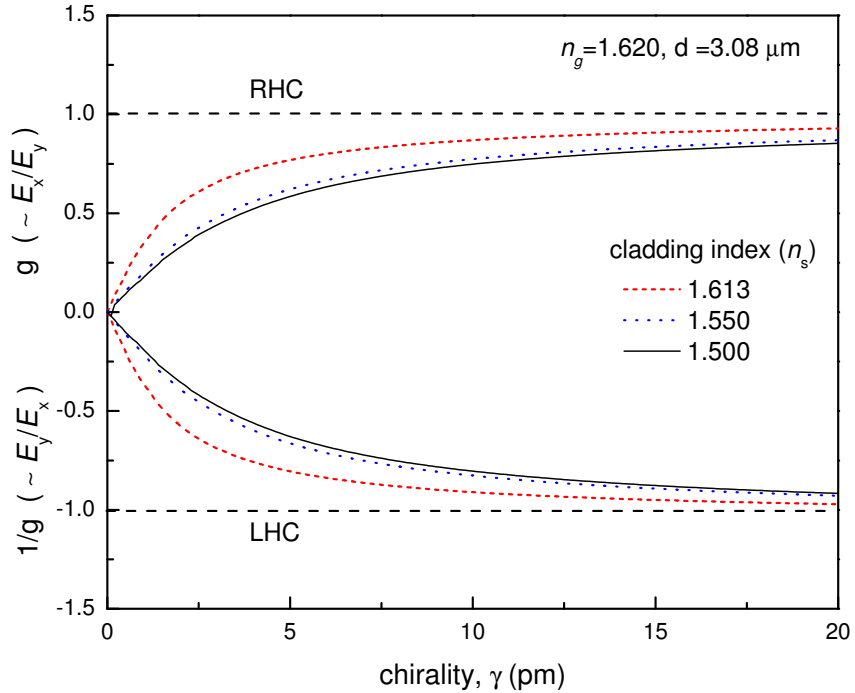


Figure 2.10: Calculation of mode ellipticity of RHE_0 and LHE_0 of asymmetric slab waveguide as a function of given material chirality γ for the core index $n_g = 1.620$ and three different lower cladding indices, $n_s = 1.613$, 1.550, and 1.500. When a $\gamma = 1.0$ pm, for example, the eccentricity parameter g almost doubles when n_s increases from 1.500 to 1.613.

2.4 Experimental polarization analysis

In previous sections we discussed the theoretical polarization properties of the eigenmodes and fabrication of asymmetric planar chiral-core waveguide from binaphthyl based chiral compounds including key design parameters. For experimental polarization analysis of these thin film waveguides, the state of polarization (SOP) represented by normalized Stokes parameters of the eigenmodes was characterized by determining the SOP at the output of the waveguide for two orthogonal input polarizations: horizontal and vertical polarizations. We refer to these orthogonal linearly polarized inputs as TE and TM with respect to the slab surface because, in an achiral slab waveguide, they would excite usual TE and TM modes. For chiral waveguides, a linearly polarized input will excite both eigenmodes, RHE and LHE, and the TE input excites a different relative fraction of these elliptical eigenmodes than the TM input. As the light propagates down the waveguide, the RHE and LHE modes travel at different speeds resulting in an overall elliptical polarization with a rotated major axis at the output of the waveguide. If the eigenmodes are circular, the output polarization is a linear polarization as well but rotated by a certain angle. By determining the output polarization state for a given input state, the eigenmodes of the slab waveguide can be computed.

As illustrated in Fig. 2.11 for the experimental setup, we used an intensity stabilized He-Ne laser for a light source and a Faraday isolator after the laser to prevent any undesired back-reflection into the laser cavity from deteriorating

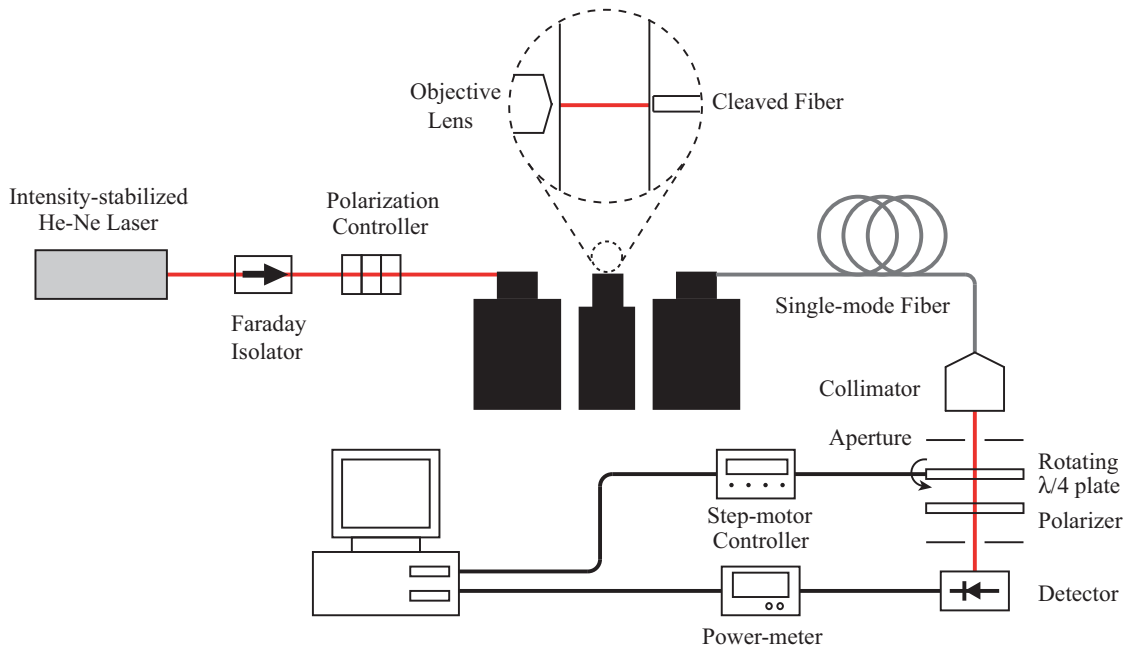


Figure 2.11: Experimental setup for polarization analysis for chiral waveguide.

the laser stabilization. Light is then directed through a polarization controller to launch a specific polarization into the waveguide under measurement. An objective lens was used for input coupling and a cleaved single mode fiber was used for output coupling, both mounted on a 3-axis translation stage, allowing accurate and stable alignment. The light signal travels through the additional single mode fiber after the waveguide, and it is collimated and detected after passing through a polarization analyzer section consisting of a rotating quarter waveplate and a linear polarizer. The quarter waveplate is mounted on a rotating step motor controlled by a computer.

The polarization analyzer section in Fig. 2.11 can be described using Stokes

vector and Mueller matrix representation. We can write a relationship,

$$\begin{aligned}
& \mathbf{S}' = \mathbf{M} \cdot \mathbf{S} \\
& = \mathbf{LP}(0) \cdot \mathbf{QWP}(\theta) \cdot \mathbf{S} \\
& = \begin{bmatrix} \frac{1}{2} & \frac{1}{2} & 0 & 0 \\ \frac{1}{2} & \frac{1}{2} & 0 & 0 \\ 0 & 0 & 0 & 0 \\ 0 & 0 & 0 & 0 \end{bmatrix} \begin{bmatrix} 1 & 0 & 0 & 0 \\ 0 & \cos^2 2\theta & \sin 2\theta \cos 2\theta & -\sin 2\theta \\ 0 & \sin 2\theta \cos 2\theta & \sin^2 2\theta & \cos 2\theta \\ 0 & \sin 2\theta & -\cos 2\theta & 0 \end{bmatrix} \begin{bmatrix} S_0^{\text{in}} \\ S_1^{\text{in}} \\ S_2^{\text{in}} \\ S_3^{\text{in}} \end{bmatrix}, \quad (2.54)
\end{aligned}$$

where \mathbf{S} is the Stokes vector describing the SOP we want to determine, and $\mathbf{LP}(0)$ and $\mathbf{QWP}(\theta)$ are the 4×4 Mueller matrices representing a fixed horizontal linear polarizer and a rotating quarter waveplate with an azimuthal angle θ with respect to the horizontal axis, respectively. From Eq. 2.54, the S'_0 -component in $\mathbf{S}' = (S'_0, S'_1, S'_2, S'_3)$ is given by

$$S'_0(\theta) = \frac{1}{2} \cdot S_0 + \frac{1}{2} \cos^2 2\theta \cdot S_1 + \frac{1}{4} \cos 4\theta \cdot S_2 - \frac{1}{2} \cos 2\theta \cdot S_3, \quad (2.55)$$

which is a function of the Stokes parameters S_0, S_1, S_2 and S_3 in \mathbf{S} that we want to determine, and it is equivalent to the total intensity I_o measured by a detector, assuming the detector is polarization insensitive. Once we measure the intensity at varying angles of θ , the unknown SOP represented by \mathbf{S} can be obtained from linear regression.

We should recognize, however, that the Mueller matrix of the fiber used for output coupling must be accounted for in order to obtain the SOP at the output of the waveguide (or equivalently at the input of the fiber). This can be done

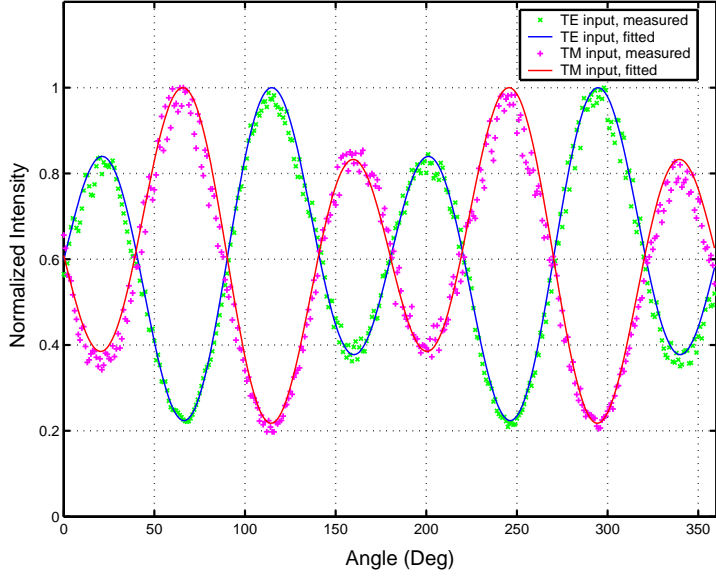
by a calibration process in which three different input polarizations, $[s_1, s_2, s_3]^3 = [1 \ 0 \ 0]$, $[0 \ 1 \ 0]$ and $[0 \ 0 \ 1]$ representing horizontal linear polarization, 45° linear polarization and RHC polarization, respectively, are launched into the fiber and the resulting output SOP for each case is determined from the linear regression as above [20]. This calibration procedure finds a characteristic 3×3 Mueller matrix⁴ $\mathbf{M}_{\text{fiber}}$ [21] that determines the SOP at the output of the fiber for a given input state. The matrix $\mathbf{M}_{\text{fiber}}$ can then be inverted to determine the SOP at the input of the fiber (and thus the output of the chiral waveguide) when the SOP at the output of the fiber is known.

Figure 2.12 shows the measurement results to determine the Stokes parameters corresponding to the polarization states of the waveguide modes after the additional single mode fiber. The dots represent the detected optical power as a function of θ , the angle of the fast axis of a rotating quarter waveplate with respect to the transmission axis of a fixed linear polarizer for two input polarizations \mathbf{s}^I of TE and TM. As discussed above, from linear curve fitting and after taking into account $\mathbf{M}_{\text{fiber}}$, we obtained polarization states at the waveguide output \mathbf{s}^F

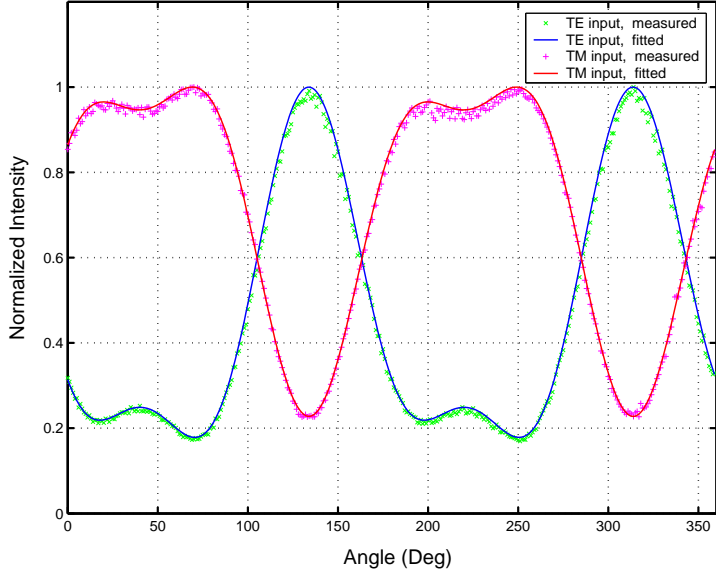
³ $[s_1, s_2, s_3]$ is a normalized Stokes vector obtained by dividing the 4-Stokes vector by the total optical power S_0 , i.e., $s_1 = S_1/S_0$, $s_2 = S_2/S_0$, $s_3 = S_3/S_0$.

⁴When we ignore the loss in the fiber, it can be considered as a unitary optical system and represented by the 3×3 Mueller matrix, a subset of a 4×4 Mueller matrix in which the first row and the first column is always $[1000]$ and $[1000]^T$ for the unitary optical component.

$$\mathbf{M}_{\text{fiber}} = \begin{bmatrix} m_{11} & m_{12} & m_{13} \\ m_{21} & m_{22} & m_{23} \\ m_{31} & m_{32} & m_{33} \end{bmatrix}$$



(a) ML-224



(b) ML-226

Figure 2.12: Detected optical power as a function of the angle between the rotating quarter waveplate and polarizer to determine the Stokes parameters corresponding to the polarization states of the waveguide modes. The solid lines fit to Eq. 2.55 for slab waveguides fabricated from (a) ML-224 and (b) ML-226.

for ML-224 waveguide

$$\mathbf{s}_{\text{TE input}}^F = \begin{bmatrix} 0.75 \\ -0.42 \\ 0.50 \end{bmatrix}, \quad \mathbf{s}_{\text{TM input}}^F = \begin{bmatrix} -0.72 \\ 0.45 \\ -0.51 \end{bmatrix}, \quad (2.56)$$

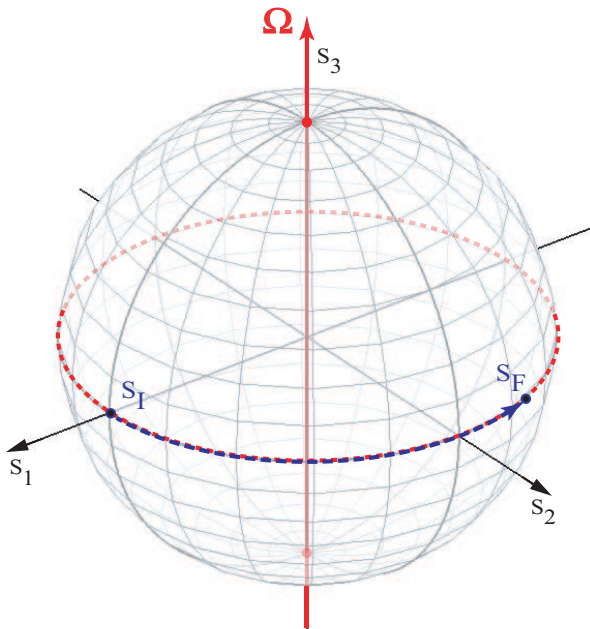
and for ML-226 waveguide

$$\mathbf{s}_{\text{TE input}}^F = \begin{bmatrix} 0.55 \\ -0.06 \\ -0.81 \end{bmatrix}, \quad \mathbf{s}_{\text{TM input}}^F = \begin{bmatrix} -0.53 \\ 0.08 \\ -0.82 \end{bmatrix}. \quad (2.57)$$

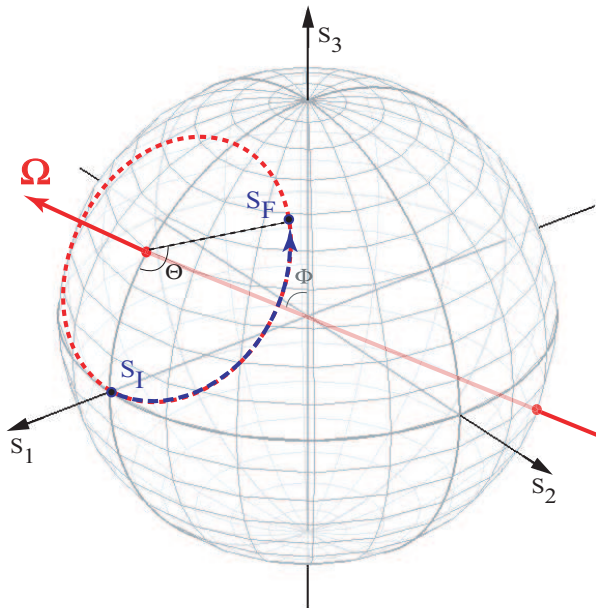
Next, we want to obtain the Stokes parameters describing the eigenstates of the waveguide from the SOP at the waveguide output for a given input polarization. The continuous evolution of the polarization states through the waveguide can be described by

$$\frac{d\mathbf{S}}{dz} = \boldsymbol{\Omega} \times \mathbf{S}, \quad (2.58)$$

where $\boldsymbol{\Omega}$ is the waveguide eigenmode with projections Ω_1 , Ω_2 , and Ω_3 defined in the same coordinate space as the Stokes vector \mathbf{S} . The above equation states that while the light signal propagates down the waveguide from any initial position, the evolution of the polarization state continuously traces out a circular orbit perpendicular to an axis connecting orthogonal eigenstates on the Poincare sphere. The evolution from the initial state \mathbf{s}^I to the final state \mathbf{s}^F can be easily visualized on the Poincare sphere as illustrated in Fig. 2.13 [22]. For example, when the eigenstates are circularly polarized modes, in other words, when the vector $\boldsymbol{\Omega}$ is



(a) Circularly polarized eigenstates



(b) Elliptically polarized eigenstates

Figure 2.13: Continuous evolution of polarization states traces out a circular orbit perpendicular to an axis connecting orthogonal eigenstates on the Poincaré sphere. (a) For circularly polarized eigenstates, the initial TE input polarization moves along the equator and remains a linear polarization rotating continuously. (b) For elliptically polarized eigenstates, the initial TE input polarization evolves into an elliptical polarization in general.

directed along the S_3 axis as shown in Fig. 2.4(a), the initial TE ($\mathbf{s} = [1 \ 0 \ 0]$) input polarization moves along the equator and remains a linear polarization rotating continuously. If the initial polarization state is represented by a point either at the north pole (RHC, $\mathbf{s}^I = [0 \ 0 \ 1]$) or at the south pole (LHC, $\mathbf{s}^I = [0 \ 0 \ -1]$), the SOP does not change. On the other hand, when eigenstates are elliptically polarized modes as shown in Fig. 2.4(b), the initial TE input polarization becomes an elliptical polarization in general. As discussed in section 2.2.2, the eigenmodes for a chiral planar waveguide are elliptical polarizations in general with major axes on either the x or y axis, which correspond to the points on the $S_1 - S_3$ meridian plane. So the eigenvector $\boldsymbol{\Omega}$ can be written as

$$\boldsymbol{\Omega} = \begin{bmatrix} \sin \Phi \\ 0 \\ \cos \Phi \end{bmatrix}, \quad (2.59)$$

where Φ is the angle between the S_3 axis and $\boldsymbol{\Omega}$ as depicted in Fig. 2.13. In terms of two angles Φ and Θ , the relationship between \mathbf{s}^I and \mathbf{s}^F can be written as

$$\mathbf{s}^F = \mathbf{R}_{S_2}(-\Phi) \cdot \mathbf{R}_{S_3}(\Theta) \cdot \mathbf{R}_{S_2}(\Phi) \cdot \mathbf{s}^I \quad (2.60)$$

where \mathbf{R}_{S_2} and \mathbf{R}_{S_3} are the matrices for rotational vector transformation with

respect to the S_2 and S_3 axis, respectively, and they are given by

$$\mathbf{R}_{S_2}(\Phi) = \begin{bmatrix} \cos \Phi & 0 & -\sin \Phi \\ 1 & 1 & 0 \\ \sin \Phi & 0 & \cos \Phi \end{bmatrix}, \quad (2.61)$$

$$\mathbf{R}_{S_3}(\Theta) = \begin{bmatrix} \cos \Theta & \sin \Theta & 0 \\ -\sin \Theta & \cos \Theta & 0 \\ 0 & 0 & 1 \end{bmatrix}. \quad (2.62)$$

For the TE input polarization ($\mathbf{s}^I = [1 \ 0 \ 0]$), after some algebraic manipulation with trigonometric identities, we get

$$\begin{aligned} s_1^F &= 1 - 2 \cos^2 \Phi \sin^2 \frac{\Theta}{2}, \\ s_2^F &= 2 \cos \Phi \sin \frac{\Theta}{2} \cos \frac{\Theta}{2}, \\ s_3^F &= 2 \cos \Phi \sin \Phi \sin^2 \frac{\Theta}{2}, \end{aligned} \quad (2.63)$$

and we can compute the angles Φ_{TE} and Θ_{TE} ,

$$\Phi_{TE} = \tan^{-1} \left(\frac{s_3^F}{1 - s_1^F} \right), \quad (2.64)$$

$$\Theta_{TE} = 2 \tan^{-1} \left(\frac{s_3^F}{s_2^F \sin \Phi_{TE}} \right). \quad (2.65)$$

Similarly for the TM input polarization ($\mathbf{s}^I = [-1 \ 0 \ 0]$),

$$\Phi_{TM} = \tan^{-1} \left(\frac{-s_3^F}{1 + s_1^F} \right), \quad (2.66)$$

$$\Theta_{TM} = 2 \tan^{-1} \left(\frac{s_3^F}{s_2^F \sin \Phi_{TM}} \right). \quad (2.67)$$

For ML-224 waveguide

$$\boldsymbol{\Omega}_{\text{TE input}} = \pm \begin{bmatrix} 0.88 \\ 0 \\ 0.47 \end{bmatrix}, \quad \boldsymbol{\Omega}_{\text{TM input}} = \pm \begin{bmatrix} -0.90 \\ 0 \\ -0.44 \end{bmatrix}, \quad (2.68)$$

and for the ML-226 waveguide,

$$\boldsymbol{\Omega}_{\text{TE input}} = \pm \begin{bmatrix} 0.88 \\ 0 \\ -0.48 \end{bmatrix}, \quad \boldsymbol{\Omega}_{\text{TM input}} = \pm \begin{bmatrix} -0.88 \\ 0 \\ 0.47 \end{bmatrix}, \quad (2.69)$$

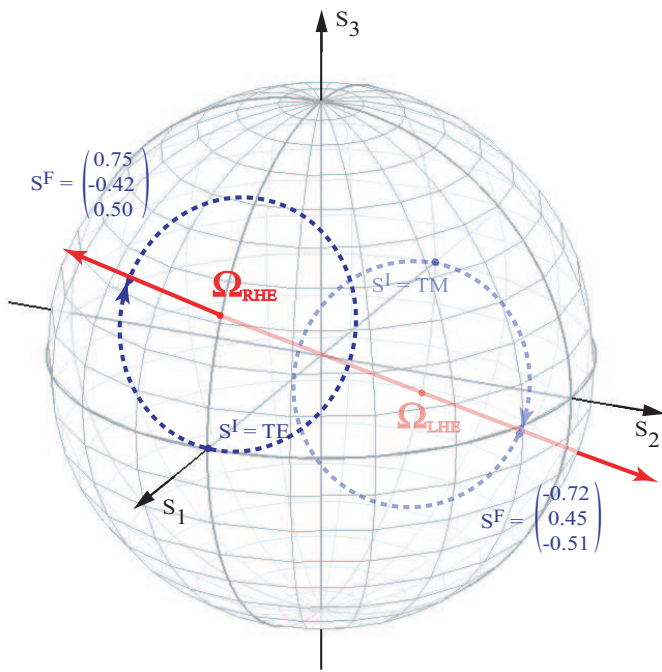
Since s_3 for the polarization ellipse with major axes on either the x or y axis is given by

$$s_3 = \frac{2E_x E_y}{E_x^2 + E_y^2}, \quad (2.70)$$

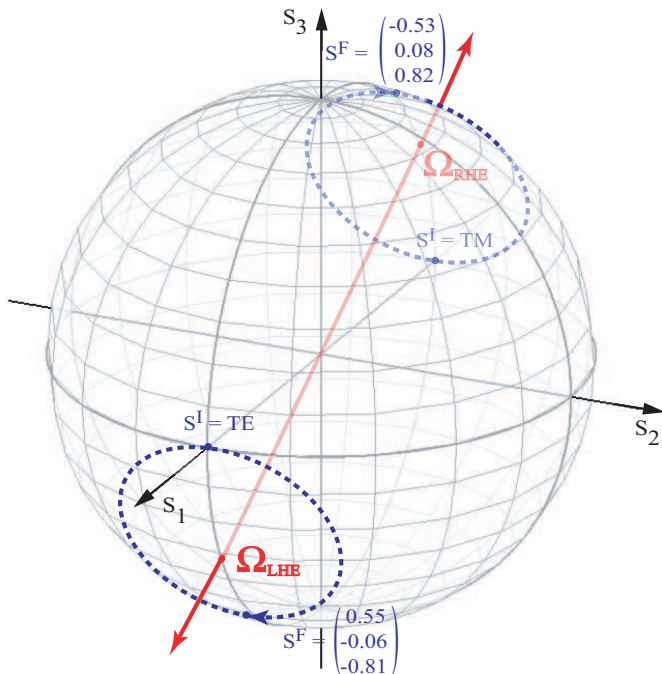
it can be related to the ellipticity g when $n_{\text{eff}} \approx n_g$ as in

$$s_3 \approx \frac{2g}{1 + g^2} \quad \text{for } n_{\text{eff}} \approx n_g. \quad (2.71)$$

From the above relation, the ellipticity parameter g is approximately 0.25 for the waveguides from both ML-224 and ML-226. Figure 2.14 illustrates the evolution of the SOP through the chiral waveguides fabricated from ML-224 and ML-226. In order to look at the quantitative property of how the SOP evolves along the waveguide as a function of the propagation distance z and the difference in mode effective indices $n_{\text{eff}}^{\text{LHE}_0} - n_{\text{eff}}^{\text{RHE}_0}$, we can multiply a scale factor $k_0(n_{\text{eff}}^{\text{LHE}_0} - n_{\text{eff}}^{\text{RHE}_0})$ to the $\boldsymbol{\Omega}$ in Eq. 2.58. However, often an alternative approach using the Jones representation can be more intuitive and useful. From two orthonormal Jones



(a) ML-224



(b) ML-226

Figure 2.14: Evolution of polarization through the chiral waveguides from (a) ML-224 and (b) ML-226.

vectors for the basis vectors corresponding to elliptical polarization states, which are given by

$$\mathbf{E} = E_r \hat{\mathbf{r}} + E_l \hat{\mathbf{l}}, \quad (2.72)$$

$$\hat{\mathbf{r}} = \frac{1}{\sqrt{a^2 + b^2}} \begin{bmatrix} a \\ jb \end{bmatrix}, \quad (2.73)$$

$$\hat{\mathbf{l}} = \frac{1}{\sqrt{a^2 + b^2}} \begin{bmatrix} b \\ -ja \end{bmatrix}, \quad (2.74)$$

$$\hat{\mathbf{r}}^\dagger \cdot \hat{\mathbf{r}} = \hat{\mathbf{l}}^\dagger \cdot \hat{\mathbf{l}} = 1, \quad \hat{\mathbf{r}}^\dagger \cdot \hat{\mathbf{l}} = \hat{\mathbf{l}}^\dagger \cdot \hat{\mathbf{r}} = 0, \quad (2.75)$$

we can construct a unitary transformation matrix representing a change of basis states from Cartesian to elliptical

$$\mathbf{U} = \frac{1}{\sqrt{a^2 + b^2}} \begin{bmatrix} a & -jb \\ b & ja \end{bmatrix}, \quad (2.76)$$

satisfying

$$\begin{bmatrix} E_r \\ E_l \end{bmatrix} = \mathbf{U} \begin{bmatrix} E_x \\ E_y \end{bmatrix}, \quad (2.77)$$

Now for the Jones vector after propagating a distance d through the chiral waveguide with linear basis, we can write

$$\begin{bmatrix} E'_x \\ E'_y \end{bmatrix}_{z=d} = \mathbf{U}^\dagger \cdot \mathbf{M}_{wg} \cdot \mathbf{U} \cdot \begin{bmatrix} E_x \\ E_y \end{bmatrix}_{z=0}, \quad (2.78)$$

where

$$\mathbf{M}_{wg} = \begin{bmatrix} e^{-jk_0 n_r d} & 0 \\ 0 & e^{-jk_0 n_l d} \end{bmatrix}. \quad (2.79)$$

If we put $[E_x \ E_y] = [1 \ 0]$, $n_r = n_{\text{eff}}^{\text{RHE}_0}$, and $n_l = n_{\text{eff}}^{\text{LHE}_0}$ into Eq. 2.78, we can achieve the polarization state $[E'_x \ E'_y]$ at $z = d$ evolved from TE input at $z = 0$.

Note that the angle Θ in Fig. 2.4 is related to the propagation distance z and $\Delta n_{\text{eff}} = n_{\text{eff}}^{\text{LHE}_0} - n_{\text{eff}}^{\text{RHE}_0}$ such that

$$\Theta = 2\rho_{\text{eff}}z, \quad (2.80)$$

$$\rho_{\text{eff}} = \frac{\pi}{\lambda}(n_{\text{eff}}^{\text{LHE}_0} - n_{\text{eff}}^{\text{RHE}_0}). \quad (2.81)$$

Therefore, $\rho_{\text{eff}}z = \pi$ corresponds to one complete circle around the eigenstate Ω . The measured waveguide lengths d are about 16.5 mm and 11.7 mm, and from the numerical calculations as shown in Fig. 2.9, the mode effective index differences are approximately $\Delta n_{\text{eff}} = 5 \times 10^{-5}$ and $\Delta n_{\text{eff}} = -8 \times 10^{-5}$ for the ML-224 and ML-226 waveguides, respectively. Once these values are plugged into Eq. 2.80, we can notice that, for both waveguides, the polarization states evolve in such a way that they reach s^F as given in Eqs. 2.56 and 2.57 after making one full complete circle. The experimental results show that the eigenmodes of the chiral waveguides are indeed RHE and LHE, and they are in excellent agreement with what is expected from the theory in [8] in terms of the mode ellipticity and the SOP evolution through the chiral-core planar waveguides.

Nevertheless, these Ω_3 values are not large enough for these materials to be used for a polarization controller or a TE/TM converter. We discussed that the Ω_3 of the eigenmode must be very close to unity, corresponding to predominantly right- and left-handed circularly polarized waveguide modes. This can be achieved

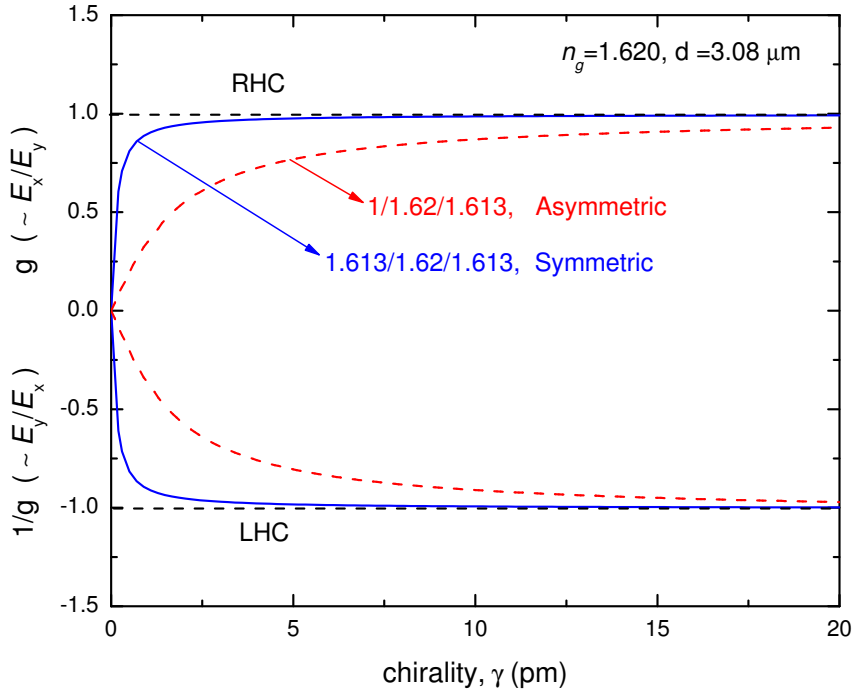


Figure 2.15: Calculation of mode ellipticity of RHE_0 and LHE_0 as a function of given material chirality γ for the symmetric and asymmetric chiral-core planar waveguides. The dotted line is associated with an asymmetric structure with refractive indices $n_g = 1.62$, $n_0 = 1.00$ and $n_s = 1.613$, and the solid line with a symmetric structure with indices $n_g = 1.62$ and $n_0 = n_s = 1.613$.

principally from larger specific rotatory power (or equivalently larger chirality γ) of the material itself.

Figure 2.15 shows a calculation of the mode ellipticity of RHE_0 and LHE_0 as a function of given material chirality γ for the symmetric and asymmetric chiral-core planar waveguides. The dotted line is associated with an asymmetric structure with refractive indices $n_g = 1.62$, $n_0 = 1.00$ and $n_s = 1.613$, and the solid line with a symmetric structure with indices $n_g = 1.62$ and $n_0 = n_s = 1.613$. From the plot,

it is evident that, in order to have predominantly circular eigen-polarizations, a chirality $\gamma > 20$ pm, or equivalently $\rho > 300$ deg/mm is required in the asymmetric waveguide. On the other hand, in the symmetric waveguide, near circularly polarized eigenstates can be obtained with considerably a lower chirality $\gamma \approx 4 - 5$ pm, or equivalently $\rho = 45 - 60$ deg/mm.

The desire for circularly polarized modes, rather than just elliptically polarized modes, is driven by the goal of achieving a pure polarization rotator in a waveguide, i.e. a device for which a linearly polarized input is rotated to some other linearly polarized state for any propagation length. Because even moderate amounts of linear birefringence can overpower the effects of optical activity, an essential requirement that must be fulfilled in order to attain this goal is the synthesis of a chiral material that is isotropic in a solid film.

2.5 Other chiral materials

Other than the chiral single molecules, ML-224 and ML-226, we have characterized several organic chiral materials from strong collaborations with university chemists: Prof. Mark Green's group at New York Polytechnic University, Prof. Andrzej Rajca's group at the University of Nebraska, and Prof. Lin Pu's group at the University of Virginia. Although the improvement in material chirality was modest so that they were not realized into actual devices, here we summarize the characteristics of those materials including optical rotatory power and index dispersion measured using the same method described in section 2.4.

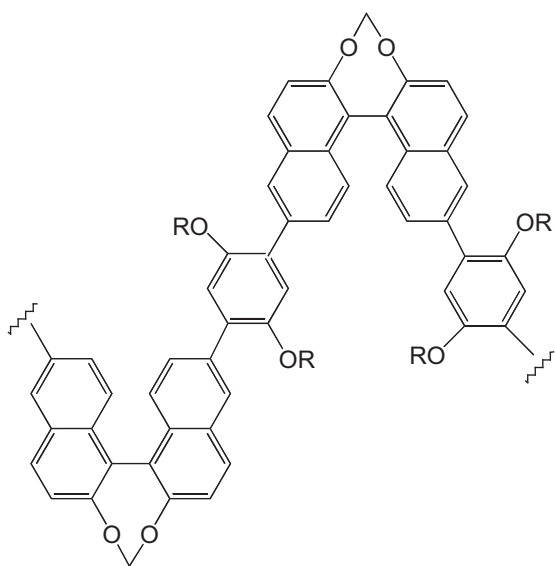


Figure 2.16: Chemical structure of the main chain binaphthyl polymer, Zhang-IV-37 with R = n-C₆H₁₃.

2.5.1 Binaphthyl polymer

A main chain binaphthyl polymer identified as Zhang-IV-37 shown in Fig. 2.16 was supplied by the University of Virginia. The glass transition temperature T_g is expected to be in the range of 200 °C and the specific rotatory power measured in solution is $[\alpha]_D^{25} = -711^\circ$.

For characterization, a 0.95 μm thick sample was prepared on a UV-grade fused quartz by dissolving the solid powder in cyclohexanone to make a 10 % solution and spin-casting followed by curing in an oven at 100 °C for two hours. The optical rotatory power measured is -8.7 deg/mm at 670 nm, which is almost twice as big as ML-224 and ML-226. However, it exhibited a marked linear birefringence of

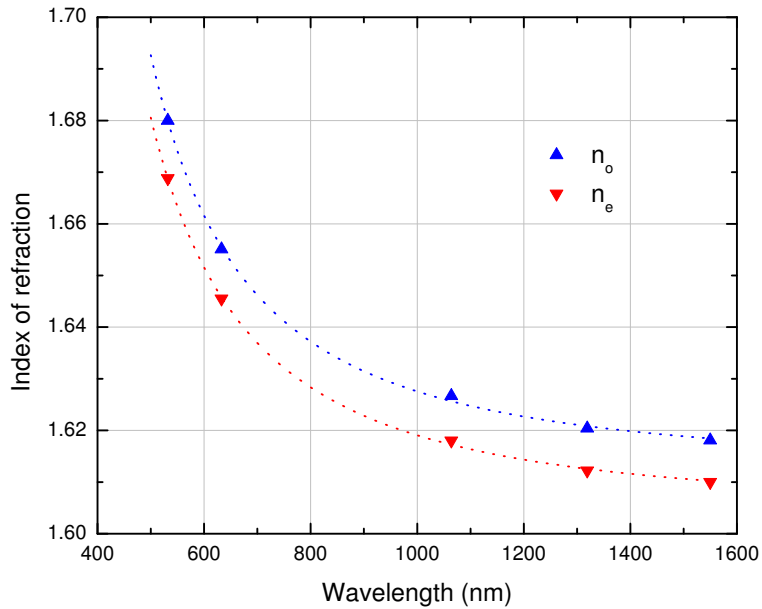


Figure 2.17: Index of refraction dispersion measured with a Metricon™ prism coupler for the polybinaphthyl Zhang-IV-37 in thin solid films, which exhibited a marked large linear birefringence, ~ -0.01 .

~ -0.01 as shown in Fig. 2.17.

From Eq. 2.21 with Eq. 2.22, we can notice that this appreciably large linear birefringence is almost 300 times bigger than the circular birefringence, and hence the eigenstates of the planar waveguide would be approximately TE/TM modes.

2.5.2 Polymethine dyes

A chiral polymethine dye identified as HT-dye14 was supplied by NY Polytechnic University and its polymer composite with a poly(butyl methacrylate-co-methyl methacrylate) was characterized. The glass transition temperature T_g for HT-dye14 and poly(butyl methacrylate-co-methyl methacrylate) are about 122 °C and

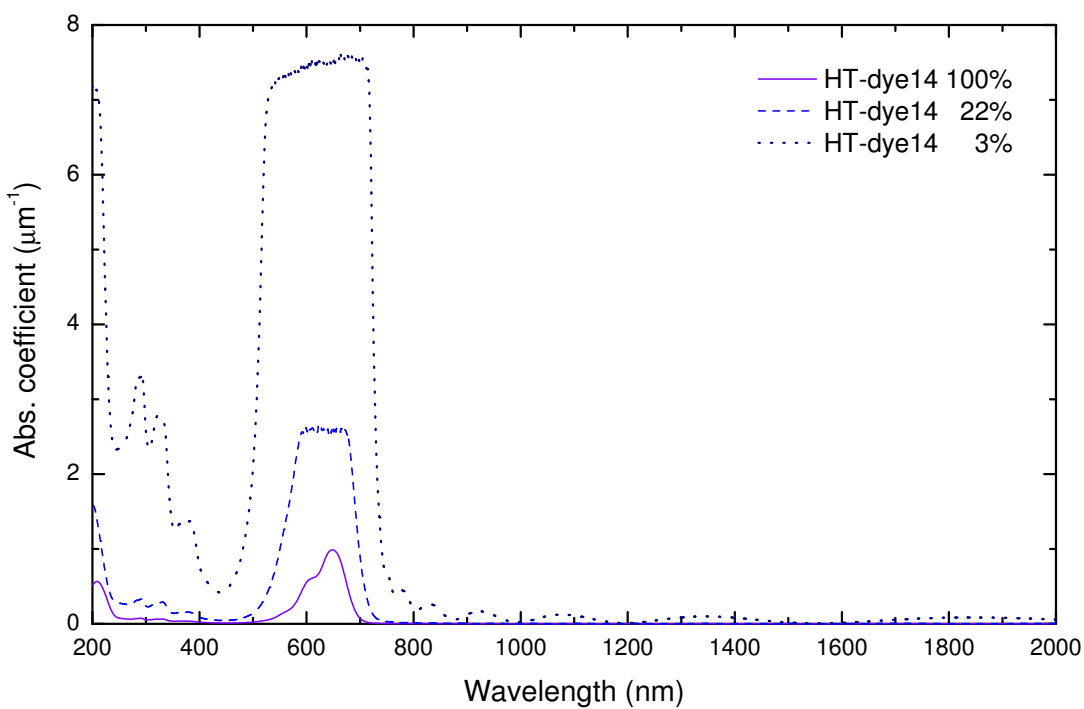


Figure 2.18: UV-Vis-IR spectra measured with a Cary 5000 spectrophotometer for HT-dye14 in poly(butyl methacrylate-co-methyl methacrylate) copolymer.

64 °C, respectively. Due to the $\pi-\pi^*$ absorption of the chromophore in polymethine dyes, there is a strong absorption in the 550–700 nm spectral range. Figure 2.18 shows UV-Vis-IR spectra for the absorption coefficient measured with a Cary 5000 spectrophotometer for three samples with different concentrations of HT-dye14 in the copolymer.

Both materials were dissolved separately in chloroform and mixed afterwards. After casting the film, it was cured at a temperature of 170 °C, substantially above the T_g , for an hour because annealing can be quite effective in removing

birefringence arising from strain in the evaporation process [23]. Optical rotatory power measured at 751 nm was about -3 deg/mm for the sample consisting of 22 % dye in the copolymer, and -72 deg/mm for the sample from pure HT-dye14 without the copolymer. The linear birefringence of pure HT-dye14 is 0.004–0.01 depending upon wavelength. As we decrease the concentration of polymethine dye molecules, the material composite becomes isotropic. For example, the sample consisting of 22 % dye was isotropic within experimental uncertainty, ~ 0.0001 , but with a trade-off in optical activity, -3 deg/mm.

2.5.3 (7)Helicene

Thiophene-based carbon-sulfur (7)helicene chiral molecular glass was supplied by the University of Nebraska [24]. T_g is about 67 °C and the specific rotatory power measured in solution is $[\alpha]_D^{25} = +1166^\circ$. A 5.6 μm thick sample was made by drop-dispensing from the solution in cyclohexanone. The optical rotatory powers were 11 deg/mm and 6 deg/mm at wavelengths of 670 nm and 850 nm, respectively, and the linear birefringence was ~ 0.0003 .

2.5.4 Bridged binaphthyl with chromophore

Bridged binaphthyls with chromophore groups attached, identified as HT-386, was supplied by NY Polytechnic University. A 2 μm thick sample was prepared by spin-casting the solution in cyclohexanone. The optical rotatory power measured was about 11 deg/mm at 670 nm. The refractive index measurement shows the sample is isotropic within the experimental uncertainty (~ 0.0001). However, T_g

is around 25 °C, so it was difficult to fabricate waveguide structures.

2.6 Summary

In this chapter, we discussed the unique polarization properties of optical chiral waveguides that can be used for integrated-optic polarization converters or polarization modulators provided that low loss amorphous films of sufficient chirality can be fabricated. Relatively recently, new modeling results for (a)symmetric planar waveguides with chiral cores showed that eigenmodes are elliptically polarized modes, in general, and the polarization ellipticity depends on the chirality that is related to the bulk rotatory power of material. For an important design consideration, dependence of mode ellipticity on cladding index was discussed. Through a detailed experimental polarization analysis on asymmetric chiral-core planar waveguides fabricated from binaphthyl-based organic single molecules with a layer of SiON for the cladding layer, we showed that eigenmodes in planar chiral-core waveguides are indeed two orthonormal elliptical polarizations, and achieved waveguide modes with a polarization eccentricity of 0.25, which agrees very well with the theory. Although the achieved mode ellipticity is not large enough to meet the requirement – predominant circularly polarized modes – for practical applications, this is, to the best of our knowledge, the first experimental demonstration of the mode ellipticities for the transverse electric field of the chiral-core optical waveguides. As we discussed, even in the case of weakly confined symmetric waveguide structure, the chirality $\gamma > 5pm$ is required for near circularly

polarized eigenmodes. Characterizations and feasibilities of several other chiral materials were also discussed. Unfortunately, none of these materials exhibited both the appreciable material chirality and negligible linear birefringence at the same time. The design and synthesis of such an isotropic material with a high degree of chirality, which also extends the ORD maxima into the near infrared, is in progress.

CHAPTER 3

ORGANIC MAGNETO-OPTIC MATERIAL

3.1 Magneto-optic effect

The magneto-optic effect refers to a phenomenon in which light propagating through a medium experiences birefringence in the presence of a magnetic field. There are two well-known magneto-optic effects, distinguished by the direction of the magnetic field with respect to the direction of light propagation, Faraday and Cotton-Mouton. The Cotton-Mouton effect arises from a linear birefringence proportional to the square of the transverse magnetic field flux density. The magnetic field-induced linear birefringence Δn can be written as

$$\begin{aligned}\Delta n &= n_{\parallel} - n_{\perp} \\ &= C_{\text{CM}} \lambda B_t^2,\end{aligned}\tag{3.1}$$

where n_{\parallel} and n_{\perp} are the refractive indices for light polarized parallel and perpendicular to the magnetic field, respectively, C_{CM} is the Cotton-Mouton coefficient, and B_t is the transverse component of the magnetic field. Therefore, the phase

difference $\Delta\phi_{\text{CM}}$ between the two orthogonal polarizations is given by

$$\begin{aligned}\Delta\phi_{\text{CM}} &= \frac{2\pi}{\lambda} \Delta nl \\ &= 2\pi C_{\text{CM}} B_{\text{t}}^2 l,\end{aligned}\quad (3.2)$$

where l is the effective optical path length through a medium.

On the other hand, the Faraday effect comes from a circular birefringence linearly proportional to the axial component of the magnetic field. Between these two, the Faraday effect is well studied because of its practical importance for useful optical components, such as isolators, circulators, polarization modulators, and sensors including current sensors and magnetic field sensors.

The Faraday effect, the magnetic field-induced optical activity, was discovered in 1845 by M. Faraday. The plane of polarized light can be rotated by allowing light to propagate through a medium with inversion symmetry in the presence of a magnetic field. The angle of rotation is given by

$$\phi_F = V \int \mathbf{B} \cdot d\mathbf{l}, \quad (3.3)$$

where \mathbf{B} is the magnetic flux density, $d\mathbf{l}$ is an infinitesimal displacement vector along the direction of propagation of light, and V is a proportional constant called Verdet constant. In words, the amount of polarization rotation is proportional to the strength of the longitudinal component of the magnetic field and the length of the medium the light propagates through.

The Verdet constant is associated with the specific material and in general varies with wavelength and temperature [25–27]. The units of V are often ex-

pressed in $[\text{rad}/\text{T} \cdot \text{m}]$ or $[\text{min}/\text{G} \cdot \text{cm}]$. By convention, a positive Verdet constant corresponds to a counter-clockwise rotation when light propagates parallel to an applied **B**-field and viewed from the direction toward which light is travelling (i.e. looking at the light source) [28, 29]. In other words, for $V > 0$, the plane of polarization rotates in the same direction as the current through a solenoid coil around the medium, regardless of the direction of light propagation. Note that this convention for the sense of rotation is opposite from the optical activity in a chiral medium, in which $\alpha > 0$ represents a clockwise rotation when looking at the light source as discussed in the previous chapter.

From the consideration of the reciprocity nature in optics, there is an important difference between the Faraday effect and optical chiral activity. In the Faraday effect, the rotation of polarization is non-reciprocal because the interaction of light with matter under a magnetic field breaks the time reversal symmetry and the parity conservation [30]. A detailed theoretical discussion on the origin of the magneto-optic effect from a quantum mechanical approach is beyond the scope of this thesis and will be omitted.

Most recently, a very high Verdet constant from an organic polymer thin film has been reported [31]. Although there is a lack of theoretical understanding on the physics of the high Verdet constants in organic polymers at this point, such kinds of materials are essential to constructing integrated-optic devices such as isolators and circulators from simple fabrication method of spin-casting and photolithography.

3.2 Balanced homodyne detection

To measure the Verdet constant associated with a particular material, we can simply increase an effective path length or use a strong magnetic field to produce a rotation angle large enough until it becomes detectable. However, in order to detect a small angle of rotation from a thin organic film with a typical thickness of $10 - 100 \mu\text{m}$ in a moderate magnetic field $< 100 \text{ Gauss}$, a measurement technique with high precision and improved signal-to-noise ratio is essential. One of the simplest ways to measure the Faraday rotation is based on the polarizer-analyzer configuration that we used to measure the optical rotatory power of a chiral thin film, but it suffers from poor measurement sensitivity and accuracy, on the order of a few mdeg. The method relies highly on the accuracy and repeatability of a step motor used in the measurement. A few other schemes for sensitive measurement have been reported [32, 33]. However, the sensitivity is generally worse than a *balanced homodyne detection* that we adopted in our experiment [34, 35].

In optical interferometry, in order to detect a phase or amplitude change in an optical signal, the signal and reference are mixed for phase comparison. When the reference frequency ω_{LO} from a local oscillator is slightly different from the signal frequency ω_s , the average current detected arises from an optical field at the difference frequency $\omega_{\text{LO}} - \omega_s$ (often referred to as the intermediate frequency, IF), but no other frequencies such as $2\omega_{\text{LO}}$ or $2\omega_s$ are detected simply because semiconductor detectors do not respond rapidly enough. The advantage of this *Heterodyne*

detection is that one can increase the S/N ratio by increasing the local oscillator power and achieve *shot-noise limit detection* in which shot noise dominates over all other noise contributions. On the other hand, when the frequency of the local oscillator is same as that of the signal ($\omega_{\text{LO}} = \omega_s$), but there is a relative phase difference, it is called *Homodyne detection*. In homodyne detection, the phase difference is transformed into an intensity change after an optical mixer, therefore the total intensity at the photodetector is determined by the relative phase difference between the signal and the local oscillator [36, 37].

In a balanced homodyne interferometry scheme designed to measure the Verdet constant with a high sensitivity and S/N ratio, a linearly polarized light oriented at 45° can be used as a probe beam instead of using two separate beams. Therefore, the two orthogonal principal polarizations – horizontal and vertical – can be treated as the two separate beams for the signal and the reference. Once the plane of polarization is rotated by a small angle after propagating through the magneto-optic sample placed in a magnetic field, the small amplitude changes are projected onto the corresponding principal components of a polarizing beam splitter as shown in Fig. 3.1.

In addition, if a sample is placed in an AC magnetic field, the rotation of polarization from an alternating magnetic flux density is transformed into an amplitude modulation along the principal axis after passing through the polarizing beam splitter. Because the amplitude changes along the principal axes are 180° out of phase from each other, by using a balanced photodetector consisting of two pho-

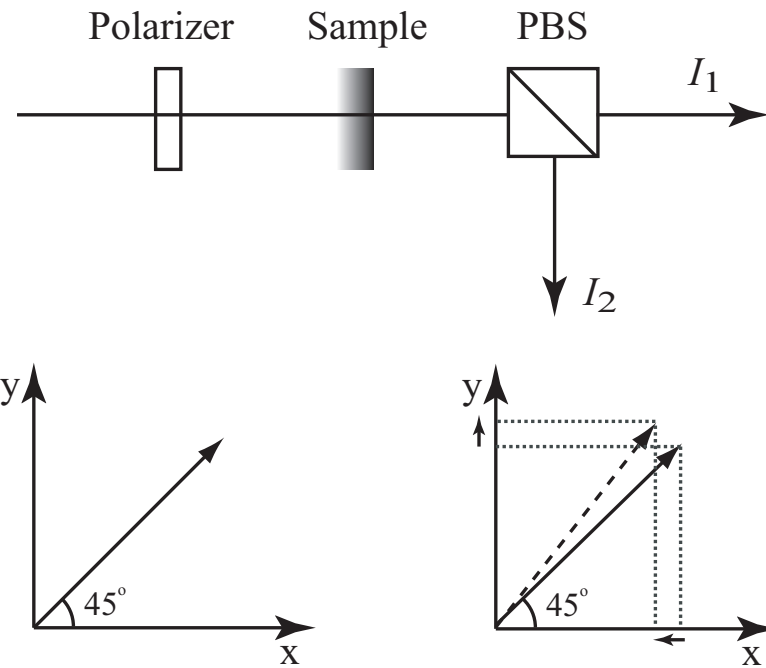


Figure 3.1: Schematics of balanced homodyne detection.

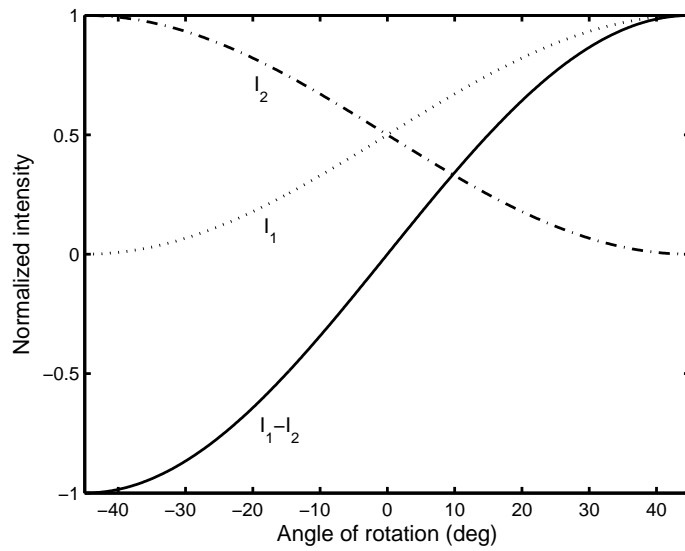


Figure 3.2: Normalized intensities along the principal axes I_1 , I_2 , and difference $I_1 - I_2$. The amplitude changes along the principal axes from rotation of polarization are 180° out of phase from each other.

todiodes and a differential amplifier, and a lock-in amplifier, we can minimize the amplitude noise of the optical field and maximize the sensitivity with a significant rejection of common-mode noise.

We can use the Jones formalism for a quantitative analysis of the balanced homodyne detection. The electric field E^1 and E^2 at each detector can be written as

$$\begin{bmatrix} E_x^{1,2} \\ E_y^{1,2} \end{bmatrix} = \mathbf{Pol}(\theta_p^{1,2}) \cdot \mathbf{HWP}(\theta_h) \cdot \mathbf{Rot}(\phi) \cdot \frac{1}{\sqrt{2}} \begin{bmatrix} 1 \\ 1 \end{bmatrix}, \quad (3.4)$$

where $\mathbf{Pol}(\theta_p^{1,2})$, $\mathbf{HWP}(\theta_h)$, and $\mathbf{Rot}(\phi)$ represent the Jones matrices for the polarizing beam splitter, the half-wave plate with the fast-axis oriented at θ_h , and the rotation by an angle of ϕ , respectively, which are given as

$$\mathbf{Pol}(\theta_p^{1,2}) = \begin{bmatrix} \cos^2 \theta_p^{1,2} & \sin \theta_p^{1,2} \cos \theta_p^{1,2} \\ \cos \theta_p^{1,2} \sin \theta_p^{1,2} & \sin^2 \theta_p^{1,2} \end{bmatrix}, \quad (3.5)$$

$$\mathbf{HWP}(\theta_h) = \begin{bmatrix} j \cos^2 \theta_h - j \sin^2 \theta_h & j \sin 2\theta_h \\ j \sin 2\theta_h & j \sin^2 \theta_h - j \cos^2 \theta_h \end{bmatrix}, \quad (3.6)$$

$$\mathbf{Rot}(\phi) = \begin{bmatrix} \cos \phi & -\sin \phi \\ \sin \phi & \cos \phi \end{bmatrix}. \quad (3.7)$$

Because the polarizing beam splitter is aligned in such a way that $\theta_p^1 = 0$ and $\theta_p^2 = \pi/2$, and each detector measures the intensity of the corresponding principal component (horizontal and vertical polarization), the electric fields E_1 and E_2 at

each detector from Eq. 3.4 can be written as

$$\begin{bmatrix} E_x^1 \\ E_y^1 \end{bmatrix} = \frac{1}{\sqrt{2}} \begin{bmatrix} \sin(2\theta_h - \phi) + \cos(2\theta_h - \phi) \\ 0 \end{bmatrix}, \quad (3.8)$$

$$\begin{bmatrix} E_x^2 \\ E_y^2 \end{bmatrix} = \frac{1}{\sqrt{2}} \begin{bmatrix} \sin(2\theta_h - \phi) - \cos(2\theta_h - \phi) \\ 0 \end{bmatrix}, \quad (3.9)$$

and the output from the balanced detector can be represented as

$$I \propto I_1 - I_2 \propto \mathbf{E}_1^\dagger \cdot \mathbf{E}_1 - \mathbf{E}_2^\dagger \cdot \mathbf{E}_2 \quad (3.10)$$

$$\propto \sin 2(2\theta_h - \phi) + \text{constant} \quad (3.11)$$

$$= A \sin 2(2\theta_h - \phi) + C. \quad (3.12)$$

When an alternating magnetic field is applied, the modulated intensity at a fixed bias point $\theta_h = \theta_{h0}$ is given by

$$\Delta I = -2A \cos 2(2\theta_{h0} - \phi) \Delta\phi, \quad (3.13)$$

$$\Delta\phi = VlB_0 \sin \omega t, \quad (3.14)$$

$$\phi_F = VlB_0. \quad (3.15)$$

Eq. 3.12 can be referred to as an *optical bias curve* or a *transfer curve*, which can be obtained from measuring the output from the balanced detector while rotating the half-wave plate without a magnetic field applied. Note that obtaining the optical bias curve is a necessary step for the absolute measurement of a rotation angle from the corresponding amplitude modulation. In other words, once we

obtain the A and C in the optical bias curve from curve fitting, we can convert the demodulated signal ΔI from the lock-in amplifier into the equivalent rotation angle of plane polarization.

Also note that the bias point θ_{h0} can be any arbitrary value for measuring the Faraday rotation, but the maximum demodulated signal $|\Delta I|$ from the lock-in amplifier can be achieved at $2\theta_{h0} = \phi$. This is the case of 45° input polarization and horizontal alignment of the fast axis of the half-wave plate. Even when there is a misalignment of the input polarizer or inherent linear birefringence in the sample, the bias point for maximum demodulation can be found from the optical bias curve.

3.3 Measurement of Verdet constant

In this section, we discuss the experimental measurement of the Verdet constant in detail and present the measurement result for terbium gallium garnet (TGG), one of the most popular Faraday materials used for free space optical isolators, and for the organic samples.

Figure 3.3 depicts the experimental setup we used to measure the Verdet constant. A Glan-Thompson polarizer with an extinction ratio better than 50 dB was used to produce a linearly polarized input oriented at 45° . The sample was placed in a Helmholtz coil through which a sinusoidal current was applied from a power supply controlled by a function generator. We used a KEPCO BOP70-12 power supply to amplify the voltage signal from a function generator to provide suffi-

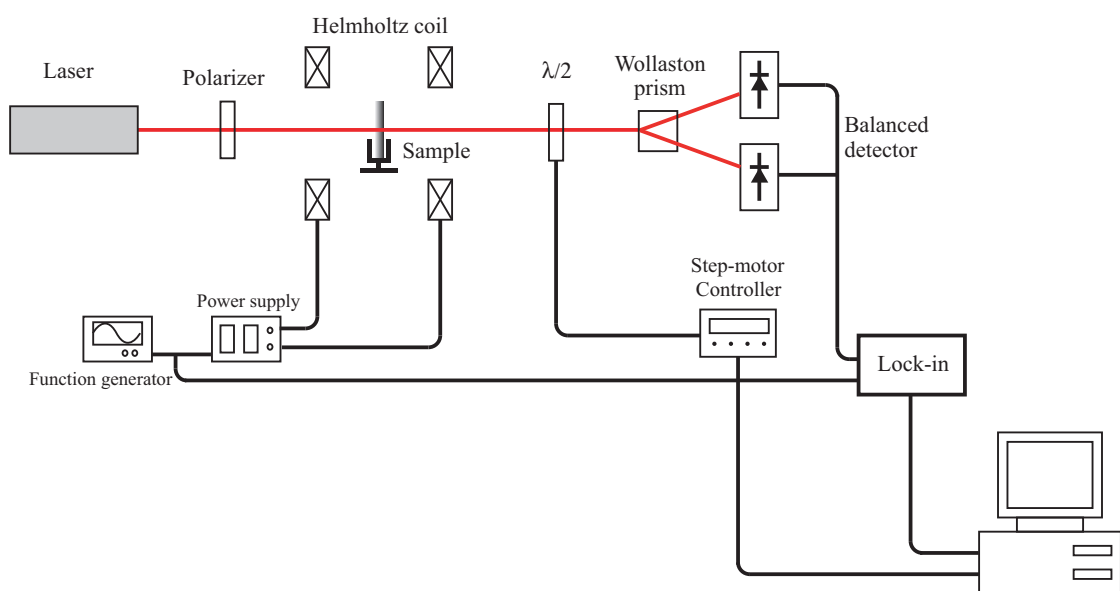


Figure 3.3: Experimental setup of balanced homodyne detection to measure the Verdet constant. The rotation of polarization through the sample placed in an alternating magnetic field is transformed into an amplitude modulation along the principal axis after passing through the Wollaston prism, and detected by a balanced detector.

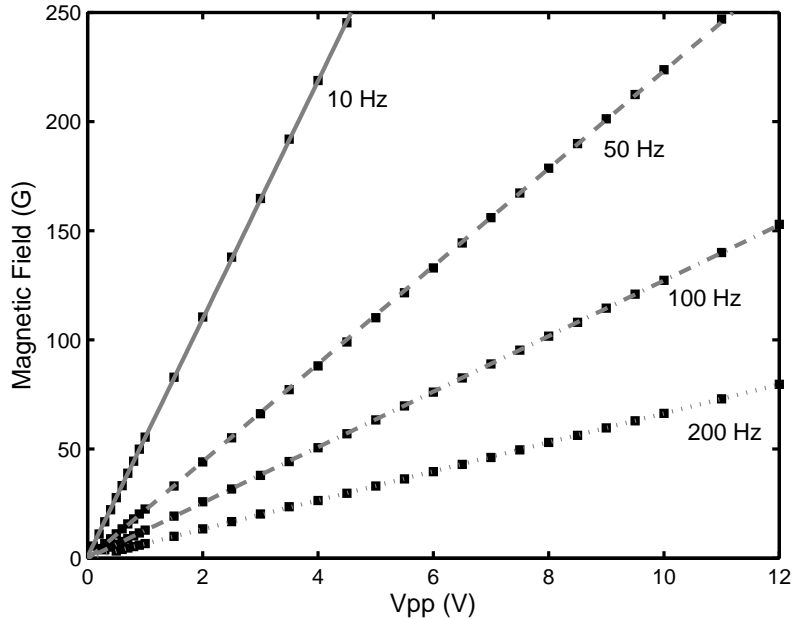


Figure 3.4: Calibration of the amplitude of alternating magnetic flux density inside the Helmholtz coil for a given input AC voltage signal to power supply. Due to the inductive impedance, the magnetic field decreases with increasing frequency.

cient current through the Helmholtz coil. After light passes through the Wollaston prism, the rotation of polarization from an alternating magnetic flux density is transformed into an amplitude modulation along the principal axis (horizontal and vertical), and detected by a New Focus balanced detector and a Signal Recovery lock-in amplifier.

As a first step, an alternating magnetic field flux density $B_0 \sin \omega t$ inside the Helmholtz coil for a given AC signal was calibrated using a gauss-meter from T.W. Bell. Figure 3.4 shows the amplitude of the AC magnetic field B_0 measured with an increasing peak-to-peak voltage amplitude at different frequencies from a function

generator. Due to the inductive impedance of the circuit $\sqrt{R^2 + \omega^2 L^2}$, the current flowing through the Helmholtz coil and hence the magnetic field decreases with increasing frequency. Because $1/f$ noise dominates over other noise sources at a low frequency detection, a modulation frequency of 100 Hz was chosen to reduce $1/f$ noise and produce a reasonably strong magnetic field at the same time. This choice was somewhat arbitrary, but we experimentally verified that the Faraday rotation measured with different modulation frequencies were indeed the same although it can affect the S/N ratio.

For a verification of our experimental procedure, we measured a 2 cm-long rod of TGG at wavelengths of 633 nm, 850 nm, 1300 nm, and 1550 nm. As we discussed in the previous section, the optical bias curve without applying magnetic field was obtained by measuring the output from the balanced detector while rotating the half-wave plate mounted on a computer-controlled step motor and fitting to Eq. 3.12 as shown in Fig. 3.5.

From the optical bias curve obtained, the demodulated signal from the lock-in amplifier representing the RMS value of amplitude modulation can be converted to an angle of rotation for a given applied magnetic field. Note that the demodulated signal for different magnetic flux density is averaged over one hundred data points. As shown in Fig 3.6, we can determine the Verdet constant by fitting the angles of rotation at different magnetic field values to a linear line, as indicated in Eqs. 3.13-3.15. The measured Verdet constant of TGG is -141 rad/T · m at a wavelength of 633 nm, which agrees well with a published value [25]. Note that

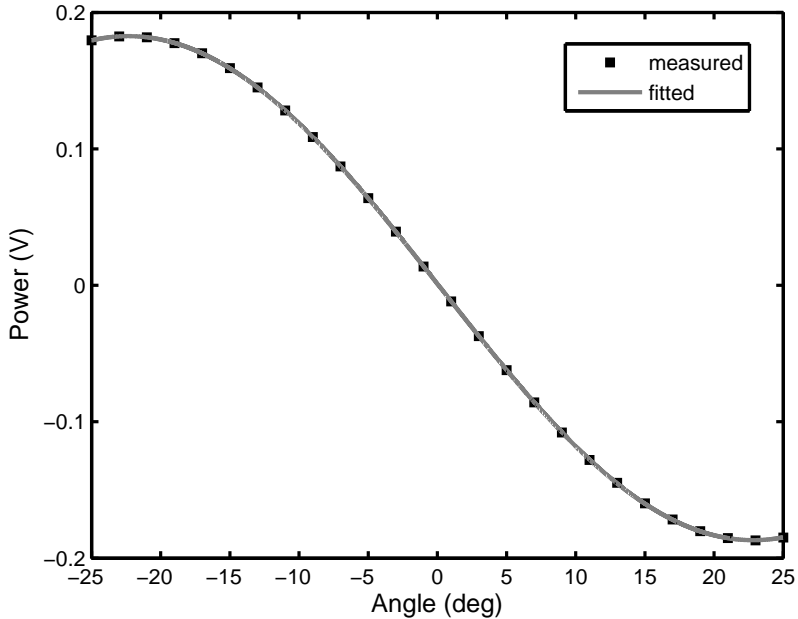


Figure 3.5: Optical bias curve without a magnetic field applied for a 2 cm-long rod of TGG sample obtained at wavelength 633 nm. The solid line is a fit to Eq. 3.12.

the Verdet constant of TGG is negative, indicating that this is a paramagnetic material. From the measurement at different wavelengths as shown Fig. 3.7, we can see that there is a wavelength dependence and the Verdet constant quickly drops as wavelength increases. The measured values of V are -71.1, -21.2, and -8.7 rad/T · m at wavelengths of 850 nm, 1300 nm, and 1550 nm, respectively.

Most recently, a very high Verdet constant from an organic polymer thin film was reported and drew attention for potential applications to integrated optic devices [31]. For this reason, thiophene based-organic samples identified as SJZ-87A (25 μ m), TK1V1292A320-A (100 μ m), and TK1V1292A320-N (100 μ m) were pro-

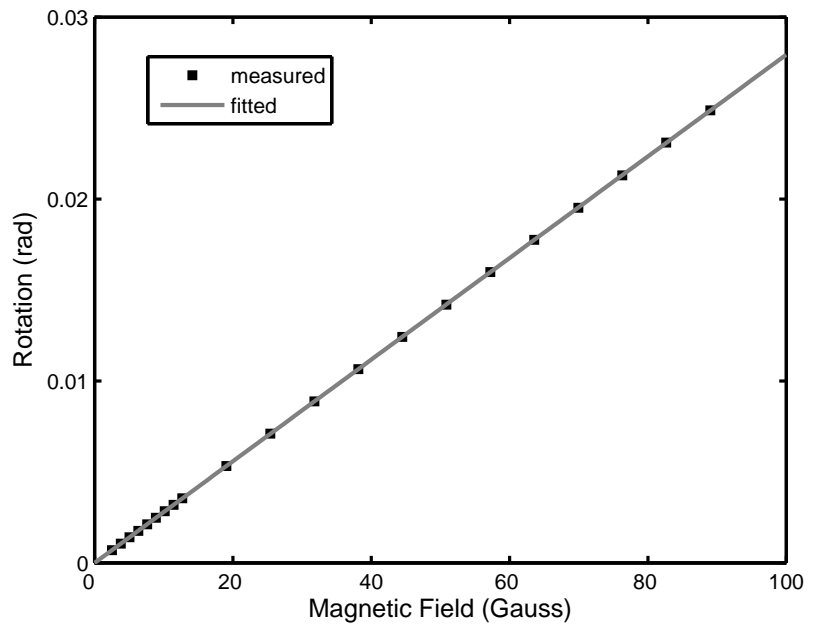


Figure 3.6: Faraday rotation measured from a 2 cm long rod of TGG at a wavelength of 633 nm by varying magnetic field flux densities and a fit to linear line.

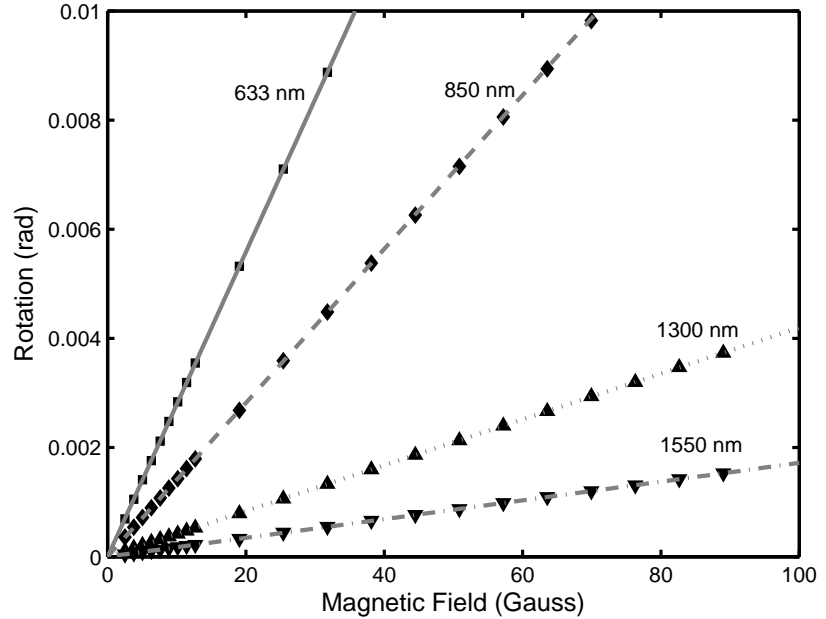


Figure 3.7: Faraday rotation measured for a 2cm-long rod of TGG at different wavelengths

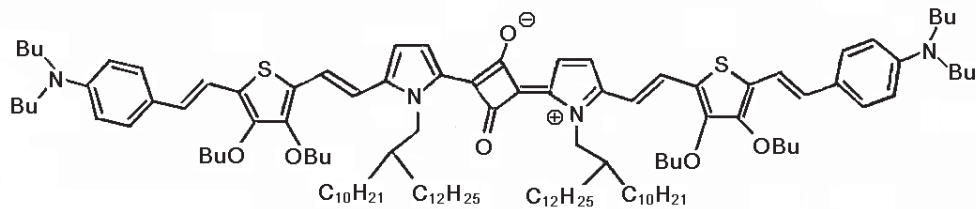


Figure 3.8: Chemical structure of SJZ-87A

vided by Prof. Seth Marder's group at Georgia Tech. All three of them were drop-dispensed and sandwiched by two glass substrates with a spacer. Figure 3.9 shows the UV-Vis-IR transmission spectra of the samples measured with a Cary 5000 spectrophotometer.

We measured the Verdet constant of SJZ-87A at wavelengths of 1300 nm and 1550 nm, and the Verdet constants of TK1V1292A320-A and TK1V1292A320-N at 850 nm. Note that the substrate has a small but finite Verdet constant that must be isolated. Hence, by measuring an angle of rotation from the substrate only, the net rotation from the organic samples were determined. The measured Verdet constant of the substrate was 2.9, 1.3, and 0.9 rad/T · m at 850 nm, 1300 nm, and 1550 nm, respectively. The values of V for SJZ-87A were 10.4 and 4.2 rad/T · m at 1300 nm and 1550 nm, respectively. For TK1V1292A320-A and TK1V1292A320-N, the values were -4.7 and -4.2 rad/T · m at 850 nm, respectively.

The measured Verdet constants of these organic samples are about a half or less than that of TGG, but new chemical structures based on polythiopene are under development. To date, constructing integrated-optic isolators or circulators

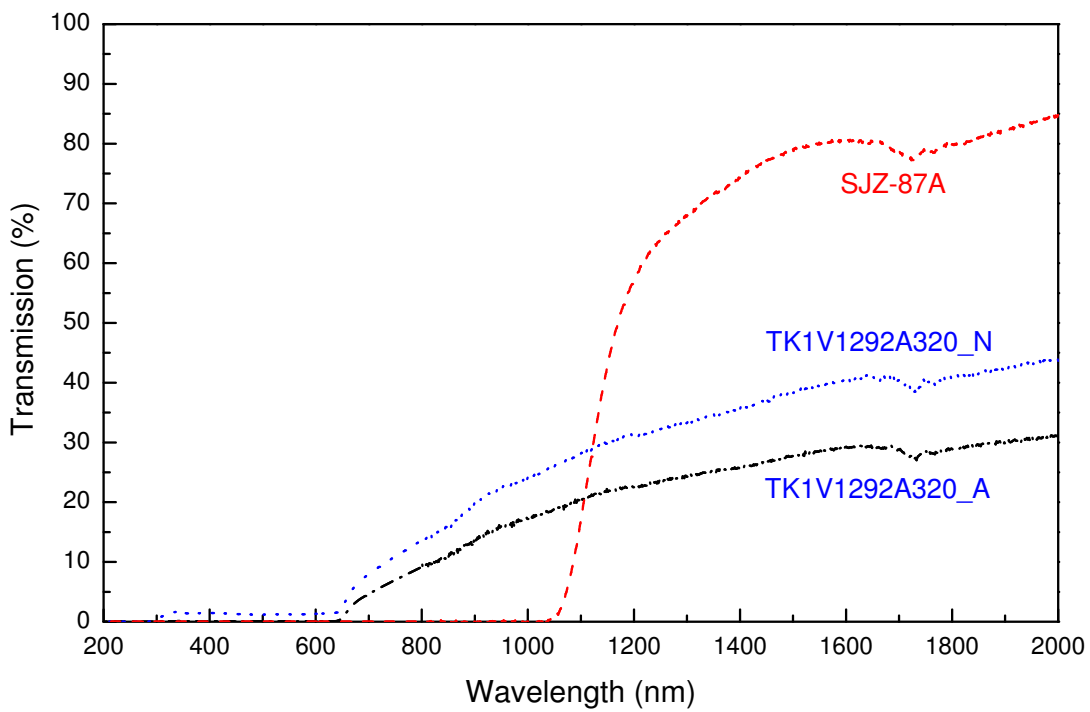


Figure 3.9: UV-Vis-IR transmission spectra measured with a Cary 5000 spectrophotometer for organic magneto-optic samples provided by Georgia Tech.

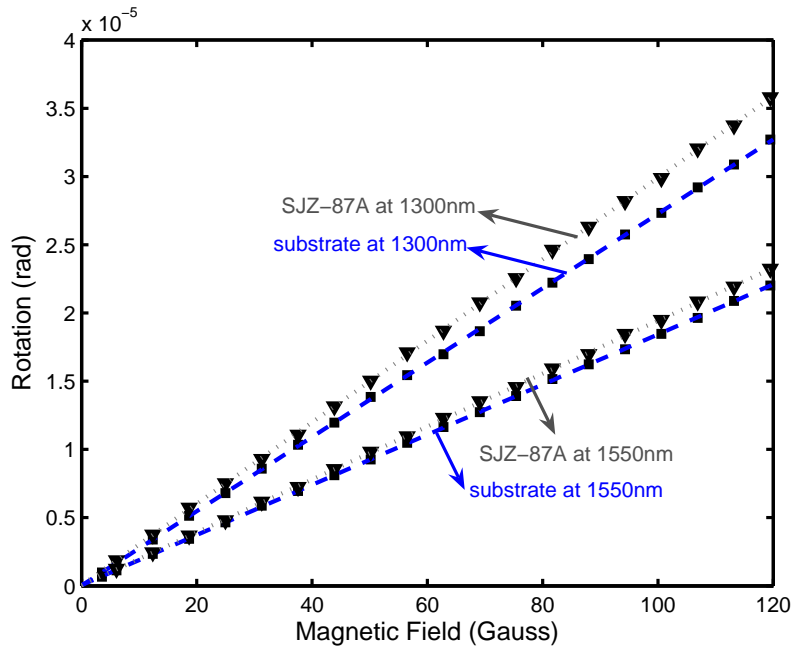


Figure 3.10: Faraday rotation measured for the substrates only and for the sample labelled SJZ-87A at wavelengths of 1300 nm and 1550 nm.

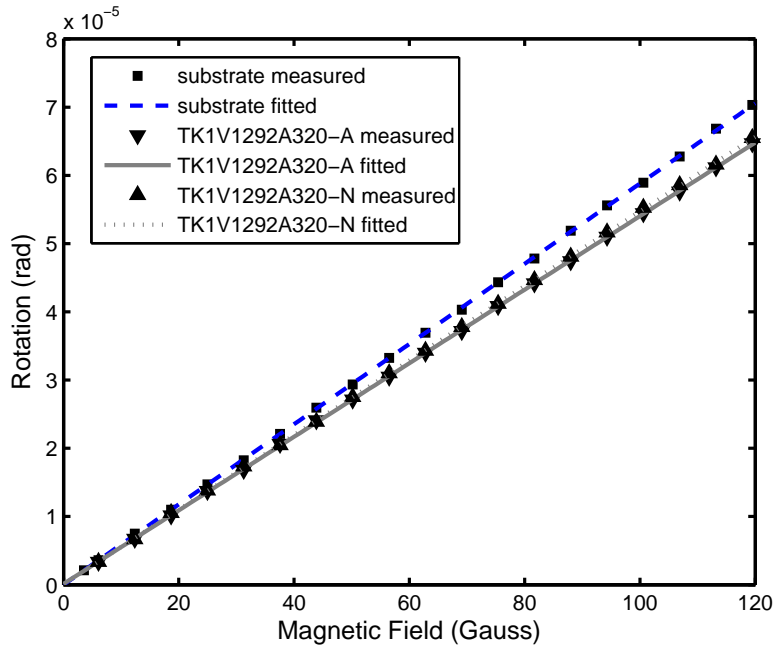


Figure 3.11: Faraday rotation measured for the substrates only and for the samples labelled TK1V1292A320-A and TK1V1292A320-N at a wavelength of 850 nm.

from crystalline magneto-optic materials have been facing challenges. However, organic materials can be potentially very useful because they can be fabricated into waveguide type devices much easier than crystals or glass materials from simple fabrication steps of spin-casting and photolithography.

3.4 Summary

In this chapter, we examined organic magneto-optic materials, which can be viable alternatives to the chiral materials. In addition to polarization rotator, they also can potentially be used for integrated-optic isolators or circulators using their non-reciprocal polarization rotation. The Faraday effect from magneto-optic material is another class of optical activity, and it is characterized by Verdet constant. Measuring the Verdet constants of thin ($10\text{--}100\,\mu\text{m}$) organic samples in a moderate magnetic field (< 100 Gauss) can be very challenging. For this reason, we discussed *balanced homodyne detection* technique that provides a highly sensitive technique to measure an angle of polarization rotation as small as 0.5×10^{-6} rad. We validated this experiment by measuring the Verdet constant of a 2 cm long rod of TGG and confirming the published value. TGG is one of the most widely used material for a free space optical isolator and is believed to have the highest Verdet constant until orders of magnitude higher Verdet constant was observed in organic materials. We demonstrated the Verdet constants of 10.4 and $4.2\,\text{rad}/\text{T}\cdot\text{m}$ at 1300 nm and 1550 nm, respectively, from an organic sample provided by Georgia Tech, which is comparable to that of terbium gallium garnet. This unique observation can lead to

a new opportunity to build integrated-optic isolators or circulators from a simple fabrication methodology including spin-casting and photolithography. However, in order to build practical devices, much work needs to be done to develop materials with even larger Verdet constant and detailed theory on the eigenmode properties in magneto-optic waveguides.

CHAPTER 4

OPTICAL WAVEGUIDE AND MICRORING RESONATOR FROM PFCB

4.1 Perfluorocyclobutyl (PFCB) copolymer

Among the many different kinds of organic polymer materials for passive photonic waveguides, fluorinated polymers are of particular interest due to their significantly low absorption loss at visible and infrared wavelengths. There are several commercially available fluoropolymers including TeflonTM AF (tetrafluoroethylene and perfluorovinyl ether copolymer, DuPont) [38], PolyguideTM (fluoroacrylate, DuPont) [39], UltradelTM (fluorinated polyimide, Amoco) [40], PyralinTM (fluorinated polyimide, HD Microsystems), CytopTM (perfluorovinyl ether copolymer, Asahi Glass) [41], and TOPSTM(perfluorocyclobutyl, originally from DOW and new PFCB-containing polymers under development at Tetramer Technologies, L.L.C) [42]. However, these fluorinated polymers, in general, suffer from limitations on processability including poor adhesion to other layers, limited solubility, poor mechanical properties such as a large coefficient of thermal expansion (CTE) and a large elongation constant that makes cleaving difficult.

The chemistry of PFCB polymers developed at Tetramer Technologies are

based on the thermal cyclopolymerization of bi- or tri-functional aryl trifluorovinyl ether monomers as shown in Fig. 4.1. These PFCB polymers and their copolymers are well suited for applications in the areas of integrated optics and photonics due to the tailorability of their refractive indices (1.443–1.527 at 1550 nm) as well as their high thermal, mechanical and optical stability, and high solubility (50 – 90 wt.%). In general, a material’s intrinsic contribution to the propagation loss at telecommunication wavelengths is dominated by multi-phonon absorption due to the excitation of molecular vibrations and Rayleigh scattering due to the local density or composition fluctuations in the material. The absorption of light from excited molecular vibrations in organic materials can be reduced significantly by replacing C-H bonds with C-F bonds. A larger reduced mass of C-F bond results in a lower vibrational resonant frequency (a longer resonant wavelength). Therefore, the strength of absorption decreases by approximately an order of magnitude between successive vibrational harmonics (sometimes referred to as vibrational overtones) [43, 44]. As a consequence, the absorption loss in the fluorinated polymer is greatly reduced at all the key communication wavelengths.

4.2 Low loss optical waveguide from PFCB copolymer

A low loss optical waveguide is one the most important building blocks in integrated-optic communication systems because most passive and active devices consist of simple straight and curved waveguide segments. In this section, we describe a design, fabrication and measurement of optical propagation loss of the PFCB-based

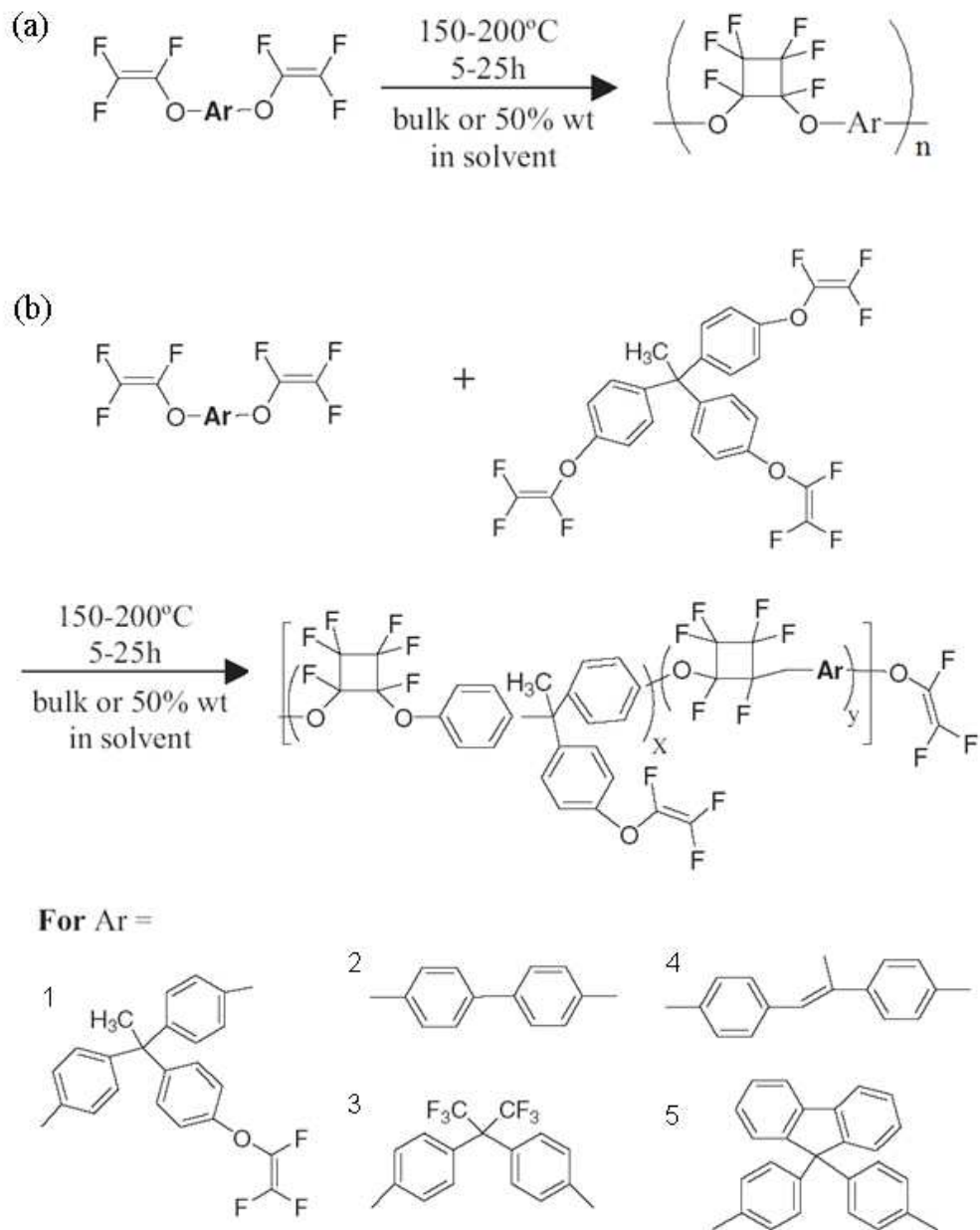


Figure 4.1: Thermal (a)polymerization and (b)copolymerization to PFCB-based polymer from trifluorovinylaryl ether monomers. Five selective aryl substituent are shown at the bottom. Courtesy of Tetramer Technologies, L.L.C.

polymer single mode waveguides.

4.2.1 Eigenmodes in dielectric waveguides

A single mode waveguide, which supports only one eigenmode for each polarization state, is preferable in most photonic communication components. To briefly discuss the design of a single-mode waveguide, let's first consider the time-independent wave equation for the electric fields,

$$\nabla^2 \bar{\mathbf{E}} + \nabla \left(\frac{1}{n^2} \nabla(n^2) \cdot \bar{\mathbf{E}} \right) + k_0^2 n^2 \bar{\mathbf{E}} = 0 \quad (4.1)$$

which can be obtained from the Maxwell's equations 2.3, 2.4, 2.11, 2.12 with the constitutive relations for non-magnetic dielectric materials given as

$$\bar{\mathbf{D}} = \epsilon \bar{\mathbf{E}}, \quad (4.2)$$

$$\bar{\mathbf{B}} = \mu \bar{\mathbf{H}}, \quad (4.3)$$

$$\epsilon(x, y) = \epsilon_0 n^2(x, y), \quad (4.4)$$

$$\mu(x, y) = \mu_0. \quad (4.5)$$

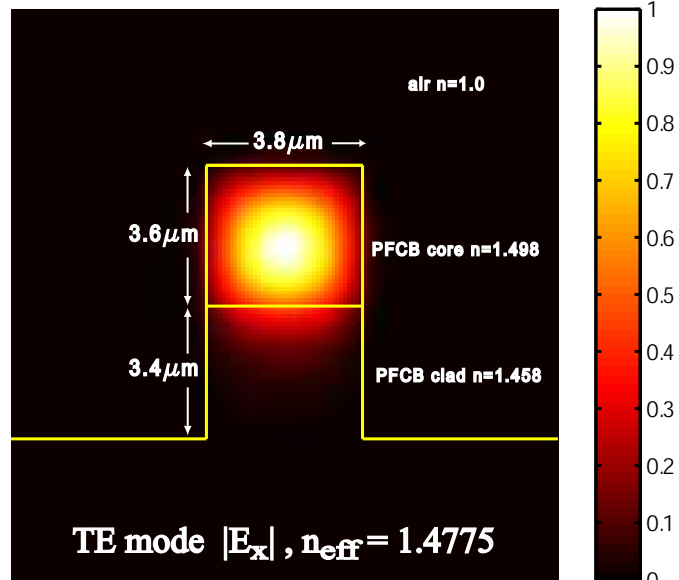
Because we consider the waveguide structures to have a piecewise constant refractive index profile from a homogeneous dielectric medium rather than a graded index profile and we assume an electric field with a longitudinal z-dependence of $e^{-j\beta z}$, the eigenvalue equation for the transverse components of the electric fields can be written as

$$\nabla_t^2 \mathbf{e}_t + (k_0^2 n^2 - \beta^2) \mathbf{e}_t = 0. \quad (4.6)$$

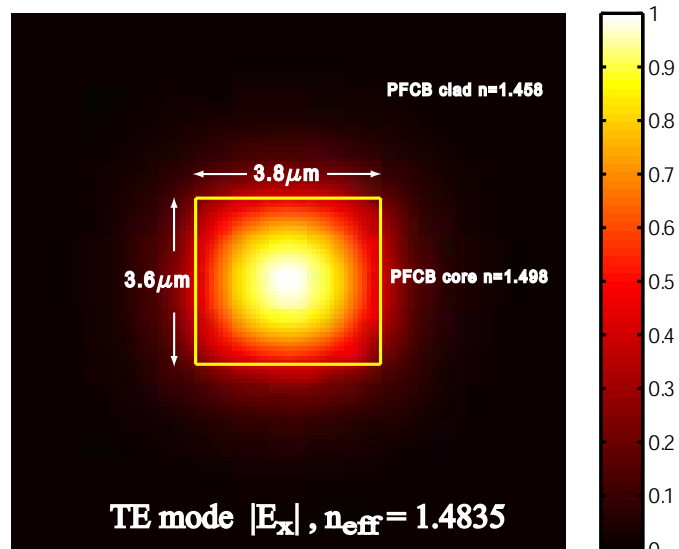
Note that once the transverse components of the electric field, e_x and e_y , are obtained by solving the above equation with proper boundary conditions, all the other field components can be computed using Maxwell's equations.

Except for a few special cases that can be solved analytically, such as a one-dimensional planar waveguide extending infinitely in one direction or an optical fiber with cylindrical symmetry, most dielectric optical waveguides require numerical computation to solve the waveguide eigenvalue equations, such as the finite element method (FEM) [45,46], the finite difference method (FDM) [47,48], and the beam propagation method (BPM) [49–51]. Although there are several commercial software packages available including Apollo Photonic Solutions Suite (APSSTM) from Apollo Photonics, OptiBPMTM from Optiwave Corp., and BeamPROPTM from RSoft Design Group, Inc., we performed a full-vectorial waveguide modal analysis using a finite difference mode solver written in MATLAB code [52].

Two different types of guiding structures, the pedestal structure and the buried channel structure, were considered with a PFCB core ($n=1.498$, with aryl substituent 2 in Fig. 4.1) and a PFCB cladding ($n=1.458$, with aryl substituent 3 in Fig. 4.1), both from Tetramer Technologies. Figure 4.2 shows the calculated mode profile of the transverse electric field component $|e_x|$ and effective index $n_{\text{eff}} (= \beta/k_0)$ for the fundamental TE mode for both structures. For the pedestal waveguide, the dimensions of the core are $3.8 \mu\text{m} \times 3.6 \mu\text{m}$ and the waveguide is etched down $3.4 \mu\text{m}$ into the cladding layer. The calculated n_{eff} is 1.47571 and 1.47647 for the TE and TM, respectively. For the buried channel waveguide, the



(a)



(b)

Figure 4.2: Mode profile of the transverse electric field component $|e_x|$ for the fundamental TE mode for two different types of straight waveguides, pedestal and buried channel, using a full-vectorial finite difference mode solver. The orthogonal field component $|e_y|$ is orders of magnitude smaller than $|e_x|$, and hence it is omitted. (a) Pedestal structure, (b) Buried channel structure.

dimensions of the core are $3.8 \mu\text{m} \times 3.6 \mu\text{m}$ and n_{eff} is 1.48300 and 1.48297 for TE and TM, respectively. Note that, in the buried channel waveguide, TE and TM modes are nearly degenerate ($n_{\text{eff}}^{\text{TE}} \approx n_{\text{eff}}^{\text{TM}}$) because it has a geometric configuration close to that of a square and a symmetric index profile.

It is worth pointing out here that although the eigenmodes of an optical dielectric waveguide are usually not pure TE or TM¹, except in those two special cases of a one-dimensional slab waveguide and an optical fiber that we mentioned above, they are typically referred to as TE or TM modes since one of the two transverse field components is orders of magnitude larger than the other. For example, in Fig. 4.2 the orthogonal field component $|e_y|$ is orders of magnitude ($\sim 10^4$) smaller than $|e_x|$ in both cases and therefore it is not shown.

4.2.2 Fabrication of PFCB waveguides

This section describes the outline of the fabrication process of waveguides from PFCB. Although the fabrication technique used here is not much different from the ones used to build other integrated-optic waveguide devices because we adopted an already existing conventional photolithography from the semiconductor IC industry, there are a few unique challenges to fabricating the waveguides from PFCB: poor adhesion, a mask cracking problem, and deep etching required.

Figure 4.3 depicts an outline of the process steps to fabricate the PFCB wave-

¹In some articles or books, they are often referred to as HE/EH or E^x/E^y indicating they are Hybrid modes. Note that the transverse electric field components $|e_x|$ and $|e_y|$ in Eq. 4.6 can not be decoupled. Therefore, strictly speaking, TE/TM are not appropriate any more since the solutions of eigenmode equations have both non-zero $|e_z|$ and $|h_z|$ [14, 53]

uides. We used Si substrates for a mechanical platform for the waveguides. In general, fluorinated polymers have poor adhesion to other layers, which is a well-known problem [54,55]. In order to improve the adhesion to the Si substrate, we deposited a 100 nm thick SiO₂ layer from a Trion PECVD, after which we spin-casted bisbenzocyclobutene (BCB, CycloteneTM 3022-35 purchased from Dow Chemical) followed by soft curing at 210 °C for 40 min as suggested by the vendor [56]. This 1 μm thick layer of BCB is believed to not only improve the adhesion strength to SiO₂/Si, but also relax the stress from the CTE mismatch between the PFCB and the substrate. These two layers were omitted in Fig. 4.3 for clarity.

Next, solutions of PFCB cladding in mesitylene were spin-coated at a spin speed to achieve a 7 μm thick layer and cured at 220 ° in the vacuum oven with N₂ environment. It is very difficult to put the PFCB core layer on top of the PFCB cladding once the cladding layer is fully cured. This problem can be solved with a partial curing of the cladding layer. However, when it is not cured enough, the cladding is attacked by the mesitylene solvent contained in the core solution. Therefore, adjusting the degree of partial curing to provide both good adhesion and resistance to the solvent at the same time is very critical and this can be found from trial-and-error. We have also found that dispensing mesitylene followed by spin-drying and keeping the sample in a N₂ environment for about one hour before casting the PFCB core layer can provide an improved adhesion. After about the 3.6 μm PFCB core layer was prepared, the sample was ready for etching the waveguide.

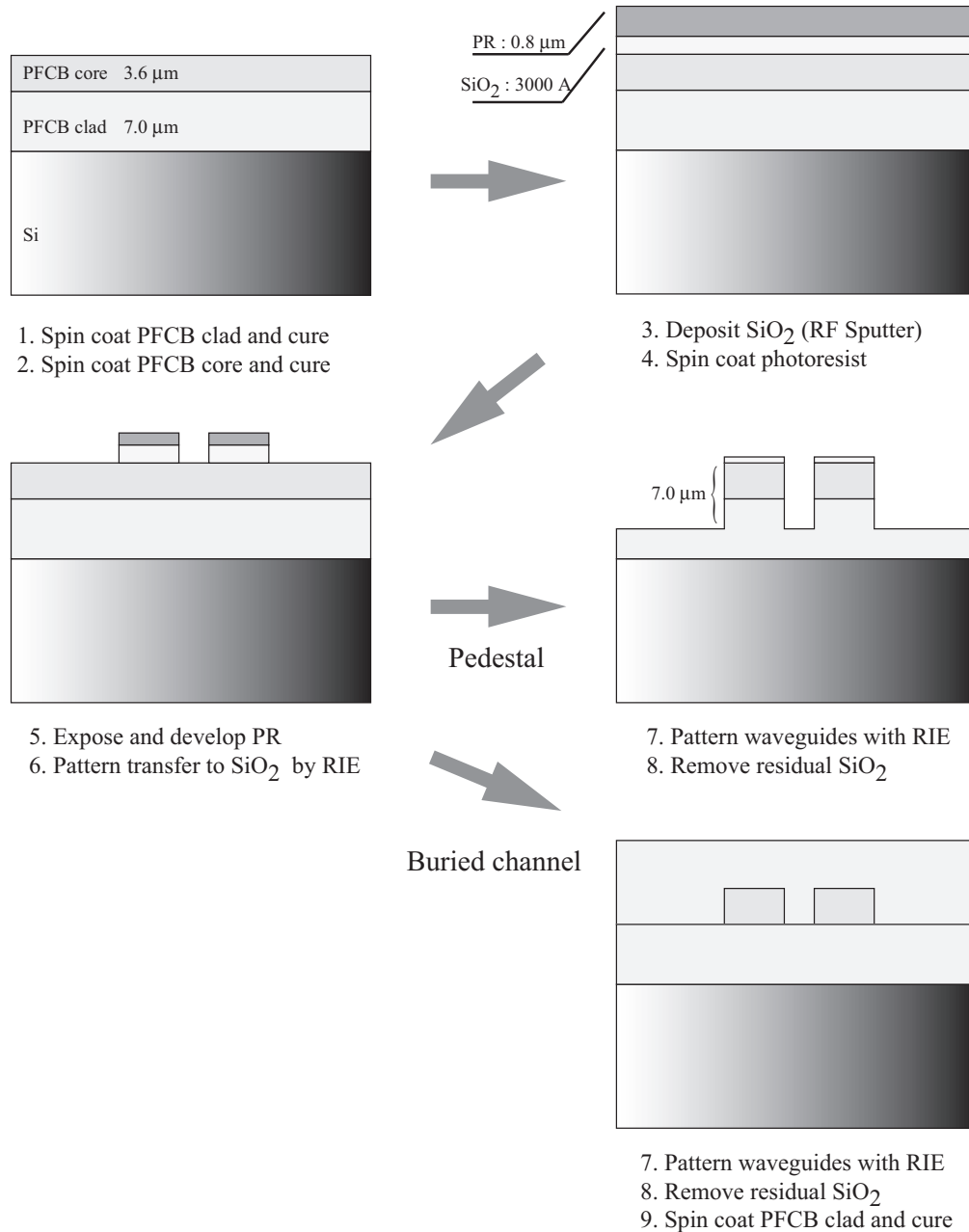


Figure 4.3: Outline of process steps to fabricate the PFCB waveguides. SiO₂ and BCB layers inserted for adhesion are not included for clarity.

Because a deep etch ($\sim 7\mu\text{m}$ in the case of the pedestal structure) is required for a waveguide structure, a hard mask was used rather than a photoresist soft mask. For the etching mask, about a 300 nm thick SiO_2 layer was deposited on PFCB dual layers using an RF sputter deposition in an argon plasma. We used an AJA International magnetron sputter with a chamber pressure of 3 mT and an RF power of 250 W for 70 min, resulting in a deposition rate about $43\text{\AA}/\text{min}$. Initially, a layer of SiO_2 from PECVD was tried for the sacrificial hard etching mask, but it caused a severe mask cracking problem. It is believed that the SiO_2 from a magnetron sputter has a lower packing density than the SiO_2 from a PECVD, hence it is less susceptible to cracking, which is likely due to the CTE mismatch. We also found an alternative solution of using a metal bilayer of Ni/Au that can be patterned by deposition and lift-off. The Ni/Au etching mask can be particularly useful for an etching mask in the case that the SiO_2 :cladding selectivity is poor, for example, when a thermal SiO_2 layer is used for a lower cladding.

For waveguide patterning, an 800 nm thick layer of OIR 906-10 photoresist was exposed with a $5\times$ GCA i-line projection aligner and developed in OPD 4262 for 60 seconds. The optimized exposure condition was found to be an expose duration of 0.13 s and a focus offset of 0 through a focus/exposure test. Next, the waveguide pattern was transferred to the sputtered SiO_2 by reactive ion etching using a Plasmatherm RIE system in a CHF_3/O_2 plasma with a flow rate of 18 sccm of CHF_3 and 2 sccm of O_2 , a chamber pressure of 40 mT and an RF power of 200 W, which resulted in an etch rate of 40-45 nm/min. It should be noted that a slight

over etch into the core layer is required to ensure that the SiO₂ has completely cleared. After patterning the SiO₂ mask, a waveguide was etched by RIE in an Ar/O₂ plasma with a flow rate of 20 sccm of Ar and 10 sccm of O₂, a chamber pressure of 20 mT, and an RF power of 250 W, which resulted in a PFCB etch rate of 150-160 nm/min. The PFCB:SiO₂ selectivity greater than 25:1. If desired, any residual photoresist on top of SiO₂ could be removed easily in acetone, but it is not required. After the PFCB etching was completed, the remaining SiO₂ was removed in a buffered oxide etch (BOE). For the buried channel waveguide structure, the PFCB clad layer was spun and cured to serve as a top cladding layer after patterning the core. For the final step, devices were cleaved to form smooth end facets allowing end-fire coupling for measurements.

Figure 4.4 shows the scanning electron micrograph of the PFCB pedestal waveguide. As shown in the figure, the PFCB core and clad layer are distinguishable by exhibiting composition-dependent side wall roughness.

4.2.3 Loss measurement of straight waveguides

The loss measurement of a straight waveguide is basic but critical because one often wants to isolate the propagation loss from total waveguide insertion loss. This can be very helpful in designing more advanced integrated-optic devices. From several available methods for waveguide-loss measurement, we chose the cut-back method [57], which is the most simple and straightforward technique. A drawback of this method is that it is a destructive measurement method requiring successive

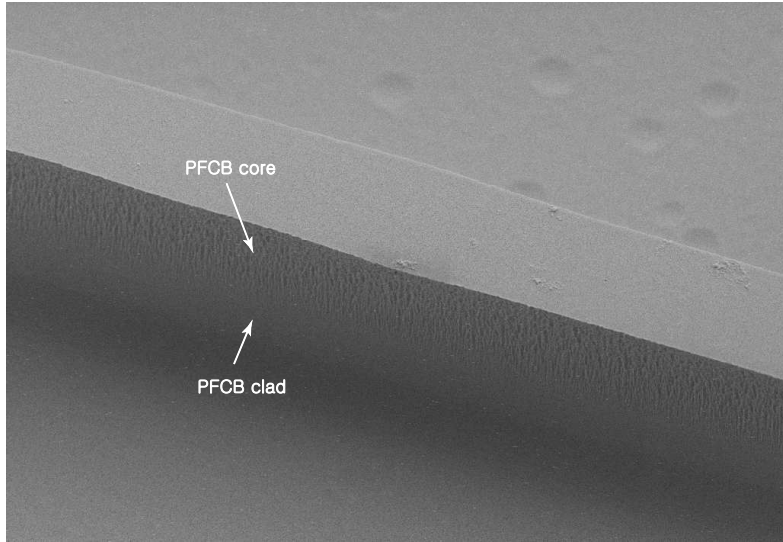


Figure 4.4: Scanning electron micrograph of the PFCB pedestal waveguide.

cleaving [58]. Another popular way to measure the loss is using the properties of Fabry-Perot resonance, because the two end facets of the waveguide form a resonant cavity [59, 60]. However, for polymer waveguides, the reflectivity at the air/waveguide interface is rather small and the cleaved surfaces are not quite as perfect as those of semiconductor waveguides, so the Fabry-Perot method is less reliable.

Figure 4.5 shows the measured total insertion loss at a wavelength of 1550 nm for the TE mode at four different waveguide lengths achieved by sequential cleaving. A single mode fiber with a conical tip (with a focal length of $\sim 8 \mu\text{m}$) was used to allow efficient end-fire coupling between the optical fiber and the waveguide. Once the total transmission loss was measured, the coupling loss and the propagation loss can be separated using a linear regression – the coupling loss is

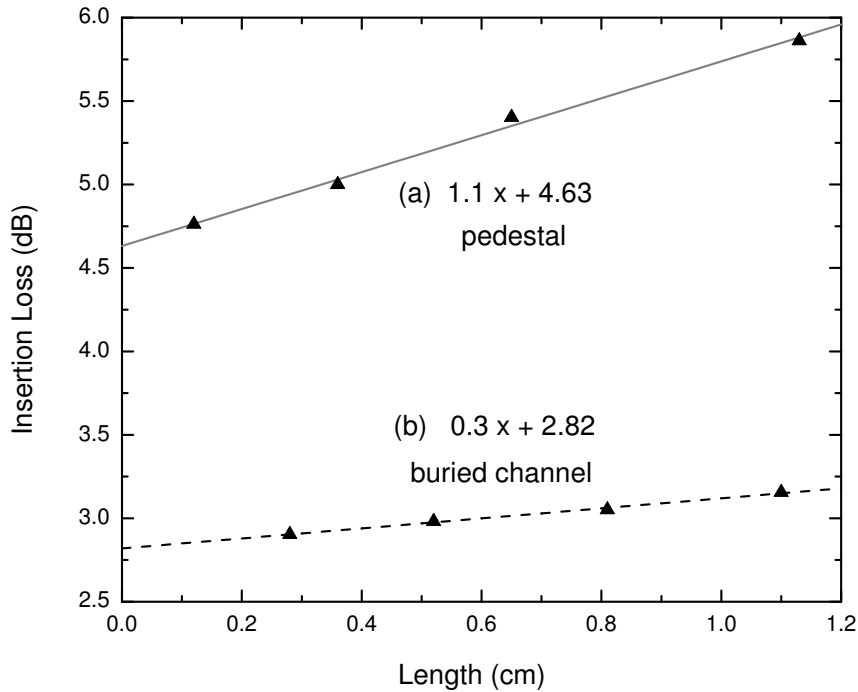


Figure 4.5: Loss measurement of PFCB straight waveguides using cutback method for TE mode. The measured propagation loss is 1.1 dB/cm and 0.3 dB/cm, and coupling loss is 4.63 dB and 2.82 dB for (a) pedestal and (b) buried channel waveguide, respectively.

from the insertion loss at the zero waveguide length, and the propagation loss is from the slope. The measured propagation loss was 1.1 dB/cm and 0.3 dB/cm, and coupling loss was 4.63 dB and 2.82 dB for the pedestal and buried channel waveguides, respectively. The difference in propagation loss between the two waveguides comes mostly from a difference in scattering loss: In general, scattering loss is larger at the waveguide side walls than at the horizontal (upper and lower) interfaces because the presence of surface roughness is dominant at the side walls

from reactive ion etching (RIE) procedures [61, 62]. For the same reason, the side wall roughness exhibits the polarization dependent loss (PDL) – the TE loss is typically slightly higher than the TM loss. Furthermore, the surface-roughness-induced scattering loss is particularly high in the case of tighter confinement of the mode in the core as opposed to the case of weak confinement because of different index contrast [39]. On the other hand, the coupling loss is smaller in the buried channel waveguide because of the difference in mode mismatch between the fiber and the waveguide [63].

4.3 PFCB Microring resonators

Devices based on a microring resonators have been actively investigated by many research groups due to their simple configuration and yet highly interesting multiple functionality. Some applications include phase shifters, optical channel dropping filters (OCDF), optical add-drop (de)multiplexers, switches, photonic logic gates, amplifiers and lasers. There are a number of excellent journal articles and theses describing the comprehensive historical background and fundamental theory on microring and microdisc resonators [64–68]. Therefore, we begin by describing a very succinct summary of the basic theoretical principles of the ring resonator rather than a comprehensive summary, and then we discuss the design considerations and characterization of microring resonators fabricated from PFCB copolymers.

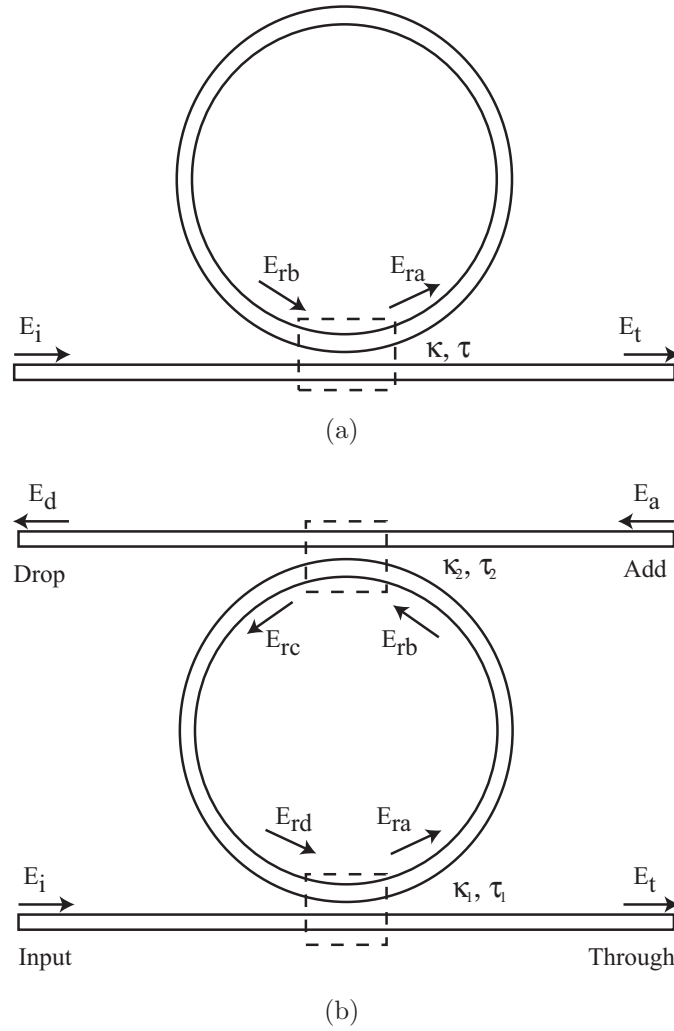


Figure 4.6: Schematic diagram of microring resonators. (a) all-pass and (b) add-drop configuration.

4.3.1 Basic principles

The microring resonator is, by nature, very similar to a Fabry-Perot resonator in many aspects. The most simple configuration of the microring device is such that the ring is coupled to one or two adjacent waveguides through ‘evanescent field coupling’ as shown in Fig. 4.6. The former is often referred to as an “all-pass

filter” and the latter is commonly called an “add-drop filter”.

By adopting the scattering matrix formulism based on energy conservation and time-reversal symmetry [69], the relationships between the optical electric fields for the add-drop filter, shown in Fig. 4.6, can be written as

$$\begin{bmatrix} E_a \\ E_t \end{bmatrix} = \begin{bmatrix} \tau_1 & -j\kappa_1 \\ -j\kappa_1 & \tau_1 \end{bmatrix} \begin{bmatrix} E_{rd} \\ E_i \end{bmatrix}, \quad (4.7)$$

$$\begin{bmatrix} E_d \\ E_{rc} \end{bmatrix} = \begin{bmatrix} \tau_2 & -j\kappa_2 \\ -j\kappa_2 & \tau_2 \end{bmatrix} \begin{bmatrix} E_{rd} \\ E_i \end{bmatrix}. \quad (4.8)$$

We can also write equations describing the circulation condition along the ring,

$$E_{rb} = E_{ra} \cdot \sqrt{A} \cdot e^{j\phi/2}, \quad (4.9)$$

$$E_{rd} = E_{rc} \cdot \sqrt{A} \cdot e^{j\phi/2}, \quad (4.10)$$

where $A = \exp(\alpha_R L/2)$ represents the field loss (or gain) after one round-trip, $\phi = k_0 n_{\text{eff}} L$ is the round-trip phase change, α_R is the power loss coefficient in the ring, n_{eff} is the effective index of the waveguide, $L = 2\pi R$ is the circumference of the ring, $\kappa_{(1,2)}$ are the field coupling coefficients between the bus and the ring, and $\tau_{(1,2)}$ are the field transmission coefficients. We also assume a lossless coupling, in which case $\tau_{(1,2)} = \sqrt{1 - \kappa_{(1,2)}^2}$.

Therefore, from Eqs. 4.7–4.10, the optical fields at drop port E_d and through

port E_t can be expressed as,

$$E_t = \frac{\tau_1 - \tau_2 A e^{j\phi}}{1 - \tau_1 \tau_2 A e^{j\phi}} E_i + \frac{-\kappa_1 \kappa_2 \sqrt{A} e^{j\phi/2}}{1 - \tau_1 \tau_2 A e^{j\phi}} E_a, \quad (4.11)$$

$$E_d = \frac{-\kappa_1 \kappa_2 \sqrt{A} e^{j\phi/2}}{1 - \tau_1 \tau_2 A e^{j\phi}} E_i + \frac{\tau_2 - \tau_1 A e^{j\phi}}{1 - \tau_1 \tau_2 A e^{j\phi}} E_a. \quad (4.12)$$

When there is no input signal at the add port, i.e. $E_a = 0$, Eqs. 4.11 and are reduced to

$$\frac{E_t}{E_i} = \frac{\tau_1 - \tau_2 A e^{j\phi}}{1 - \tau_1 \tau_2 A e^{j\phi}}, \quad (4.13)$$

$$\frac{E_d}{E_i} = \frac{-\kappa_1 \kappa_2 \sqrt{A} e^{j\phi/2}}{1 - \tau_1 \tau_2 A e^{j\phi}}. \quad (4.14)$$

The optical field at the through port E_t for the all-pass configuration can be obtained by putting $\tau_1 = \tau$ and $\kappa_1 = \kappa$, and letting $\kappa_2 = 0$ in Eq. 4.13 because there is no second waveguide adjacent to the ring. Then, for the all-pass configuration, we have

$$\frac{E_t}{E_i} = \frac{\tau - A e^{j\phi}}{1 - \tau A e^{j\phi}} \quad (4.15)$$

$$= \frac{A - \tau e^{j\phi}}{1 - \tau A e^{j\phi}} \cdot e^{j(\pi+\phi)}. \quad (4.16)$$

The phase of E_t can be obtained from Eq. 4.16 and can be written as,

$$\Phi = \frac{\tau - A e^{j\phi}}{1 - \tau A e^{j\phi}}. \quad (4.17)$$

For the all-pass configuration, when the ring resonator is lossless, i.e. $A = 1$, (but, in practice, this has to be the negligible loss case, $A \approx 1$) the output power is unity (100% transmission) at all wavelengths regardless of the coupling coefficient κ . On

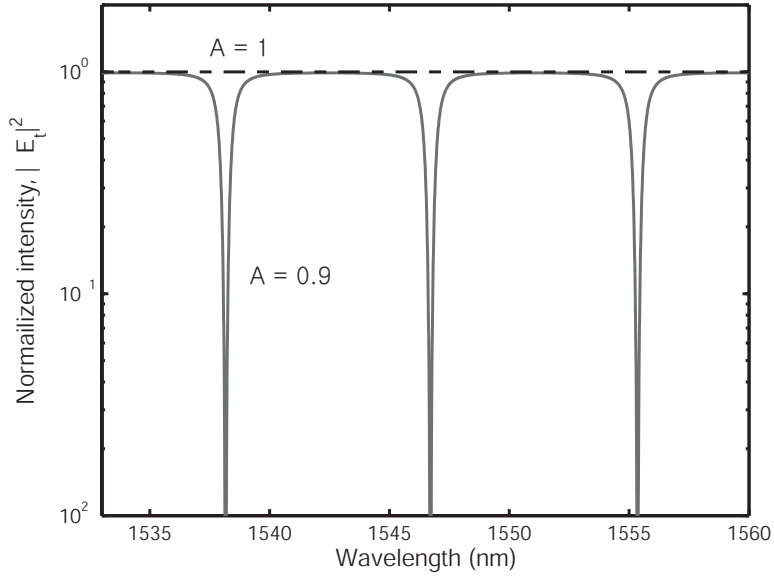


Figure 4.7: Calculation of a typical spectral response of all-pass filter with $n_{\text{eff}} = 1.477$, $R = 30 \mu\text{m}$, and $\tau = 0.9$ for when $A = 1$ and $A = 0.9$ representing the lossless case and the round-trip power loss of 19%, respectively.

the other hand, when the ring has a finite amount of loss that satisfies “critical coupling”, in which the round trip field loss of the ring equals the field coupled into the ring from the bus waveguide, i.e. $A = \tau$, the output power has high extinction at the resonant wavelengths. This could be used as an optical channel-drop filter (OCDF), also referred to as a notch filter. Figure 4.7 shows the calculation of a typical spectral response of an all-pass filter with $n_{\text{eff}} = 1.477$, $R = 30 \mu\text{m}$, and $\tau = 0.9$ when $A = 1$ and $A = 0.9$ representing the lossless case and the round-trip power loss of 19%, respectively.

Although the all-pass configuration with a negligible loss is not useful as a

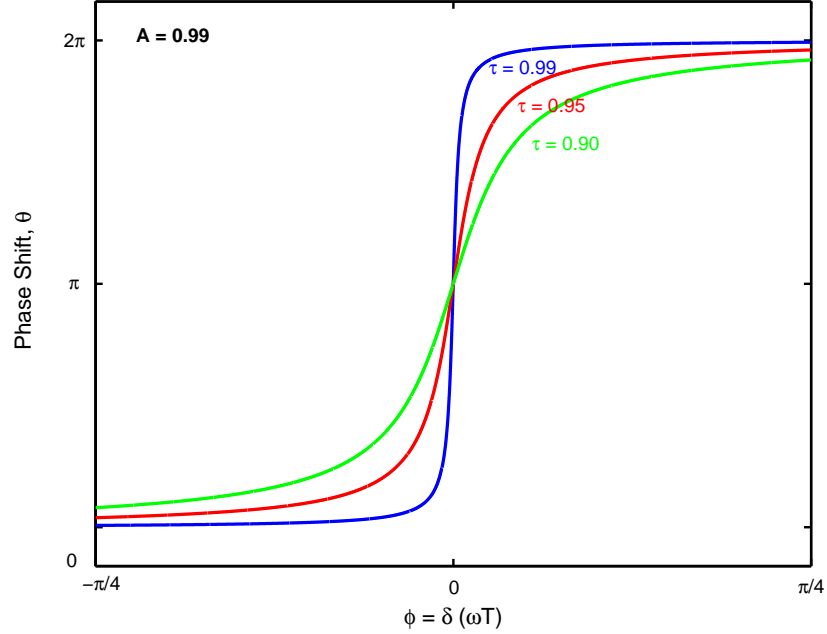


Figure 4.8: Calculated phase response near a resonance in all-pass configuration for three different τ 's when the loss is very small, $A = 0.99$.

channel drop filter, its interesting phase response near the resonant wavelength ($\phi \approx 0$), as shown in Fig. 4.8, makes it possible for use as a π phase shifter. This can be utilized as a notch filter by incorporating it into one arm of a Mach-Zehnder interferometer [66]. The add-drop configuration is mathematically equivalent to a Fabry-Perot interferometer with two input and two output ports. Using the narrow-band amplitude filter response from its high wavelength selectivity, one can drop a particular frequency band from the input port via the drop port and add another band from the add port to the through port. Figure 4.9 shows a typical spectral response of an add-drop filter with $n_{\text{eff}} = 1.477$, $R = 30 \mu\text{m}$, $A = 0.95$, and $\tau_1 = A\tau_2 = 0.9$ satisfying the critical condition. Resonators are

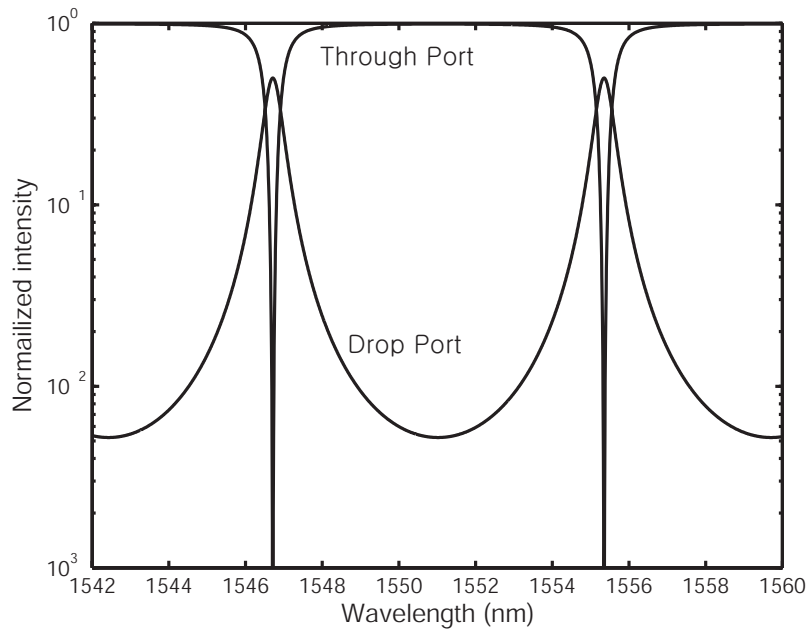


Figure 4.9: Calculation of a typical spectral response of add-drop filter with $n_{\text{eff}} = 1.477$, $R = 30 \mu\text{m}$, $A = 0.95$, and $\tau_1 = A\tau_2 = 0.9$ satisfying the critical condition.

typically characterized by their free spectral range $\Delta\nu_{\text{FSR}}$ (or $\Delta\lambda_{\text{FSR}}$), resonance width $\Delta\nu_{\text{FWHM}}$ (or $\Delta\lambda_{\text{FWHM}}$, the full width at half maximum), quality factor Q , and finesse \mathcal{F} . The free spectral range is the separation between two successive resonances expressed as,

$$\Delta\nu_{\text{FSR}} = \frac{c}{L n_{\text{eff}}} = \frac{1}{T} \quad \text{in frequency,} \quad (4.18)$$

$$\Delta\lambda_{\text{FSR}} = \frac{\lambda_0^2}{L n_{\text{eff}}} \quad \text{in wavelength,} \quad (4.19)$$

and the finesse \mathcal{F} is defined as

$$\mathcal{F} = \frac{\Delta\nu_{\text{FSR}}}{\Delta\nu_{\text{FWHM}}} \quad (4.20)$$

The quality factor Q , describing the rate at which the resonator dissipates its stored energy and the sharpness of a resonance, is defined as the resonance frequency divided by the bandwidth, $Q = \nu_0/\Delta\nu_{\text{FWHM}}$, and is related to the finesse by $Q = Ln_{\text{eff}}\mathcal{F}/\lambda$.

4.3.2 Design considerations

Mode analysis

In section 4.2.1, we discussed the eigenmodes of the dielectric waveguides and numerically computed the eigenvalue equation to find the eigenmodes for a given waveguide geometry. The numerical mode profile that we obtained can also be used to compute the scattering loss at the waveguide boundary or the coupling efficiency between two adjacent waveguides. To construct the microring resonator devices, the pedestal waveguide structure was adopted simply because it allows the most tightly confined guiding geometry.

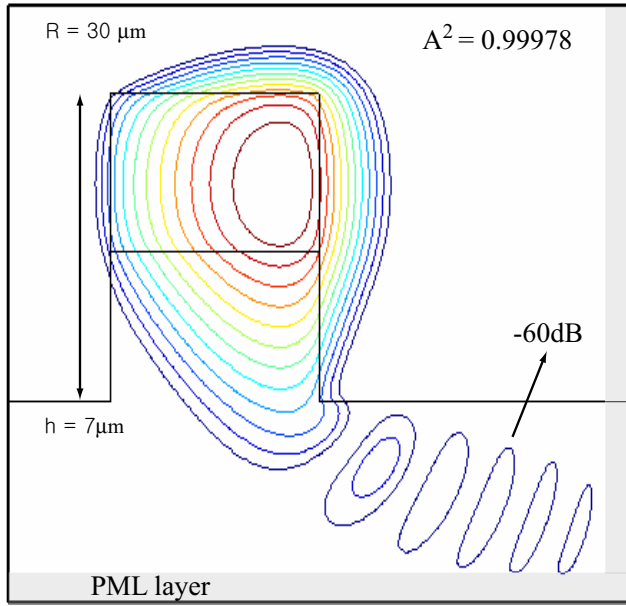
Bending Loss

The most commonly used practical figure of merit for a ring resonator is the quality factor or finesse, which is directly related to the radius of the ring, the propagation loss in the ring, and the coupling efficiency between the ring and waveguide. Obtaining loss as low as possible is essential because the loss directly dictates the resonance bandwidth (FWHM), hence Q and \mathcal{F} of the ring resonator. Two main contributions to loss in the ring are bending loss and scattering loss. For a given index contrast of the waveguide, one can simply increase size of the ring and in-

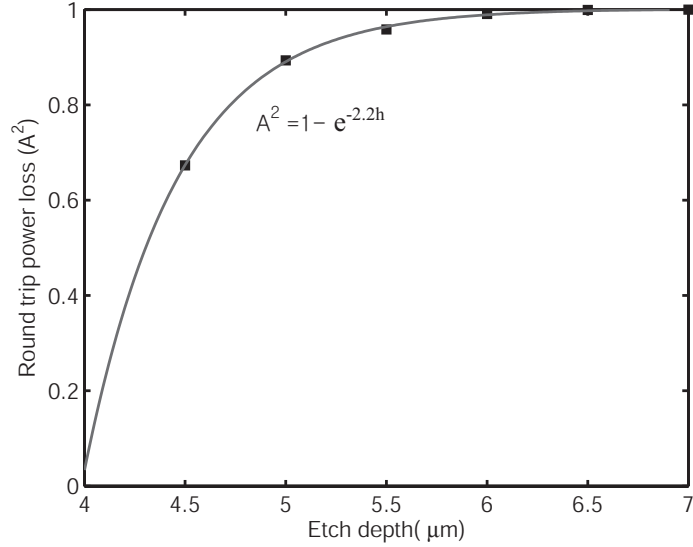
crease etching depth of the pedestal structure in order to minimize the bending loss.

For the PFCB microring devices, the waveguide dimensions in Fig. 4.2(b) and a radius of curvature R in the range of 25–40 μm are chosen from detailed numerical modelling for the bending loss. There is a simple model to calculate bending loss in planar slab waveguides based on Fraunhofer diffraction theory [70]. This model can be very useful especially in the early phase of the design by providing a good starting point for determining a radius of curvature and width of the waveguide. However, for most practical waveguides with a 3D structure confining the lightwave both horizontally and vertically, this is only a good approximation.

We performed a 3D full vectorial FD calculation incorporating a conformal transformation and a complex perfectly matched layer (PML) [71–73]. Figure 4.10(a) shows that a radius R of 30 μm with an etch depth 7 μm is estimated to yield negligible bending loss ($< 10^{-3}$ dB). Figure 4.10(b) shows the etch depth dependence from the calculation of the bending loss with several different etch depths when $R = 30 \mu\text{m}$. The round-trip power loss $A^2 (= \exp(\alpha_R L))$ as a function of etch depth h can be fitted to an exponential curve, i.e. $A^2 = 1 - e^{-2.2h}$. It should be noted that this dependence could almost be predicted from the fact that the field decay constant in the lower cladding layer, $k_0 \sqrt{n_{\text{eff}}^2 - n_s^2}$, is about 1.13 when $n_{\text{eff}} = 1.4775$, and the power decay constant is twice as much.



(a) Bending loss when $R = 30 \mu\text{m}$



(b) Etch depth dependence

Figure 4.10: 3D full vectorial calculation for a bending loss. (a)negligible bending loss $< 10^{-3}$ dB when a radius R of $30 \mu\text{m}$ with a etch depth of $7 \mu\text{m}$, and (b)Etch depth dependence of the bending loss when $R = 30 \mu\text{m}$. The round-trip power loss A^2 as a function of the etch depth h can be fitted to an exponential curve, $A^2 = 1 - e^{-2.2h}$.

Coupling efficiency

One of the most important design parameters for constructing a practical microring resonator device is the coupling efficiency – the amount of power transferred from one waveguide to another when they are in close proximity – between the waveguide and the ring. From this, we can determine the physical size of the gap required for the critical coupling condition.

In a system consisting of two adjacent waveguides, the coupling constant between the two can be numerically computed from the mode profile we obtained before and the coupled-mode theory [52, 74]. A very comprehensive and excellent summary on non-orthogonal coupled-mode theory can be found in [52]. Therefore, in this section, we present only the computation results for the coupling constant μ in the coupled-mode equation,

$$\frac{d}{dz} \begin{bmatrix} a_1(z) \\ a_2(z) \end{bmatrix} = -j \begin{bmatrix} \beta_1 & \mu_{12} \\ \mu_{21} & \beta_2 \end{bmatrix} \begin{bmatrix} a_1(z) \\ a_2(z) \end{bmatrix}, \quad (4.21)$$

where β_1 and β_2 are the propagation constants of waveguide 1 and waveguide 2, respectively.

When the two waveguides are identical to each other, we can calculate the coupling constant in a more direct way by considering the coupled waveguide system as a whole rather than as two separate waveguides. The approximate normal modes of the system can be expressed as the symmetric and antisymmetric

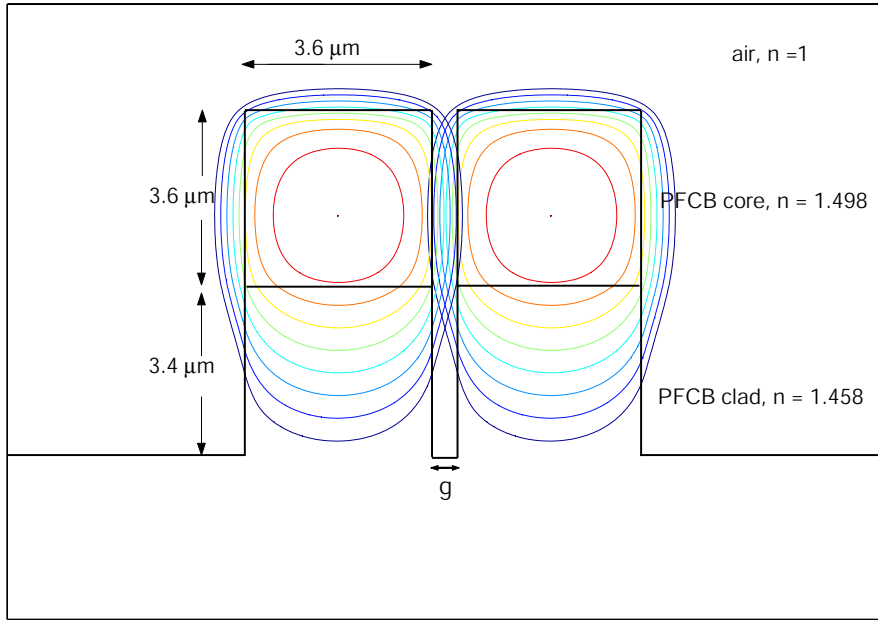


Figure 4.11: Cross-sectional mode profile of two parallel waveguides separated by an edge-to-edge distance g .

combinations of the isolated waveguide modes as

$$\beta_s = \beta + \mu, \quad \mathbf{v}_s = \frac{1}{\sqrt{2}} = \begin{bmatrix} +1 \\ +1 \end{bmatrix}, \quad (4.22)$$

$$\beta_a = \beta - \mu, \quad \mathbf{v}_a = \frac{1}{\sqrt{2}} = \begin{bmatrix} +1 \\ -1 \end{bmatrix}. \quad (4.23)$$

Therefore, the coupling constant μ can be written as

$$\mu = \frac{1}{2}(\beta_s - \beta_a). \quad (4.24)$$

Figure 4.11 shows the mode profile of two parallel PFCB pedestal waveguides separated by an edge-to-edge distance g , which was used to compute the coupling

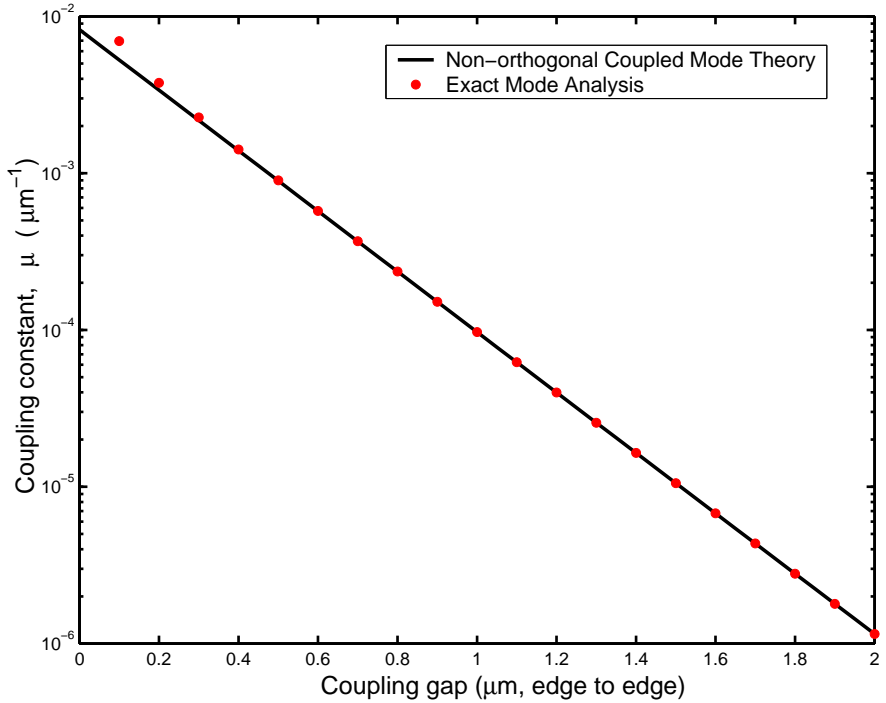


Figure 4.12: Calculation of coupling constant between two PFCB pedestal waveguides as a function of waveguide separation g .

constant. Figure 4.12 shows the calculated coupling constant μ between two PFCB pedestal waveguides as a function of waveguide separation g from both the non-orthogonal coupled theory and the direct mode analysis. Note that the coupling constant μ drops exponentially with increasing separation g , as we expect from the fact that electric field decays exponentially in the cladding region. Also note that the direct modal evaluation agrees very well with the coupled mode theory, especially when $g > 0.3 \mu\text{m}$.

In order to find the field coupling coefficient κ in Eqs. 4.13–4.16, we consider

the transfer matrix, which is the solution of the differential coupled mode equation:

$$\begin{bmatrix} a_1(z) \\ a_2(z) \end{bmatrix} = e^{j\beta_0 z} \begin{bmatrix} \cos \sigma(z) & -\sin \sigma(z) \\ -\sin \sigma(z) & \cos \sigma(z) \end{bmatrix} \begin{bmatrix} a_1(0) \\ a_2(0) \end{bmatrix}, \quad (4.25)$$

with

$$\sigma(z) \equiv \int_0^z \mu(z) dz, \quad (4.26)$$

where $\sigma(z)$ represents the integrated coupling when the two waveguides approach and separate gradually as in the microring resonator. If light is launched into waveguide 1 at $z = 0$, then the relative power in the two waveguides as a function of z is given by,

$$\left| \frac{a_2(z)}{a_1(0)} \right| = \sin \sigma(z), \quad (4.27)$$

$$\left| \frac{a_1(z)}{a_1(0)} \right| = \cos \sigma(z). \quad (4.28)$$

Therefore, the coupling coefficient κ between the ring and the bus waveguide is

$$\kappa = \sin \sigma(z) \quad (4.29)$$

$$\approx \sigma(z) \quad \text{when } \sigma(z) \ll 1. \quad (4.30)$$

4.3.3 Experimental characterization

The fabrication process to build the PFCB microring resonators is almost identical to the one described in section 4.2.2. Effort was made to achieve a coupling gap g as small as possible. The limitation on the coupling gap comes mainly from the following two causes. First, the smallest feature size is fundamentally limited by the wavelength of the light source employed in the *i*-line ($\lambda = 365$ nm from

Mercury lamp) projection aligner we used for photolithography. Second, the tight confinement of guided light to reduce the bending loss requires a deep etch into the cladding layer as we discussed earlier. In general, a high RF power and low chamber pressure can increase the anisotropicity (or verticality) in RIE etching, but the side wall etching to a certain degree is unavoidable. Figure 4.13 shows a scanning electron micrograph of a PFCB add-drop microring resonator with a radius of $25\ \mu\text{m}$ and a coupling gap of $0.45\ \mu\text{m}$. A coupling gap down to $0.4\ \mu\text{m}$ with our stepper is possible, but it is very difficult to achieve.

Figure 4.14 illustrates the experimental setup for characterizing the microring devices. We used a Photonetics tunable laser and/or an erbium doped fiber amplifier (EDFA) for light sources. Light was coupled into the waveguide using a conical-shaped lensed fiber, which has a focal length of approximately $8\ \mu\text{m}$. A signal emerging from either the through port or the drop port is collected by a lensed fiber and directed to a detector and a spectrum analyzer. Both the input and output fibers are mounted on 3-axis translation stages from Newport, allowing accurate and stable alignment.

Using a broad band amplified spontaneous emission (ASE) from an EDFA as a light source can be very useful for device alignment because a spectrum analyzer allows us to monitor the spectral response of the device in nearly real-time. Figure 4.15 shows the dropped signal at the drop port of an add-drop filter with a radius of $25\ \mu\text{m}$ when the ASE light is coupled into the input port. As shown in the figure, the measured free spectral range $\lambda_{\text{FSR}} = 9.3\ \text{nm}$. Note that the unpolarized

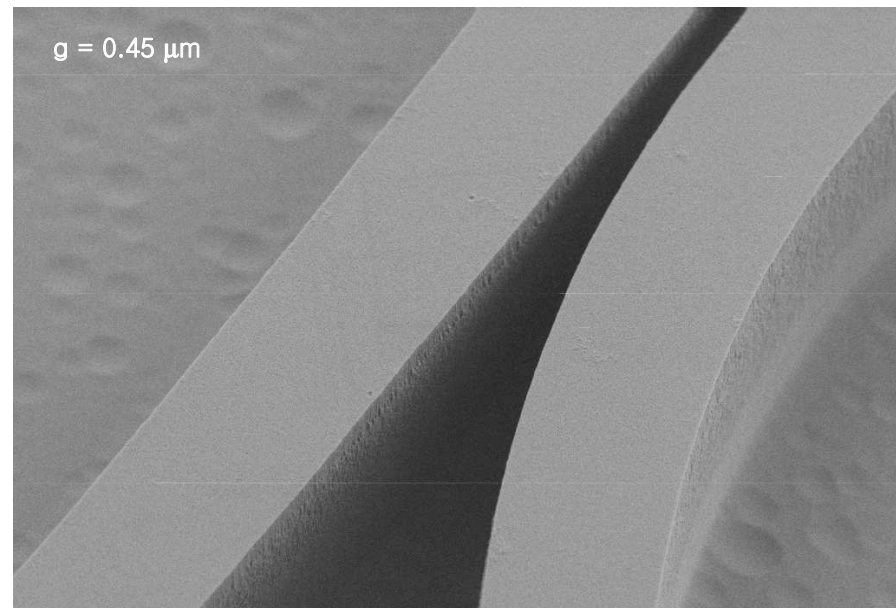
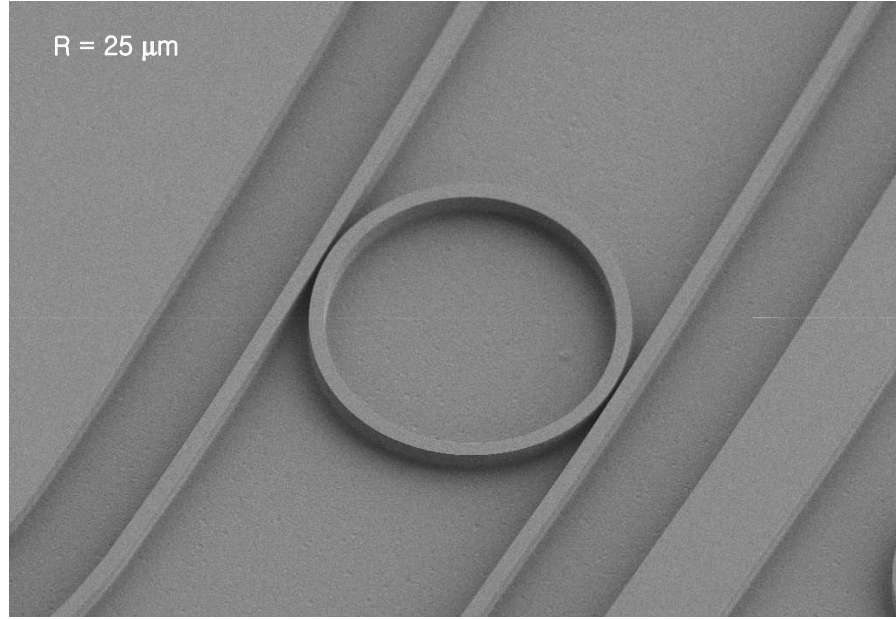


Figure 4.13: Scanning electron micrograph of PFCB ring resonator, with a radius $R = 25 \mu\text{m}$, and a coupling gap $g = 0.45 \mu\text{m}$.

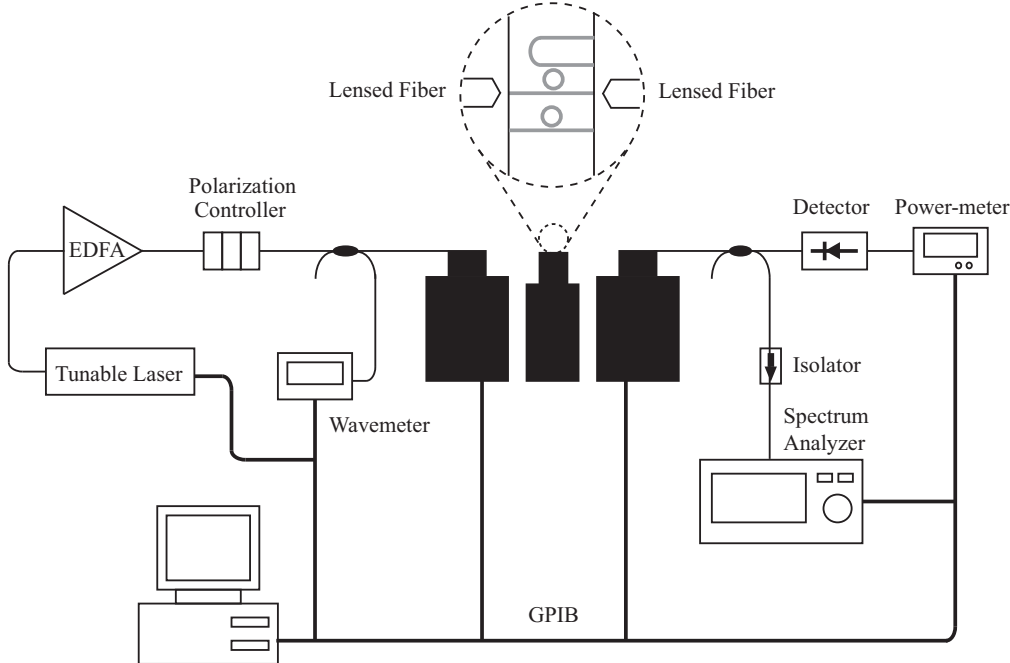


Figure 4.14: Experimental setup for microring characterization.

ASE source shows the resonances for both TE and TM mode, and the different signal intensities for TE and TM can be explained by the polarization dependent scattering loss (PDL) and the difference in coupling constants.

Figure 4.16 plots the normalized signal of the device at the through and drop port at the resonance at 1531.05 nm from a tunable laser input. As shown in the figure, the maximum extinction ratio at the throughput port is 4.87 dB, and the calculated quality factor Q and finesse \mathcal{F} are approximately 8544 and 55, respectively.

In addition, we observed a resonance shift with increasing EDFA input power. When the total ASE power was increased from 4 dBm to 12 dBm, a resonance shift

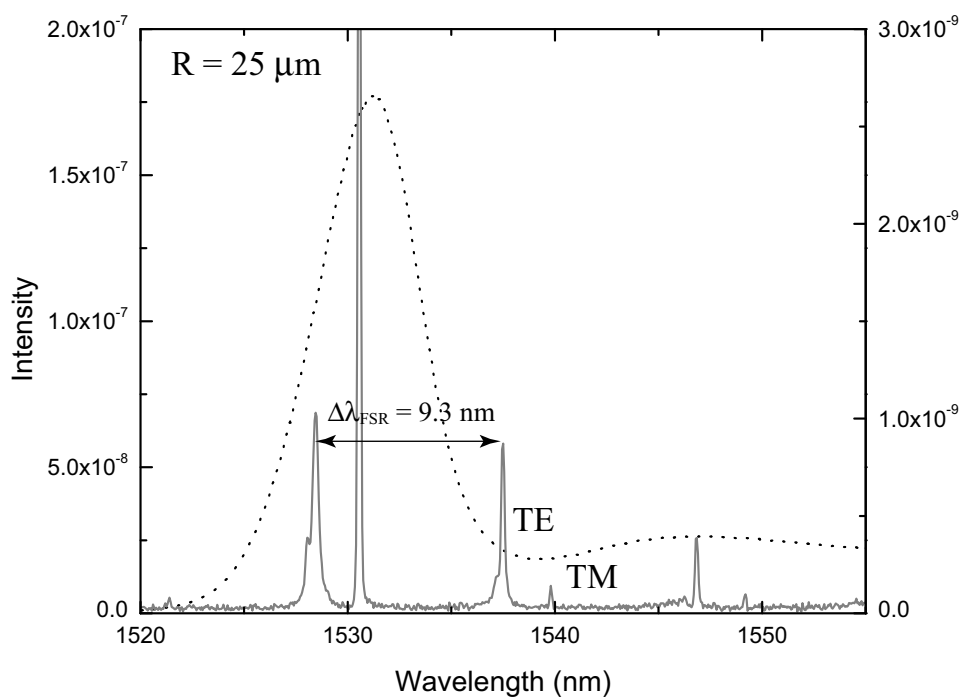


Figure 4.15: Measured spectral response at the drop port of an add-drop filter with a radius $25 \mu\text{m}$ with ASE input (solid line). The measured free spectral range λ_{FSR} is 9.3 nm for TE mode. EDFA spectrum (dotted line) is also plotted as a reference.

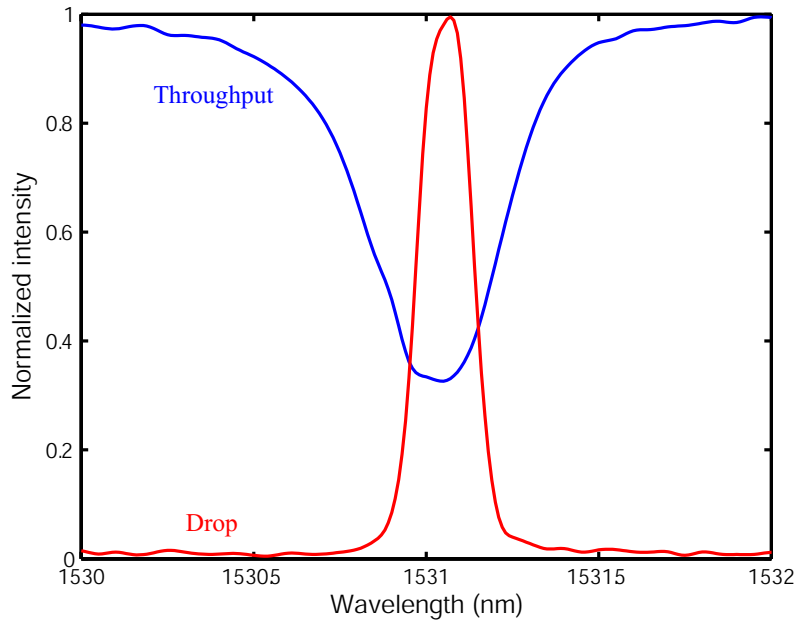


Figure 4.16: Normalized signal of the device at the throughput and drop port at the resonance at 1531.05 nm from a tunable laser input.

of 25 pm was obtained as shown in Fig. 4.17(a). We speculate that the origin of this resonance shift is thermal, based on the observation of the negative thermo-optic coefficients, dn/dT , of the PFCB polymers as shown in Fig. 4.17(b). The thermo-optic coefficient was obtained by measuring refractive indices at different temperatures with a MetriconTM that was custom fitted with temperature control. This negative dn/dT that lowers the mode effective index of the waveguide can qualitatively explain the blue-shift of the resonance with increasing EDFA input power. Similar effects were observed in microrings fabricated from benzocyclobutene (BCB) polymer, and optical bistable switching based on the resonance

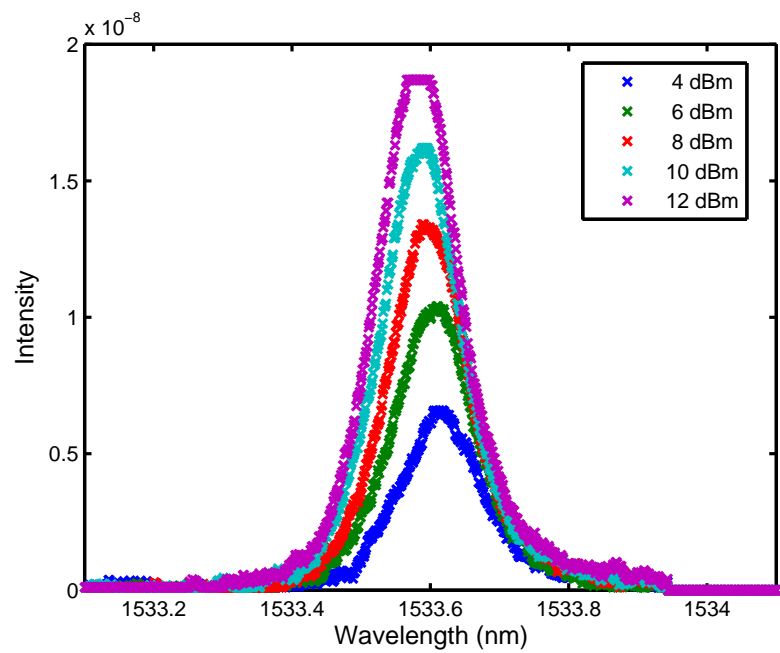
shift was demonstrated by other members in our group [75, 76]. They are currently investigating the subject for more complete understanding of the physical origin.

4.3.4 Ultrafast all-optical switching experiment

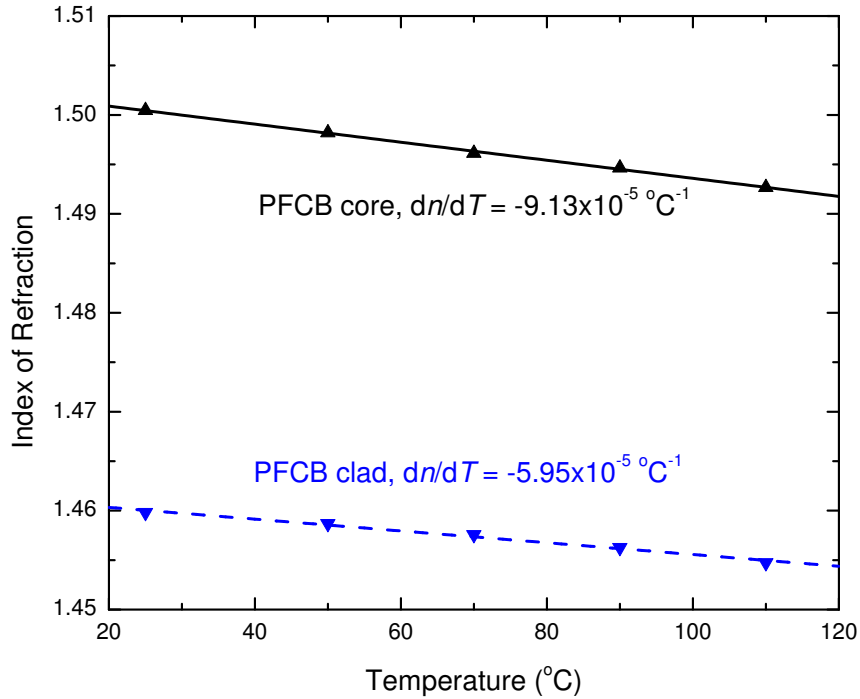
More than two decades ago, ultra-fast optical control of microwave and millimeter wave propagation was reported [77, 78]. This ground work demonstrated phase shifting, switching, and modulating in semiconductor waveguides using a picosecond laser pulse. Likewise, the light signal out of a microring can also be modulated or switched by changing the optical properties of the material with an optical pump that either co-propagates through the ring together with a probe signal [79, 80], or directly illuminates the ring from above. All-optical lightwave switching in GaAs semiconductor microring devices was also achieved by injecting free carriers, generated by absorbing photons with an energy greater than the band gap [81].

In this section, we show that all-optical switching in polymer microrings is possible from preliminary experimental results. The fundamental physics of carrier dynamics in polymer devices is substantially different from the direct optical excitation of electrons and holes for the GaAs semiconductor microring devices. Although it is not clearly understood at this point, the all-optical switching we observed can still be explained by carrier injection (excitons and free carriers), as evidenced by an earlier report on the transient photoconductivity in a BCB polymer film induced by a femtosecond laser pulse [82].

For the switching experiment, we used a microring-loaded Mach-Zehnder inter-



(a) ASE input power vs. resonance shift



(b) Thermo-optic coefficient, dn/dT

Figure 4.17: (a) Resonance shift with increasing ASE input power. Maximum resonance shift 25 pm obtained. (b) Thermo-optic coefficient, dn/dT , measured using a Metricon™ that was custom outfitted with temperature control.

ferometer (MR-MZI) – a microring coupled to one arm of an MZI – fabricated from PCB, which is schematically shown in Fig. 4.18(a). In the experiment, a train of mode-locked Ti:Sapphire laser pulses with a pulse width of 100 fs, a repetition rate of 1 KHz at a wavelength of 400 nm was used for the optical pump beam. When these pump pulses directly illuminate the ring from above, it causes a temporal blue shift of the microring resonance as schematically shown in Fig. 4.18(b). When the probe beam is initially tuned to a wavelength slightly shorter than a ring resonance ($\lambda_p^1 < \lambda_R$ in Fig. 4.18(b)), the probe beam experiences a rapid decrease in transmission temporally due to the resonance shift from λ_R to λ'_R , and hence exhibits High-Low-High modulation behavior. On the other hand, when the probe beam is initially tuned to a resonance ($\lambda_p^2 = \lambda_R$ in Fig. 4.18(b)), the probe beam experiences a rapid increase in transmission, and hence exhibits Low-High-Low modulation behavior. As a result, the train of pulses modulates the probe signal in time as shown in Fig. 4.18(d) and (e), respectively.

In addition to this amplitude modulation from the resonance shift, the optical pump pulse changes the phase near a ring resonance as we discussed in section 4.3.1. Fig. 4.18(c) illustrates the phase response across the resonance. For an MR-MZI, the temporal π phase shift around a resonance of the ring resonator can destructively interfere with the light in the second arm, therefore, as in the amplitude modulation, the train of pulses modulates the probe signal in time as shown in Fig. 4.18(d) and (e), depending on whether the probe signal is initially on-resonance or off-resonance. From the combined effect of amplitude modulation

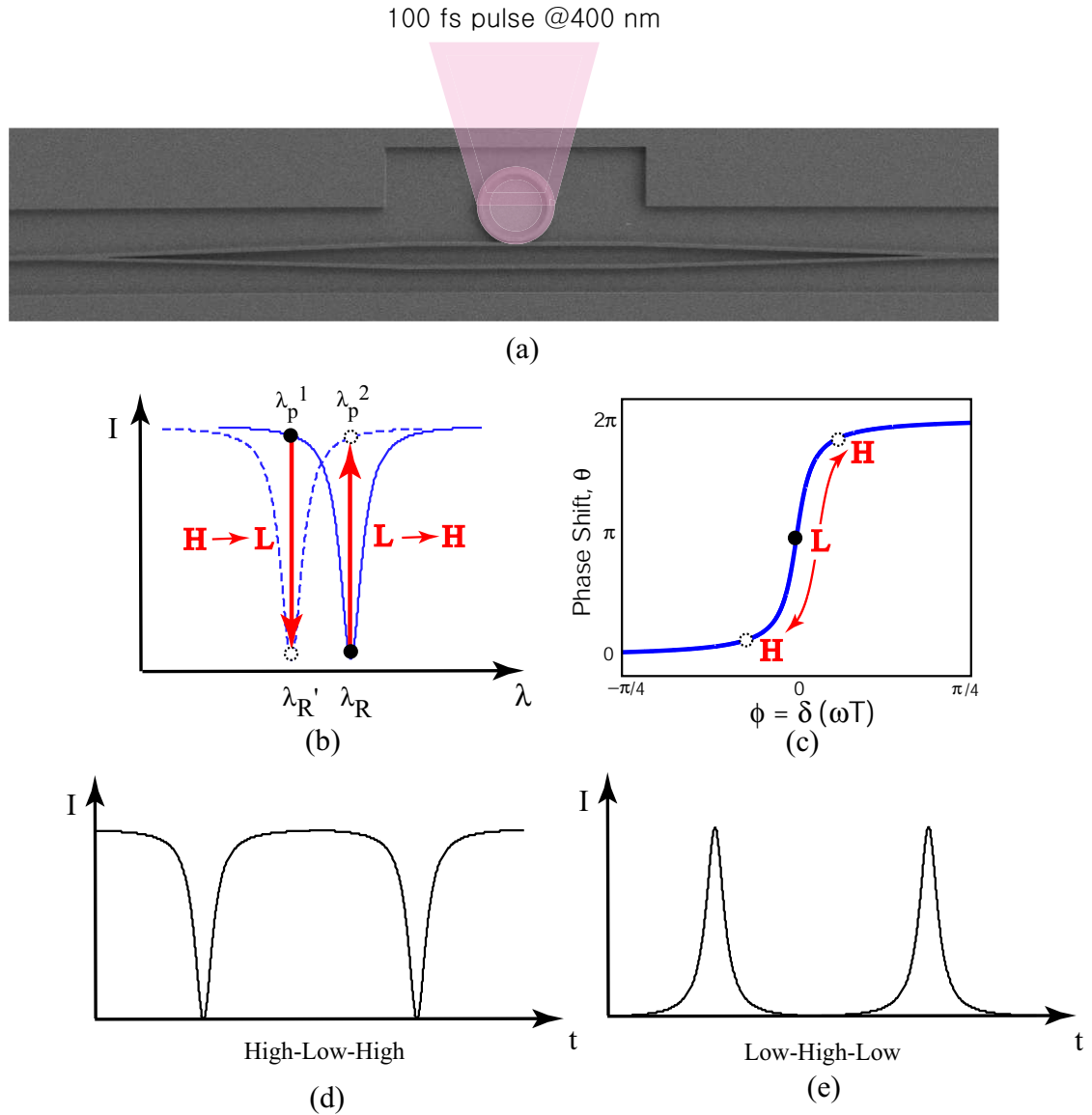


Figure 4.18: Schematic picture of all-optical switching experiment. (a) An optical pump with a 100 fs Ti:Sapphire laser pulse with an energy of 500 pJ/pulse at 400 nm directly illuminates the ring from above. The resulting modulation behavior comes from the combined effect of (b) amplitude and (c) phase modulation. (d),(e) Therefore, the probe signal is modulated in time H-L-H or L-H-L depending on the initial probe wavelength.

and phase modulation, the switching efficiency can be greatly increased around the resonance [83, 84]. However, it should be noted that this phase contribution is significant only when the one arm of the MZI is over-coupled to the ring and the loss in the ring is negligibly small.

The transfer response at the output of an MR-MZI is given by

$$E_t = \frac{E_i}{2} \left\{ |E_r| e^{j\Phi} e^{j\Delta\phi} + 1 \right\} \quad (4.31)$$

where E_r and Φ were given by Eqs. 4.16 and 4.17, respectively, and $\Delta\phi$ is the phase imbalance between the two arms of the MZI. Note that a finite imbalance in length between two arms of an MZI resulting from fabrication imperfection is inevitable and the phase difference ($\Delta\phi = k_0 n_{\text{eff}} \Delta d$) from the length imbalance (Δd) can greatly affect the spectral response of an MR-MZI over a wide range of wavelengths.

The spectral response of an MR-MZI shown in Fig. 4.19 is exaggerated for the case of a length imbalance, $\Delta d = 5 \mu\text{m}$, and a ring radius, $R = 10 \mu\text{m}$. As shown in the figure, when the phase difference between the two arms is close to $\Delta\phi = \pi$, the ring resonances exhibit ‘peaks’ rather than ‘dips’, and when $0 < \Delta\phi < \pi$, the resonance dips show asymmetric profiles. However, the Δd can easily be controlled to less than 100 nm, and therefore the response from an MZI without a microring is essentially flat over a narrow range of wavelengths in most cases.

Figure 4.20 shows the preliminary experimental data showing the modulation (or switching) response of the device ($R = 50 \mu\text{m}$) when a 100 fs Ti:Sapphire laser pulse with an energy of 500 pJ/pulse was used for an optical pump beam. By

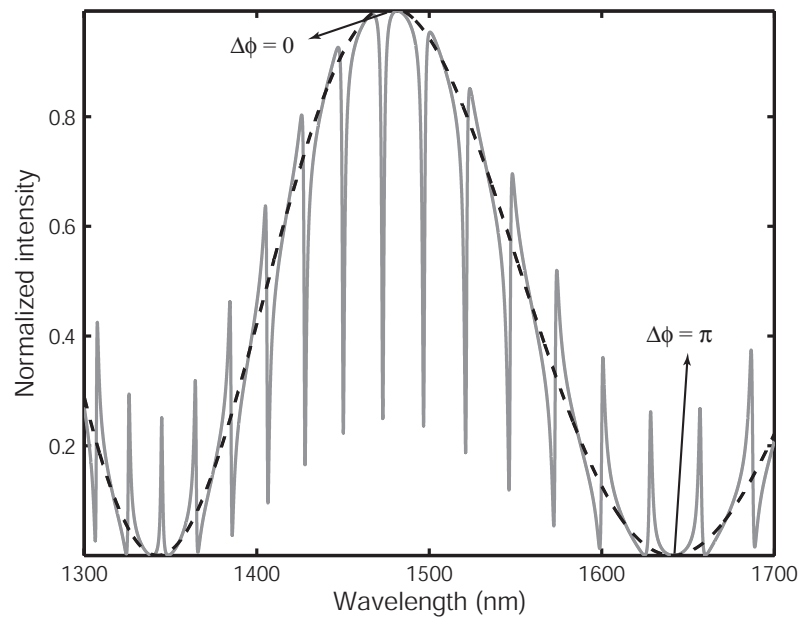
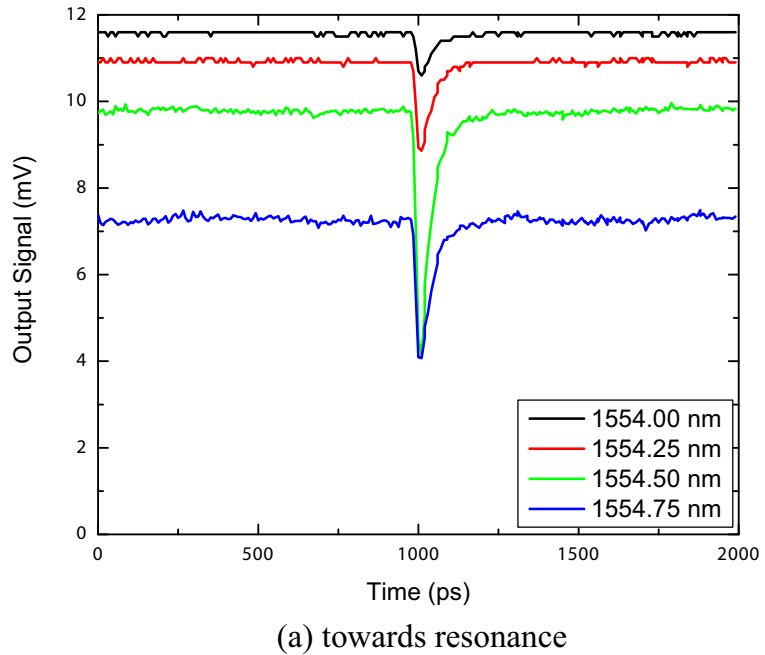


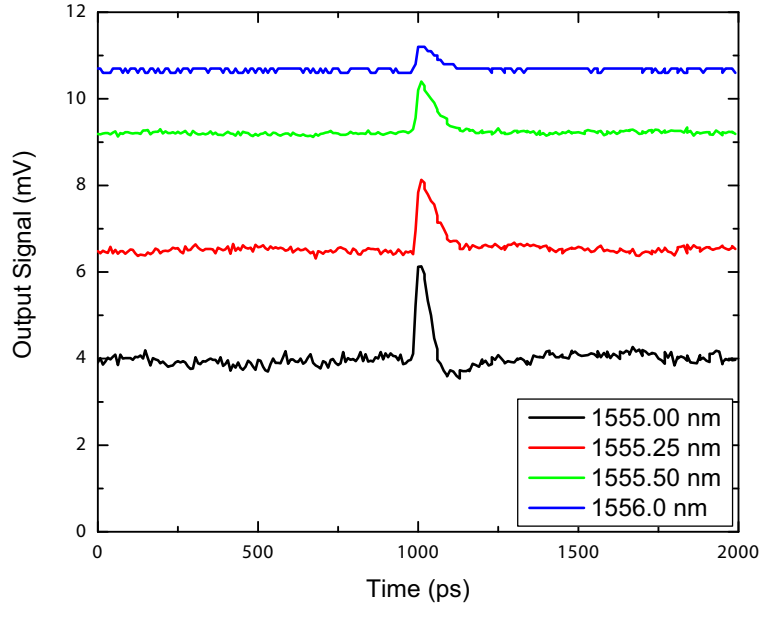
Figure 4.19: Spectral response of an MR-MZI with a length imbalance between two arms of the MZI, $\Delta d = 5 \mu\text{m}$, which is exaggerated for clarity. The microring is critically coupled and has a round-trip loss, $A = 0.95$, an effective index, $n_{\text{eff}} = 1.477$, and a radius of the ring, $R = 10 \mu\text{m}$.

sweeping the wavelength of a probe beam across a ring resonance ($\lambda_R \approx 1554.9$ nm) and detecting the time variation of the transmitted signal, we can estimate how much the resonance is shifted. As shown in the figure, when the probe beam was initially tuned to a wavelength slightly shorter than a ring resonance, and progressively scanned towards the resonance, the dropped probe beam exhibited High-Low-High modulation behavior. On the other hand, when the probe beam was initially tuned to the resonance and scanned away from the resonance, the signal is modulated as Low-High-Low. As discussed before, this can be explained by the temporal change in the optical properties of the PFCB polymer. A response pulse width of about 30 ps, which is primarily limited by the sampling scope used in the measurement, and a maximum modulation depth of 3.8 dB was obtained. Note that the response window is wider in the case that the probe wavelength was scanned away from the ring resonance because of the asymmetric resonance profile arising from length imbalance as shown in Fig. 4.19.

The estimated resonance shift $\Delta\lambda$ is around 0.6 nm, leading to a maximum refractive index change, $\Delta n \approx -5.7 \times 10^{-4}$. From the pulse energy of 500 pJ/pulse used in the experiment, if this resonance shift results from the intensity dependent nonlinear refractive index, $n = n_0 + n_2 I$, from 3rd order nonlinear optical effect, an n_2 on the order of -8×10^{-18} m²/W, and a $|\text{Re}\{\chi^{(3)}\}|$ on the order of 4×10^{-9} esu would be required. This large value of $\chi^{(3)}$ is much higher than one might expect from PFCB, therefore it can be speculated that the observed behavior results from exciton and/or free carrier effects as we observed in the GaAs microring devices.



(a) towards resonance



(b) away from resonance

Figure 4.20: Measured switching response of the MR-MZI when the ring was illuminated by a 100 fs Ti:Sapphire laser pulse with an energy of 500 pJ/pulse at 400 nm. The probe signal was swept through one of the ring resonances, $\lambda_R \approx 1554.9$ nm.

However, the switching efficiency is about two orders of magnitude worse than for the GaAs devices, mainly from the following two reasons. First, the carrier generation efficiency is worse than the one from the conduction–valence interband transition from linear absorption in the GaAs device. Second, a phase contribution to switching is not significant because the ring in our case is under-coupled to the MZI and the loss present in the ring cannot be neglected. Figure 4.21 shows a phase response around a resonance for the all-pass configuration with a round-trip field loss $A = 0.9$ when the field transmission coefficients are $\tau = 0.95$ and $\tau = 0.98$. When the ring is lossy, particularly when the coupling efficiency is very small compared to the loss (for example, solid line in the figure, a round-trip power loss of 19% and a power coupling efficiency of 4%), the effective phase shift Φ shows a very different behavior from the one we discussed in section 4.3.1 and it is much smaller than a radian. Therefore, the phase modulation represented by $e^{j\Phi}$ term in Eq. 4.31 is not significant.

4.4 Summary

In this chapter, we investigated low-loss waveguides and microring resonators fabricated from perfluorocyclobutyl (PFCB) copolymer. Fluorinated polymers are one of the most attractive materials to construct photonic passive waveguides because they have substantially low absorption loss at telecommunication wavelengths. Low-loss waveguides are one of the most important building blocks in integrated-optic communication systems because most passive and active devices consist of

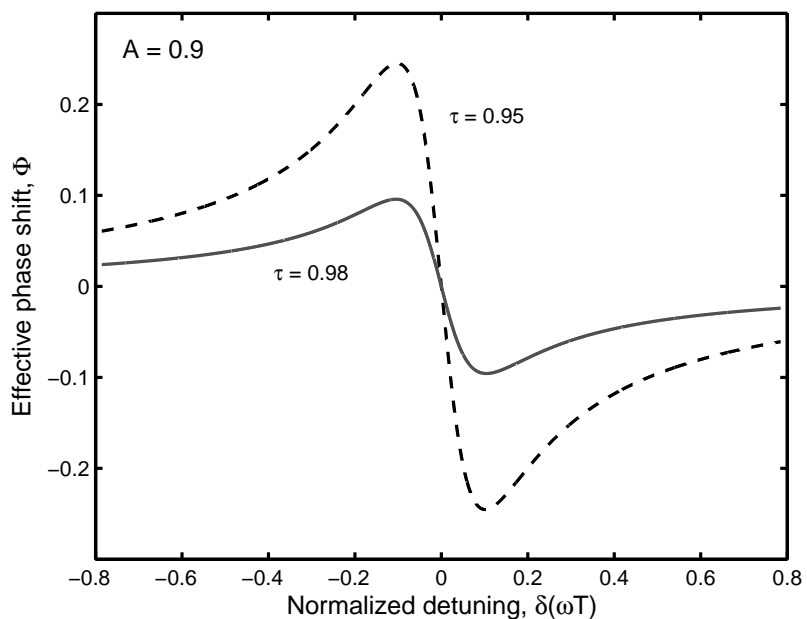


Figure 4.21: Calculated phase response near a resonance in all-pass configuration when the ring is lossy and under-coupled, a round-trip field loss $A = 0.9$, the field transmission coefficients are $\tau = 0.95$ and $\tau = 0.98$.

simple straight and curved waveguide segments. For example, microring resonator based devices have very simple configurations of straight waveguides and circular rings, and the loss present in the ring is the most important parameter determining the device performance. For these reasons, this chapter was devoted to the design, fabrication, and characterization of those devices using PFCB polymers. We demonstrated straight waveguides with propagation losses of 0.3 dB/cm and 1.1 dB/cm for a buried channel and pedestal structures, respectively, and a microring add-drop filter with a maximum extinction ratio of 4.87 dB, quality factor $Q = 8554$, and finesse $\mathcal{F} = 55$. In addition, we showed that all-optical switching with the PFCB microring resonator is possible when it is optically pumped by a femtosecond laser pulse with sufficient energy. From a microring-loaded Mach-Zehnder interferometer (MR-MZI), we demonstrated that a modulation window of 30 ps and modulation depth of 3.8 dB from an optical pump with a pulse duration of 100 fs and pulse energy of 500 pJ when the signal wavelength is initially tuned to one of the ring resonances.

CHAPTER 5

ORGANIC THIN-FILM PHOTODETECTOR BASED ON BULK HETEROJUNCTION

Ever since the discovery of organic semiconducting polymers¹, new avenues for their use as replacement for inorganic semiconductors have been explored. This interest is fueled by their potential capabilities and possibilities for modern electronic and photonic devices, which include light emitting diodes (LEDs) [85, 86], photovoltaic cells (PVs) [87–90], photodetectors (PDs) [91–94], and field effect transistors (FETs) [95–98]. Among these, development of OLEDs has nearly matured and they were recently employed in the commercial flat panel displays for small electronic appliances such as cell phones and PDAs. The commercial success of this technology provided further spur to research on organic photovoltaic cells in particular and organic photodetectors to a lesser extent because of their very low manufacturing cost and substrate flexibility. Because solar energy conversion in OPV cells and light detection in OPDs share a lot of common basic physics, the work on organic thin film photodetectors that we discuss in this chapter has benefited from the ideas developed in the study of OPV cells.

¹This pioneering work on the discovery and development of electrically conductive polymers by Alan J. Heeger, Alan G. MacDiarmid, and Hideki Shirakawa was awarded the Nobel Prize in Chemistry in 2000 [3]

5.1 Basic principles

Charge carrier transport and light absorption in organic semiconducting materials are associated with electronic bands formed by sp^2 -hybridized orbitals of carbon atoms. An electron in the p_z -orbital of each sp^2 -hybridized carbon atom will form π -bonds with neighboring p_z electrons. In conjugated polymers with chains of alternating single–double bond structure, the molecular p_z orbitals constituting the π -bonds are actually overlapped and spread over the entire molecule. The electrons in this molecular orbital are respectively delocalized along the whole molecular chain, resulting in high electron polarizability.

Organic semiconducting polymers have a few distinct features, which distinguish them from their crystalline inorganic counterparts. First, organic materials have poor carrier mobilities, typically less than $1\text{ cm}^2/\text{V}\cdot\text{s}$ in most materials, which is orders of magnitude lower than inorganic semiconductors. The highest mobility reported to date is around $5\text{ cm}^2/\text{V}\cdot\text{s}$ in the pentacene-based field effect transistor through a surface modification [98], and yet this is still two orders of magnitude lower than silicon. Second, most organic semiconductors have absorption peaks located in the visible range with strong absorption coefficients typically greater than 10^5 cm^{-1} . In most practical devices, however, this high extinction requires an active layer thicknesses of only a few hundred nanometers, which partly compensates for the low mobilities. Third, the absorption of incident photons in these materials lead to photo-excitation of excitons (referring to mobile excited states or

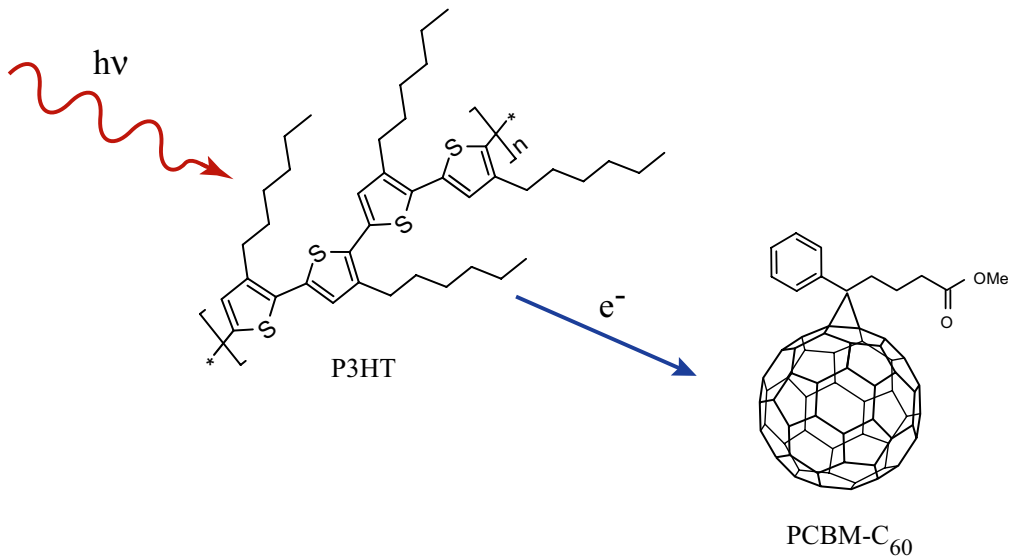


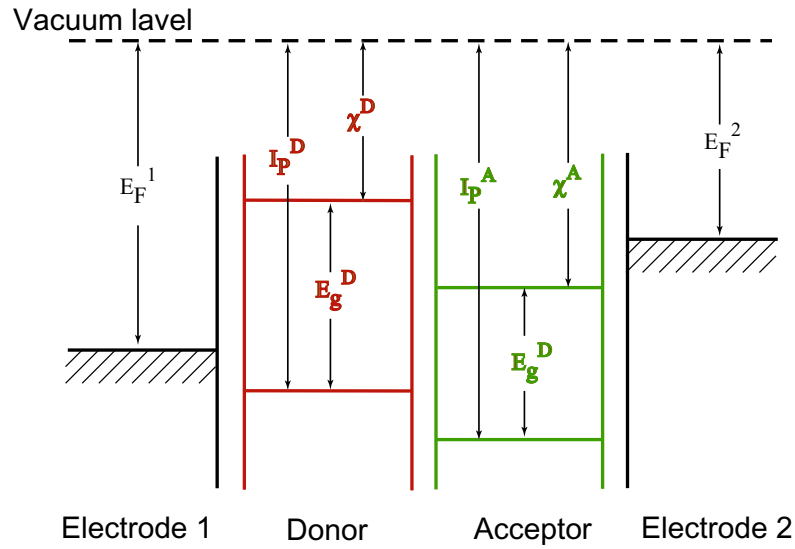
Figure 5.1: Schematic drawing illustrating photoinduced charge transfer between a conjugated polymer (P3HT) and a fullerene (PCBM-C₆₀). After photo-excitation P3HT, the electron is transferred to the PCBM-C₆₀ within 10^{-13} second. With respect to electron transfer, they are often referred to as donor and acceptor materials. In this particular example, P3HT is an electron donor and fullerene is an electron acceptor material.

bound electron-hole pairs via the Coulomb force) rather than free charge carriers. These excitons, an intermediate product in the photocurrent generation process, carry energy but no net charge. Hence they diffuse within the material as a single entity and recombine within distances, typically on the order of 10 nm [99–101]. In solar cells or photodetectors, they need to be *dissociated* non-radiatively by an applied electric field exceeding the exciton binding energy, which can be up to 2 eV, or through a process called *photoinduced charge transfer* [102–105], after which free carriers can be collected at the respective electrodes.

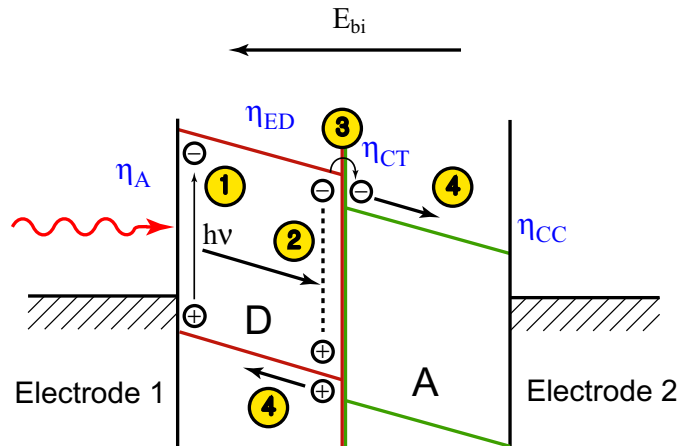
Several approaches of active layer composites for organic PV cells or detectors have been made over the last few decades. The main concepts of these approaches are fundamental photophysics based on the photoinduced charge transfer either between layers of conjugated polymers and low molecular weight organic molecules forming a single heterojunction at the interface, or within a single layer blend of conjugated polymers and low molecular weight organic molecules forming a bulk heterojunction. The very first generation of organic thin film PV cells was based on a single organic layer sandwiched between two metal electrodes of different work functions [88], but the external quantum efficiency (EQE) and hence the power conversion efficiency (PCE) was very poor, generally $\ll 1\%$. The remarkable breakthrough was achieved by introducing bilayer heterojunction and bulk heterojunction devices consisting of buckminster fullerene C₆₀ molecules or soluble derivatives of C₆₀ in addition to the active conjugated polymers. After photo-excitation of the conjugated polymer by an incident light with an energy $\hbar\omega$ greater than the $\pi-\pi^*$ gap, electrons are transferred onto the fullerene molecules due to their high electron affinity. Because an electron is transferred from the *p*-type hole conducting polymer to the *n*-type electron conducting C₆₀, these materials are often referred to as electron donors and electron acceptors, respectively. Fig. 5.2(a) illustrates a schematic energy band diagram of electrodes with their work-functions, and donor/acceptor materials with their ionization potential I_p , electron affinity χ , and energy band-gap E_g between HOMO (highest occupied molecular orbital) and LUMO (lowest unoccupied molecular orbital) levels corresponding to the va-

lence and conduction bands in inorganic semiconductors, respectively. For efficient charge transfer, an exciton binding energy greater than $I_p^D - \chi_p^A$ is required because it is energetically favorable. Detailed time-resolved studies on this photoinduced charge transfer between conjugated polymers and fullerene molecules showed that it occurs within 10^{-13} second after photo-excitation of the polymer, which is nearly 10^3 faster than any other competing process [106]. For this reason, the charge transfer efficiency approaches 100%, resulting in excellent quenching of excitonic photoluminescence from the polymer.

Figure 5.3 depicts conceptually the photoinduced charge transfer in bilayer and bulk heterojunction structures. In the bilayer structure, where the electron donor (*p*-type hole conducting polymer) and electron acceptor (*n*-type electron conducting fullerene) form a well-defined planar interface by sequential deposition or spin-casting of the organic layers, the EQE and PCE are limited primarily by the exciton lifetime before photoexcited excitons recombine or dissociate into free charge carriers at the D-A interface. Therefore, the device thickness should be kept within the exciton diffusion length of the active polymer material for efficient charge transfer. On the other hand, in the bulk heterojunction device, the D-A interface is distributed over the entire active layer structure because both donor and acceptor materials are co-evaporated or blended in solution. Therefore, the interfacial area is increased by a large extent such that the dissociation site at a D-A interface falls within a distance closer than the exciton diffusion length from an each absorbing site. For this reason, the charge generation efficiency in the bulk heterojunction



(a)



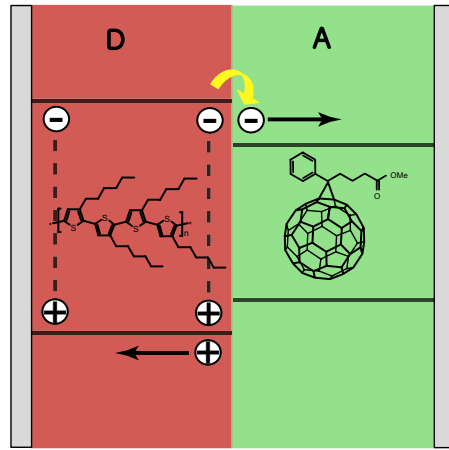
(b)

Figure 5.2: (a) Schematic energy level diagram of electrodes with Fermi energy, and a donor and acceptor materials with energy band-gap E_g between HOMO and LUMO, ionization potential I_p and electron affinity χ . For efficient charge transfer, an exciton binding energy greater than $I_p^D - \chi^A$ is required. (b) Schematic illustration of photocurrent generation in heterojunction PV cells and PDs. Generation of photocurrent consists of four steps: exciton generation, exciton diffusion, exciton dissociation by photoinduced charge transfer, and free charge carrier collection at the electrodes. Therefore, the external quantum efficiency, the ratio of the number of free charge carriers to the number of incident photons, can be expressed with four respectively corresponding efficiencies, η_A , η_{ED} , η_{CT} , η_{CC} .

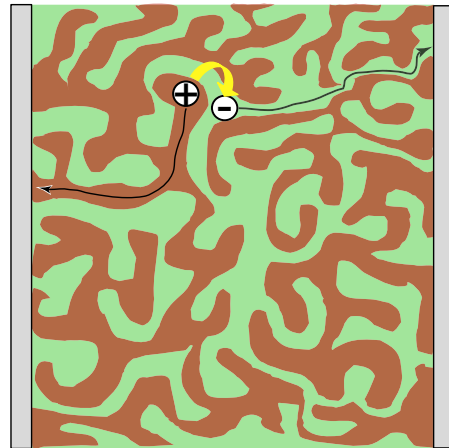
structure is known to be near 100%. However, in such a blended structure, efficient charge transport to the electrodes is sensitive to the nanoscale morphology of the mixture because it requires an intimate interpenetrating network to provide percolated pathways for the hole and electron conducting paths to reach the opposite contacts. Nanomorphology is dependent on many parameters: an evaporation rate, substrate temperature during vacuum deposition process, specific solvents used and solvent evaporation time for solution process like spin-casting, and the annealing condition and relative concentration of the mixture for both processes [90]. It should be noted that charge transport in actual devices can be much more complicated than the continuous conducting paths as illustrated in Fig. 5.3(b) [107].

Photocurrent generation in heterojunction PV cells and PDs consists of four steps and the corresponding efficiencies are defined as:

1. Exciton generation in the electron donor material from incident photons, which is directly related to the material absorption coefficient, (η_A).
2. Exciton diffusion, fraction of excitons generated in the donor material reaching the D-A interface, (η_{ED}).
3. Exciton dissociation at the D-A interface through photoinduced charge transfer, (η_{CT}).
4. Charge collection at the electrodes, (η_{CC}).



(a) Bylayer heterojunction



(b) Bulk heterojunction

Figure 5.3: Schematic diagram depicting conceptually the photoinduced charge transfer in (a) bilayer heterojunction and (b) bulk heterojunction. In a bilayer structure, the electron donor and electron acceptor form a well-defined planar interface by sequential deposition or spin-casting. On the other hand, in a bulk heterojunction, the D-A interface is distributed over the entire active layer structure and its interfacial area is increased by a large extent because both the donor and acceptor materials are co-evaporated or blended in solution.

Therefore, we can write the external quantum efficiency η_{EQE} , which describes the ratio of the number of free charge carriers to the number of incident photons

$$\begin{aligned}
 \eta_{\text{EQE}} &= \frac{I_{\text{ph}}/e}{P_{\text{light}}/(h\nu)} \\
 &= \frac{N_{\text{ex}}}{N_{\text{ph}}} \cdot \frac{N_{\text{ex}}^{\text{DA}}}{N_{\text{ex}}} \cdot \frac{N_{\text{free}}^{\text{DA}}}{N_{\text{ex}}^{\text{DA}}} \cdot \frac{N_{\text{free}}^{\text{A,C}}}{N_{\text{free}}^{\text{DA}}} \\
 &= \eta_{\text{A}} \cdot \eta_{\text{ED}} \cdot \eta_{\text{CT}} \cdot \eta_{\text{CC}} \\
 &= \eta_{\text{A}} \cdot \eta_{\text{IQE}}, \tag{5.1}
 \end{aligned}$$

where $\eta_{\text{IQE}} = \eta_{\text{ED}} \cdot \eta_{\text{CT}} \cdot \eta_{\text{CC}}$ is the internal quantum efficiency (IQE).

In this chapter, we will focus on the bulk heterojunction structure to develop a photodetector with a high EQE. Although there are a number of different organic materials used in photovoltaic applications, including organic dyes or pigments, the most commonly used active materials are, for hole conducting donor materials, MDMO-PPV (poly[2-methoxy-5-(3,7-dimethyloctyloxy)]-1,4-phenylenevinylene), MEH-PPV (poly(2-methoxy-5-(2'-ethylhexyloxy)-1,4-phenylenevinylene)), P3HT (poly(3-hexylthiophene-2,5-diyl)), P3OT (poly(3-octylthiophene)), PFB (poly(9,9'-dioctylfluorene-co-bis-*N,N'*-(4-butylphenyl)-bis-*N,N'*-phenyl-1,4-phenylene diamine), and pentacene, and for electron conducting acceptor materials, CN-PPV (poly(2,5,2',5'-tetrahexyloxy-7,8'-dicyano-di-p-phenylenevinylene), CN-MEH-PPV (poly[2-methoxy-5-(2'-ethylhexyloxy)-1,4-(1-cyanovinylene)-phenylene], F8TB (poly(9,9'- dioctylfluoreneco-benzothiadiazole), fullerene C₆₀ and C₇₀, and chemically modified soluble fullerene derivatives, namely PCBM-C₆₀ ([6,6]-phenyl-C₆₁-butyric acid methyl ester) and PCBM-C₇₀ ([6,6]-phenyl-C₇₁-butyric acid methyl ester).

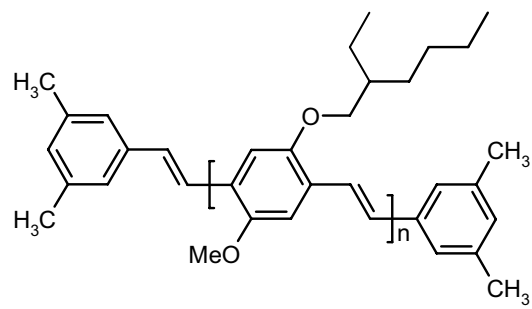
The materials used in this work are conjugated polymers, MEH-PPV and P3HT for electron donors, and small organic molecules, PCBM-C₆₀ and PCBM-C₇₀ for electron acceptor materials. Fig. 5.4 shows the chemical structures of these four materials.

5.2 Fabrication of bulk heterojunction PDs

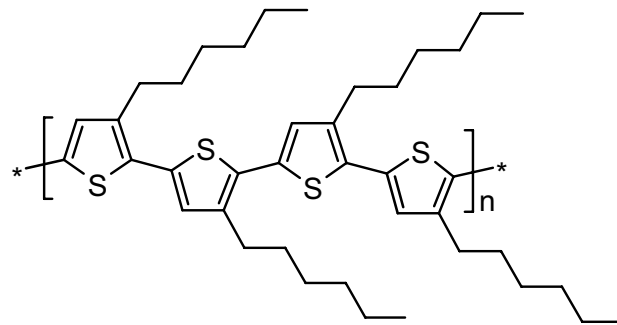
The device structure is shown in Fig. 5.5. Indium-tin-oxide (ITO) on float glass substrate was purchased from Delta Technologies. The transparent conducting oxide, ITO, with a sheet resistance of 4–8 Ω/□ and a thickness of 200 nm was used as the hole injecting electrode. In order to etch parts of the ITO to define several devices on a 1" × 1" ITO/glass substrate, a photoresist pattern was transferred onto the ITO layer by wet chemical etching using diluted HCl². The etch rate can be adjusted by varying the concentration of HCl. The typical etch rate is about 50 Å/min in HCl aqueous solution (1:1, standard 38% HCl to DI water) at room temperature and can be accelerated up to 2000 Å/min in undiluted HCl (38%). A digital voltmeter was used to check whether the ITO was completely cleared without leaving any unwanted residual layer that can short out the device.

Once the patterned ITO/glass substrate was prepared, all the subsequent layers were deposited in an inert N₂ environment in a glove box to avoid photo-oxidative degradation. After solvent cleaning of the ITO/glass substrate, a thin layer (~

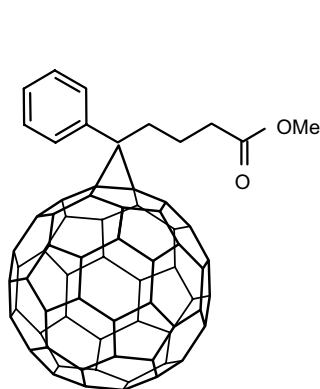
²ITO can be easily removed in HF as well. However, the etch rate is very high and often uncontrollable, and, more importantly, it attacks the glass substrate at the same time. Reactive ion etching in an Ar plasma is an alternative way to etch ITO when the feature size is small.



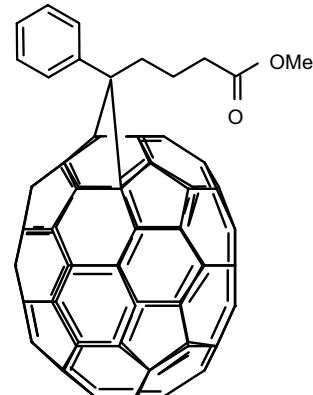
(a) MEH-PPV



(b) P3HT



(c) PCBM-C₆₀



(d) PCBM-C₇₀

Figure 5.4: The chemical structure of the materials in bulk heterojunction layer for organic photodetector. (a) and (b) are electron donor/hole conducting conjugated polymers, MEH-PPV and P3HT, respectively. (c) and (d) are electron acceptor/electron conducting small molecules, PCBM-C₆₀ and PCBM-C₇₀, respectively.

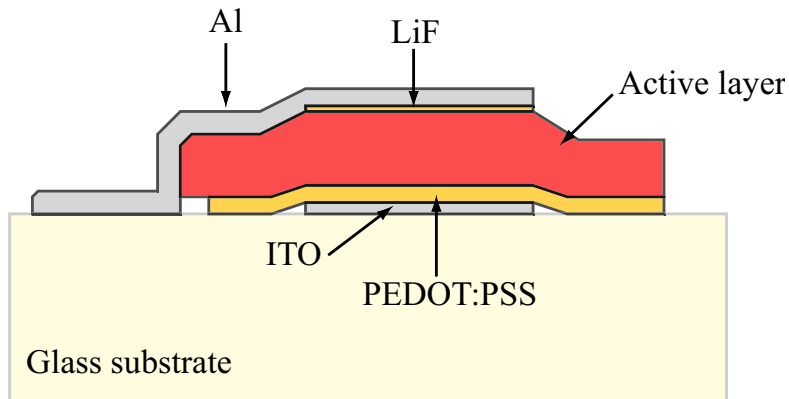


Figure 5.5: Schematic diagram of the device configuration.

50 nm) of PEDOT:PSS (poly[3,4-ethylenedioxythiophene]:poly[styrenesulfonate], LED grade PEDOT Al4083 purchased from Baytron) was spin-coated and followed by annealing at 150 °C for 1 hr. Either ITO or PEDOT:PSS alone can be used as the hole injecting anode, but the ITO/PEDOT:PSS combination employed in OLEDs and OPV cells has given the most promising results for device efficiency as well as lifetime [108–110].

A polymer/fullerene blend was spin-casted and annealed at 100 °C for 1 hr for the active layer with a desired thickness. The materials for the blend are conjugated polymers MEH-PPV and P3HT for electron donors, and small organic molecules PCBM-C₆₀ and PCBM-C₇₀ for electron acceptor materials, all of which were purchased from American Dye Source. Chlorobenzene was used to dissolve both of these organic materials for a solution process because chlorobenzene can provide more uniform mixing of the constituents compared with other organic solvents

such as toluene, which is also frequently used. This more uniform mixing mainly comes from the higher solubility of C₆₀, and results in a smooth surface morphology and hence an improved photocurrent [111]. Separate solutions of polymer and fullerene were prepared and stirred at 80 °C for a few days and then filtered into a pre-cleaned vial to prepare a blend solution with a desired relative concentration of donor/acceptor. The total solution concentration in weight was kept about 1% for a layer with a thickness about 100 nm.

As mentioned earlier, the nanoscale morphology of the active layer in a bulk-heterojunction is an important factor because the presence of an intimate interpenetrating network between the electron donor and acceptor materials is critical for efficient charge transport. For this reason, a detailed study was conducted earlier in our group (R. Barber, W. Herman, and D. Romero) to investigate how the morphology and device characteristics depend on the relative concentration of the active layer blend [112, 113].

Figure 5.6 shows the atomic force microscopy (AFM) images for four different PCBM-C₆₀ molar fractions in the blend with a block copolymer MEH-PPV-co-biphenylene vinylene [113]. The molar fraction of PCBM-C₆₀ x is defined as

$$x = \frac{W_{C_{60}}/MW_{C_{60}}}{W_{C_{60}}/MW_{C_{60}} + W_{\text{poly}}/MW_{\text{poly}}}. \quad (5.2)$$

Therefore, $x = 1$ denotes pure C₆₀, $x = 0$ denotes pure MEH-PPV polymer, and $x = 0.5$ corresponds to the blend containing one C₆₀ molecule for every repeating unit of the polymer. The AFM images of different surface morphologies with

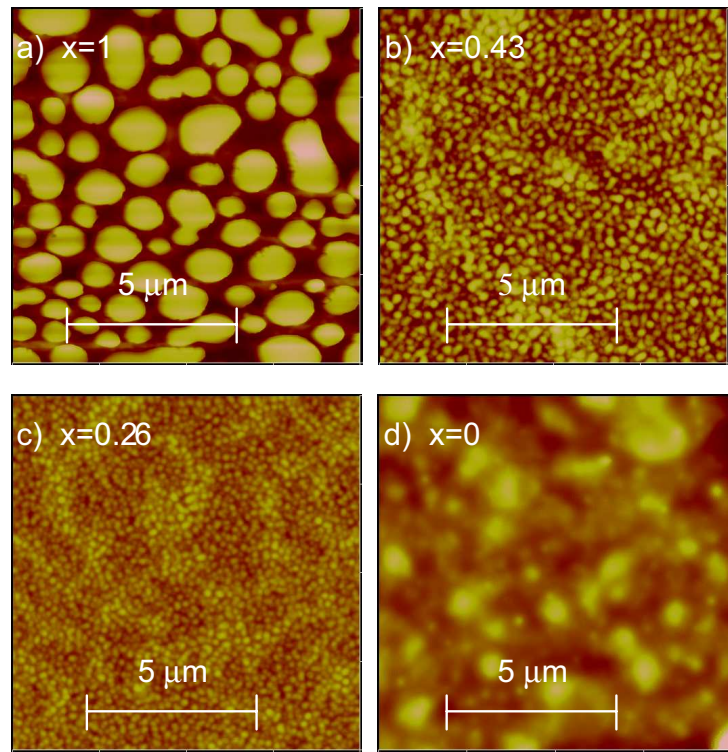


Figure 5.6: Atomic Force Microscopy (AFM) images for four different PCBM-C₆₀ molar fractions x [113].

varying fullerene concentrations clearly show that smooth morphology with uniform fine grains (~ 100 nm), rather than segregated large clusters ($\sim 1\ \mu\text{m}$) can be achieved at intermediate values of x .

Further study on photovoltaic device characteristics depending on fullerene concentration showed that when the molar fraction of C₆₀ in the MEH-PPV copolymer/C₆₀ blend is around 0.6 (or equivalently, 3:1 in weight for this particular example), the device exhibits the best performance in terms of short circuit current, fill factor, EQE, and PCE [113]. Note that the optimized relative ratio can be significantly different when other materials are used. For instance in P3HT/C₆₀ blend, the optimized ratio is close to $x = 0.17$ (or equivalently, 1.1:1 in weight for this particular example).

For an electron-injecting top contact, a ~ 1 nm thick layer of lithium-fluoride (LiF) followed by a ~ 60 nm thick layer of aluminum (Al) was deposited on top of the organic layer via shadow mask technique using a thermal evaporator inside the glove box. Similar to the case of the ITO/PEDOT:PSS combination that was used for the hole-injecting electrode for the purpose of energy barrier engineering, a very thin layer of LiF was inserted between the active layer and the Al cathode in order to enhance the electron injection efficiency [114, 115].

5.3 Device characteristics

Characterization of the devices was performed under an AM 1.5 solar simulator with an intensity of 92 mW/cm² and/or using a CW laser at a wavelength of 532 nm

with a maximum output power of 5 W.

A practical figure of merit for PV cells is the PCE (η_P), which is defined as the ratio of the maximum electrical power generated to the incident light power [116],

$$\begin{aligned}\eta_P &= \frac{\max\{I \cdot V\}}{P_{\text{light}}} \\ &= \frac{I_{\text{SC}} \cdot V_{\text{OC}}}{P_{\text{light}}} FF,\end{aligned}\quad (5.3)$$

where $\max\{I \cdot V\}$ is the maximum electrical power that the device can deliver to an external load, P_{light} is the incident light power, I_{SC} is the short-circuit current (current at zero voltage), V_{OC} is the open-circuit voltage (voltage intercept at zero current), and FF is the fill factor defined as

$$FF = \frac{\max\{I \cdot V\}}{I_{\text{SC}} \cdot V_{\text{OC}}}, \quad (5.4)$$

The PCE can also be expressed with the EQE (η_{EQE}) and the energy conversion efficiency (ξ_{en}) at a particular wavelength as

$$\eta_P = \eta_{\text{EQE}} \cdot \xi_{\text{en}} \cdot FF, \quad (5.5)$$

with

$$\eta_{\text{EQE}} = \frac{I_{\text{ph}}/e}{P_{\text{light}}/(h\nu)}, \quad (5.6)$$

$$\xi_{\text{en}} = \frac{eV_{\text{OC}}}{h\nu}. \quad (5.7)$$

Note, however, that Eqs. 5.5–5.7 are more useful for describing the detector response at a particular wavelength because PV cell are characterized under AM

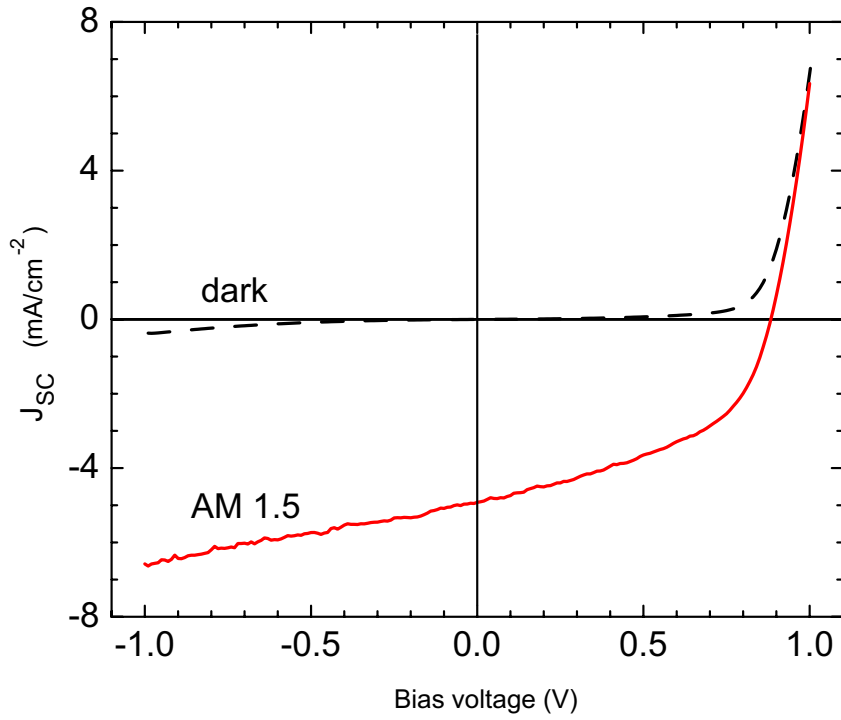


Figure 5.7: Current versus voltage (I - V) characteristics of the bulk heterojunction device of MEH-PPV copolymer and PCBM- C_{60} with a C_{60} molar fraction $x = 0.57$. $V_{OC} = 0.88$ V, $J_{SC} = 4.92$ mA/cm 2 , $FF = 0.47$, and $\eta_P = 2.4\%$ under AM1.5 direct solar simulator with $P_{in} = 92$ mW/cm 2 [113].

1.5 solar illumination in most cases. The incident photon to current conversion efficiency ($IPCE$),

$$IPCE[\%] = \frac{1240 \cdot I_{SC}[\mu A]}{\lambda[nm] \cdot P_{light}[W]} \quad (5.8)$$

is often used instead of EQE (η_{EQE}), but they are equivalent to each other.

Figure 5.7 shows the current versus voltage (I - V) characteristics in the dark and under solar illumination for the bulk heterojunction device of MEH-PPV copolymer and PCBM- C_{60} with a C_{60} molar fraction $x = 0.57$. We can extract the PV

characteristics of the device, $V_{OC} = 0.88$ V, $J_{SC} = 4.92$ mA/cm², $FF = 0.47$, and $\eta_P = 2.4\%$ under AM 1.5 direct solar simulator with $P_{in} = 92$ mW/cm².

A practical figure of merit for PDs is the EQE or photo-responsivity at a certain wavelength, while it is the PCE for the PV cells. In order to describe an overall detector performance, a high EQE alone is not sufficient and other parameters such as dark current, noise equivalent power, dynamic range, and response time, should be considered as well. However, a high EQE is a prerequisite. Although a detector can be used in ‘PV mode’, operating without any bias voltage applied, most detectors operate under reverse bias voltage for fast carrier sweep within the active layer. Therefore, depending on whether the device is employed as a solar cell or a detector, a slightly different approach is needed. Our primary interest in the rest of this chapter is to improve the EQE at the wavelengths of peak detector responsivity by increasing the photocurrent under reverse bias.

Figure 5.9 shows the I - V characteristics of the bulk heterojunction detector of P3HT/PCBM-C₆₀ with a relative ratio, C₆₀/P3HT = 1.15 in weight, (a) under AM 1.5 solar illumination and (b) under different laser intensities at 532 nm. As shown in Fig. 5.8, the absorption peak of the blend of P3HT/PCBM-C₆₀ is near 532 nm, and hence the maximum detector responsivity is expected at around 532 nm as well. Although the PCE under solar illumination is poor $\eta_P < 0.5\%$ mainly due to the small fill factor $FF \approx 0.2$, the EQE is around 0.3 at short circuit condition and approaches 0.6 at $V = -10$ V as shown in the figure. These lower PCE but higher EQE, in comparison with the previous device from MEH-PPV/C₆₀ ($\eta_p = 2.4\%$

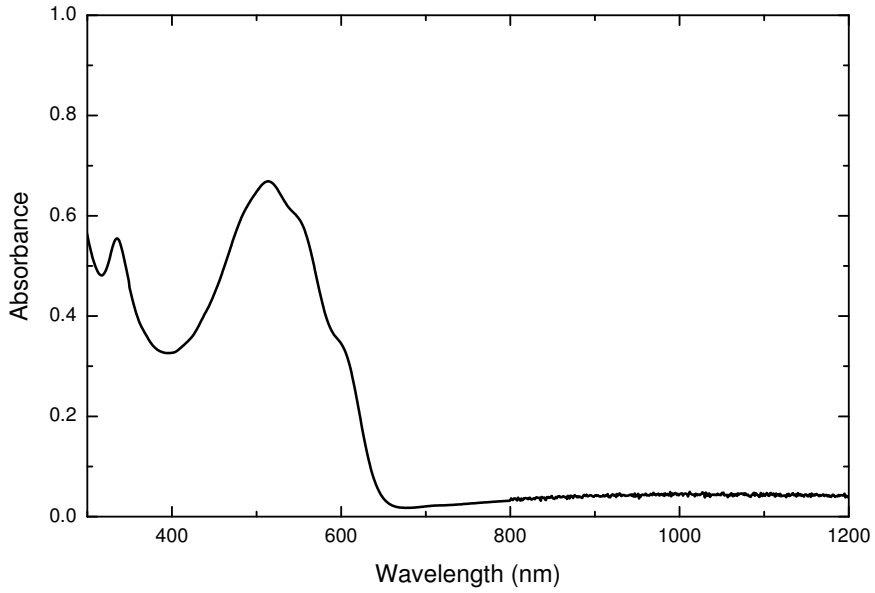
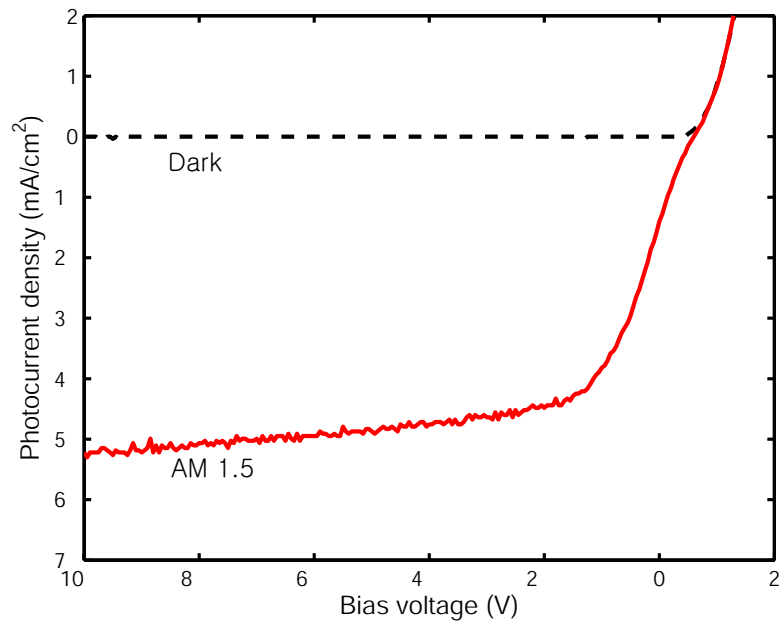
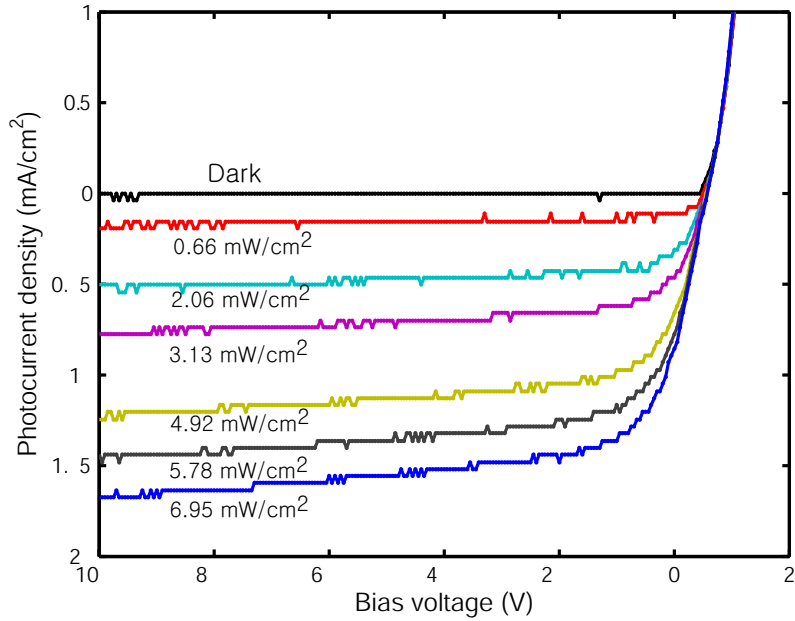


Figure 5.8: Absorption spectra of the blend of P3HT/PCBM-C₆₀. The absorption peak of the blend of P3HT/PCBM-C₆₀ is near 532 nm.

and $\eta_{\text{EQE}} < 0.1$) reported in the earlier work [113], clearly indicate that an efficient PV cell with a high PCE is not necessarily an efficient detector requiring a high EQE and a slightly different approach is needed depends on whether the device is employed as a solar cell or a detector. The value of EQE achieved ($\eta_{\text{EQE}} = 0.3$ and 0.6 at $V = 0 \text{ V}$ and -10 V , respectively) is reasonably high, but in order to improve it further, we need to estimate how many photons arrive and are absorbed within the active layer by taking into account of multilayer thin film interference effects.



(a) under solar AM 1.5 illumination



(b) under laser (@ 532 nm) illumination

Figure 5.9: $I-V$ characteristics of the bulk heterojunction device of P3HT and PCBM-C₆₀ with a C₆₀/P3HT 1.1 in weight, (a) under AM 1.5 direct solar illumination (b) under different laser intensities at 532 nm.

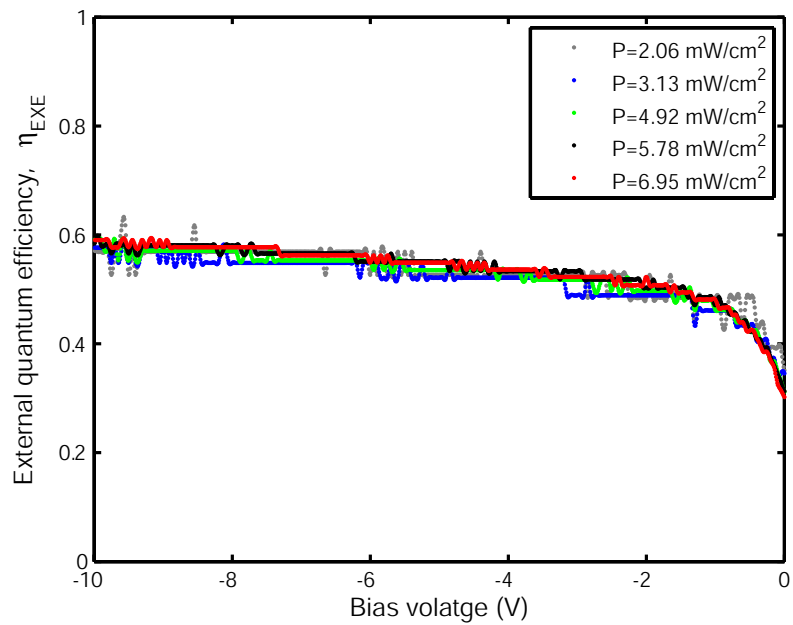


Figure 5.10: External quantum efficiency vs. bias voltage of the device from P3HT and PCBM-C₆₀ at 532 nm. η_{EQE} is around 0.3 at short circuit condition and approaches 0.6 at $V = -10 \text{ V}$.

5.4 Multilayer thin film interference effects

Because the number of excitons generated is directly related to the absorption of optical energy, in order to improve the external quantum efficiency, the first step to consider is maximizing the number of photons that arrive in the active layer, where photoexcited excitons are generated and dissociated into free carriers.

Because the exciton diffusion and dissociation efficiencies are near 100% in the bulk heterojunction as mentioned in section 5.1, we can define a theoretical upper limit of EQE that assumes all the free carriers from the dissociated excitons are collected at the respective electrodes ($\eta_{CC} = 1$). We expect that this upper limit of EQE can be nearly achieved when the detector is under a relatively strong reverse bias.

For the estimation of EQE, a model including interference effects from multiple reflection and transmission at each interface is necessary to calculate the optical field distribution in each layer. This interference effect is particularly important when there is a very strong reflection at the conducting electrode and polymer interface as the case of our device. When considering a device model of a stratified structure, knowledge of the complex refractive indices and thicknesses of all the layers is a prerequisite.

5.4.1 Optical properties of individual layers

For the numerical modeling to calculate the optical field profile in the stratified structure, the complex refractive indices and thicknesses of individual layers were

determined by a spectroscopic ellipsometry (J.A. Wollam) employing a model fitting procedure using the *Drude-Lorentz* model [117, 118]. The complex dielectric function $\tilde{\epsilon}(\omega)$ in the Drude-Lorentz model can be expressed as

$$\tilde{\epsilon}(\omega) = \epsilon_R - j\epsilon_I \quad (5.9)$$

$$= \epsilon_\infty + \frac{f_0\omega_p^2}{-\omega^2 + j\omega\Gamma_0} + \sum_{k=1}^n \frac{f_k\omega_p^2}{(\omega_k^2 - \omega^2) + j\omega\Gamma_k}, \quad (5.10)$$

where ω_p is the plasma frequency and n is the number of Lorentz oscillators with a center frequency of ω_k , a strength of f_k and a damping constant Γ_k . This Drude-Lorentz model combines the free-electron model to represent intraband optical transition and the bound-electron model for interband effects. In general, there can be one or more Lorentz oscillators depending on the material. The complex index of refraction \tilde{n} can be determined from the complex dielectric function:

$$\tilde{n} = \sqrt{\tilde{\epsilon}} = n - jk. \quad (5.11)$$

Figure 5.11 (a) shows the measurement result for the real and imaginary index of refraction of the ITO on soda lime glass substrate. For the model fit to extract n and k from ellipsometric data, one Lorentz oscillator in the Drude-Lorentz model ($n = 1$ in Eq. 5.10) was enough to achieve an excellent fit in the case of ITO [119]. Also note that the thickness obtained from a profilometer was used for an initial guess value in the fitting procedure.

In order to validate the measurement of the complex refractive index, the values of n and k , and the thickness from the best-fit model for the ellipsometric data

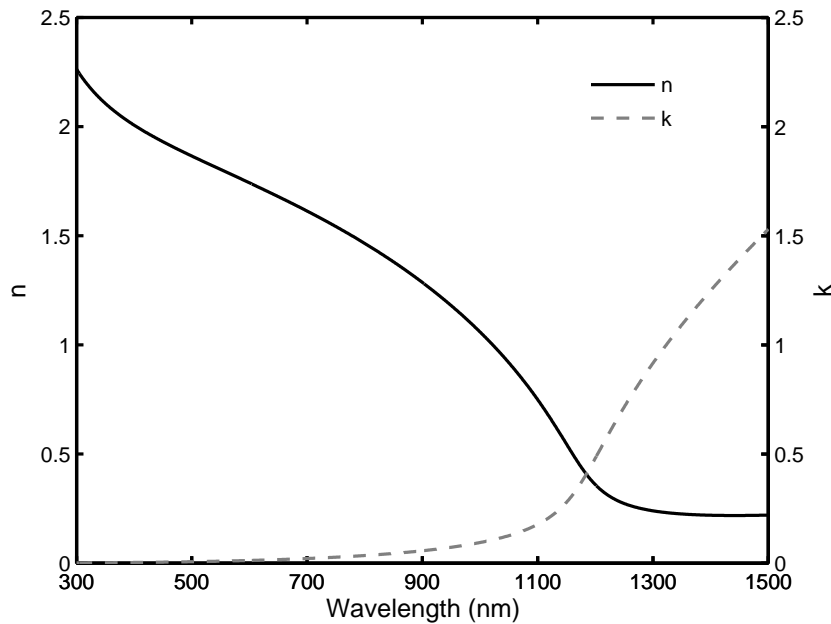
were used to generate the transmission data, and the generated transmission curve was compared with the experimentally measured UV/Vis/IR transmission from a spectrophotometer as shown in Fig. 5.11 (b).

With the same procedure as ITO, the optical properties and thicknesses of other layers were also determined. Figure 5.12 shows the n and k for Al, PEDOT:PSS, and P3HT:C₆₀. The optical properties of LiF were not shown in the figure because the index dispersion of LiF is very flat, ~ 1.39 , in both the visible and near-IR region, and absorption in a 1 nm thick LiF layer is negligible.

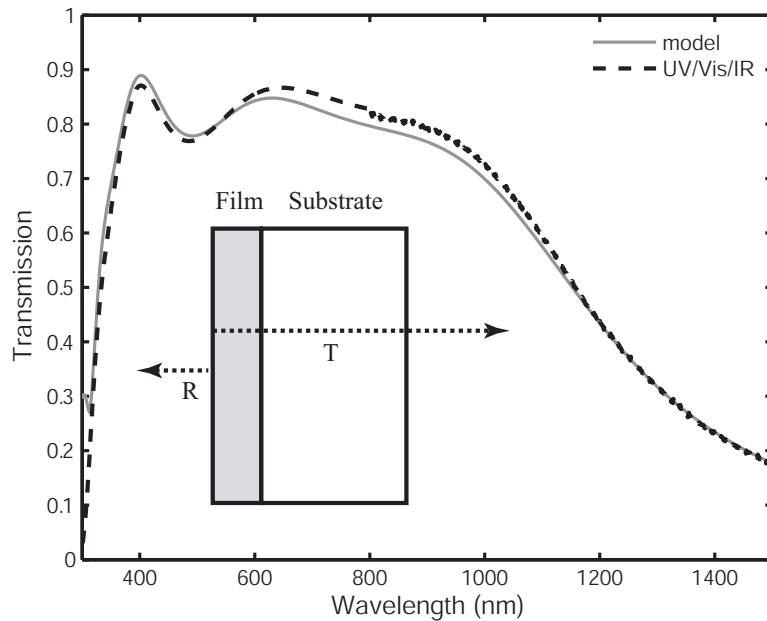
5.4.2 Effect of multilayer thin film interference

Once all the optical properties and thicknesses of individual layers were determined as discussed in the previous section, we can calculate the optical field distribution and absorption of light in each layer of the stratified device structure. Although there are a few different ways to perform the calculation, we follow the approach of the work reported in [91, 101]. In this model, we assume a plane wave incident normal to the device, homogeneous and isotropic layers, and parallel and smooth interfaces.

To calculate the optical electric field as a function of position within the device, consider the schematic diagram of the multilayer structure of the device as shown in Fig. 5.13. The field in the i -th layer has two components, \mathbf{E}_i^+ and \mathbf{E}_i^- , propagating in the positive and the negative z direction, respectively. In this case, the electric field of the light can be represented by a 2×2 matrix because equations

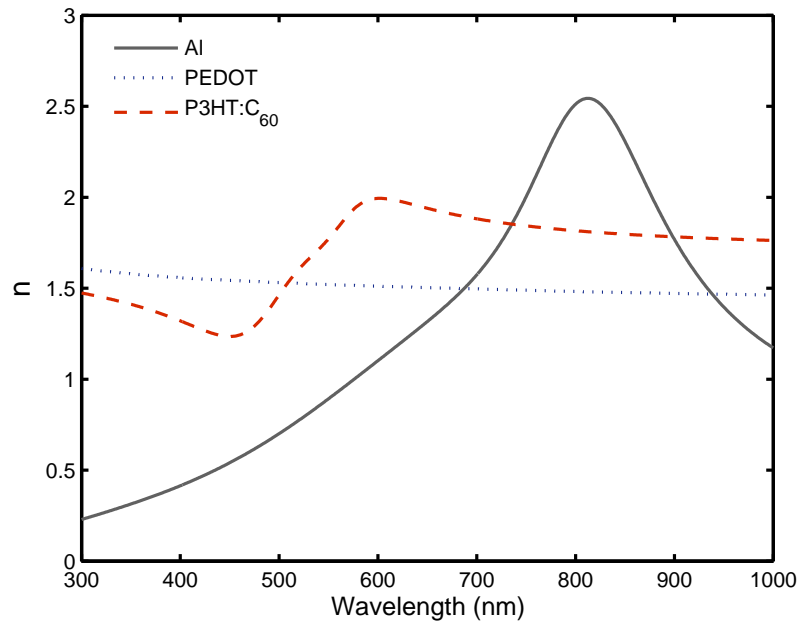


(a) n and k of ITO film

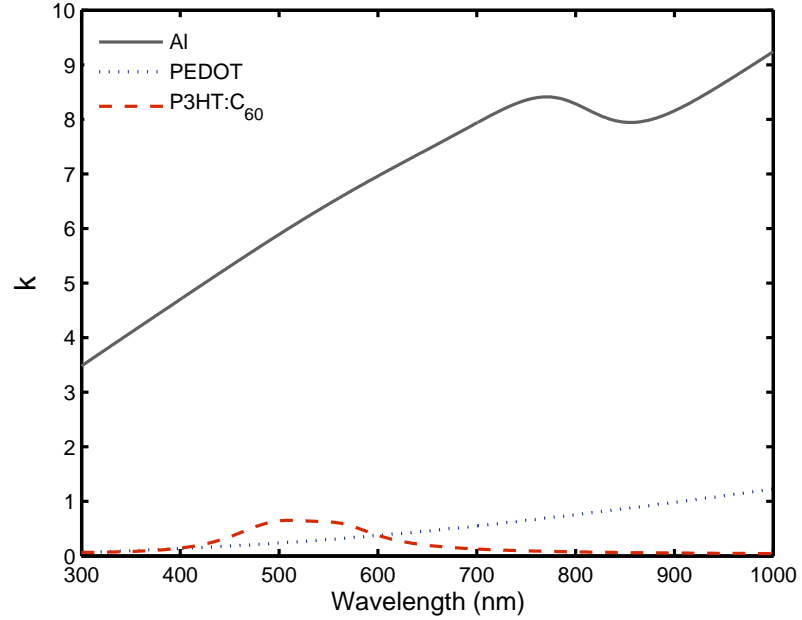


(b) Transmission of ITO/glass sample

Figure 5.11: (a) Real and imaginary index of refraction measured from the spectroscopic ellipsometric data and model fit with the Drude-Lorentz model. (b) Comparison between the estimated transmission using the n and k , and thickness from the best-fit model and the measured transmission from a spectrophotometer.



(a)



(b)

Figure 5.12: Optical properties of Al, PEDOT:PSS, and P3HT:C₆₀

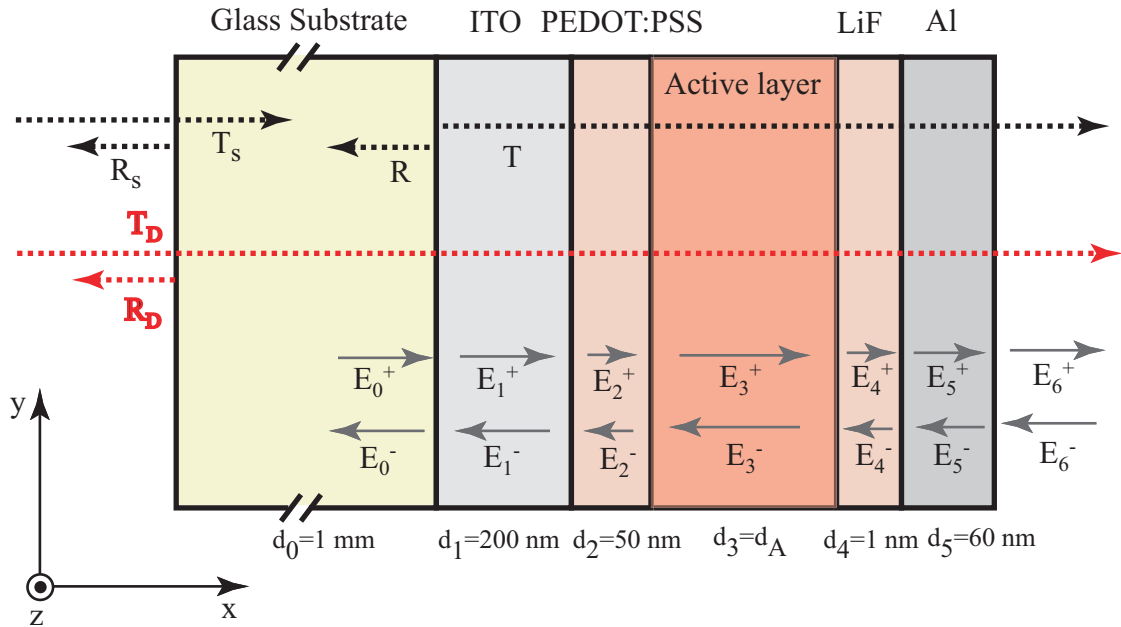


Figure 5.13: Schematic diagram of the multilayer device structure with the thicknesses and the optical electric fields in each layer, \mathbf{E}_i^+ and \mathbf{E}_i^- , representing the component propagating in the positive and the negative z direction, respectively.

describing the light propagation are linear, and the tangential components of the field are continuous across the interface. In this particular example, five thin film layers are stacked to form the actual device. A 1 mm thick glass substrate was not directly included in the thin-film analysis because the light travelling within the glass substrate could be treated as effectively incoherent light by considering the average effect combining the angular dispersion of incident light, the finite bandwidth of the light source, and the surface roughness and nonuniformity in the thickness of the substrate. The substrate effect can be incorporated by considering the reflectivity R_D and transmissivity T_D of the entire device after we calculate R

and T of the multilayer structure, i.e.

$$R_D = \frac{R_S + R - 2R_S R}{1 - R_S R}, \quad (5.12)$$

$$T_D = \frac{T_S T}{1 - R_S R}, \quad (5.13)$$

$$A_D = 1 - R_D - T_D, \quad (5.14)$$

with

$$R_S = \left| \frac{1 - \tilde{n}_0}{1 + \tilde{n}_0} \right|^2, \quad (5.15)$$

$$T_S = n_0 \left| \frac{2}{1 + \tilde{n}_0} \right|^2, \quad (5.16)$$

where R_S and T_S are respectively the reflectivity and transmissivity at the air/glass interface, A_D is the total absorption in the device, and \tilde{n}_0 is the complex refractive index of the glass substrate.

To calculate the optical fields as a function of position in the most general case, consider m layers and corresponding fields \mathbf{E}_i ($i = 0 \dots m + 1$). Then we can write an expression that relates the two outermost fields \mathbf{E}_0 and \mathbf{E}_{m+1} ,

$$\begin{bmatrix} \mathbf{E}_0^+ \\ \mathbf{E}_0^- \end{bmatrix} = \mathbf{S} \cdot \begin{bmatrix} \mathbf{E}_{m+1}^+ \\ \mathbf{E}_{m+1}^- \end{bmatrix}, \quad (5.17)$$

with the scattering matrix \mathbf{S} defined as

$$\begin{aligned} \mathbf{S} &= \begin{bmatrix} S_{11} & S_{12} \\ S_{21} & S_{22} \end{bmatrix} \\ &= \left\{ \prod_{p=1}^m \mathbf{I}_{(p-1)p} \mathbf{L}_p \right\} \cdot \mathbf{I}_{m(m+1)}, \end{aligned} \quad (5.18)$$

where \mathbf{I}_{ij} is the interface matrix representing the reflection and transmission at the $i-j$ interface and \mathbf{L}_i is the layer matrix representing a phase change through the i -th layer as defined below.

$$\mathbf{L}_i = \begin{bmatrix} e^{jk_0\tilde{n}_i d_i} & 0 \\ 0 & e^{-jk_0\tilde{n}_i d_i} \end{bmatrix}, \quad (5.19)$$

$$\mathbf{I}_{ij} = \begin{bmatrix} \frac{1}{t_{ij}} & \frac{r_{ij}}{t_{ij}} \\ \frac{r_{ij}}{t_{ij}} & \frac{1}{t_{ij}} \end{bmatrix}, \quad (5.20)$$

$$r_{ij} = \frac{\tilde{n}_i - \tilde{n}_j}{\tilde{n}_i + \tilde{n}_j}, \quad (5.21)$$

$$t_{ij} = \frac{2\tilde{n}_i}{\tilde{n}_i + \tilde{n}_j}, \quad (5.22)$$

where $\tilde{n}_i = n_i - jk_i$ is the complex refractive index and d_i is the thickness of the i -th layer. Note that the complex Fresnel reflection coefficient r_{ij} and transmission coefficient t_{ij} are the same for TE and TM modes when the light is incident normal to the surface.

When light is incident on the glass and travels through the device in the $+x$ direction and $\mathbf{E}_{m+1}^- = 0$, we can obtain the complex coefficients r and t .

$$r = \frac{\mathbf{E}_0^-}{\mathbf{E}_0^+} = \frac{S_{21}}{S_{11}}, \quad (5.23)$$

$$t = \frac{\mathbf{E}_{m+1}^+}{\mathbf{E}_0^+} = \frac{1}{S_{11}}, \quad (5.24)$$

Therefore, the reflectivity R and transmissivity T described in Fig. 5.13 can be

written as

$$R = |r|^2, \quad (5.25)$$

$$T = \frac{|t|^2}{n_0}. \quad (5.26)$$

To obtain the electric field within the i -th layer, the total multilayer transfer matrix can be divided into two subsets, \mathbf{S}_i^L and \mathbf{S}_i^R . Hence, we can write an expression

$$\mathbf{S} = \mathbf{S}_i^L \mathbf{L}_i \mathbf{S}_i^R, \quad (5.27)$$

with

$$\mathbf{S}_i^L = \left\{ \prod_{p=1}^{i-1} \mathbf{I}_{(p-1)p} \mathbf{L}_p \right\} \cdot \mathbf{I}_{(i-1)i}, \quad (5.28)$$

$$\mathbf{S}_i^R = \left\{ \prod_{p=i+1}^m \mathbf{I}_{(p-1)p} \mathbf{L}_p \right\} \cdot \mathbf{I}_{m(m+1)}. \quad (5.29)$$

From the equations above, we can obtain the electric field propagating in the $+x$ direction in the i -th layer with respect to the incident optical field,

$$\mathbf{E}_i^+ = t_i^+ \mathbf{E}_0^+ = \frac{\frac{1}{S_{i11}^-}}{1 + \frac{S_{i12}^- S_{i21}^+}{S_{i11}^- S_{i11}^+} e^{-j2k_0 \tilde{n}_i d_i}} \mathbf{E}_0^+, \quad (5.30)$$

Similarly the electric field propagating in the $-x$ direction in the i -th layer with respect to the incident optical field is given by,

$$\mathbf{E}_i^- = t_i^- \mathbf{E}_0^+ = \frac{\frac{S_{i21}^+}{S_{i11}^- S_{i11}^+} e^{-j2k_0 \tilde{n}_i d_i}}{1 + \frac{S_{i12}^- S_{i21}^+}{S_{i11}^- S_{i11}^+} e^{-j2k_0 \tilde{n}_i d_i}} \mathbf{E}_0^+. \quad (5.31)$$

Therefore, the total electric field in the i -th layer at an arbitrary distance x to the

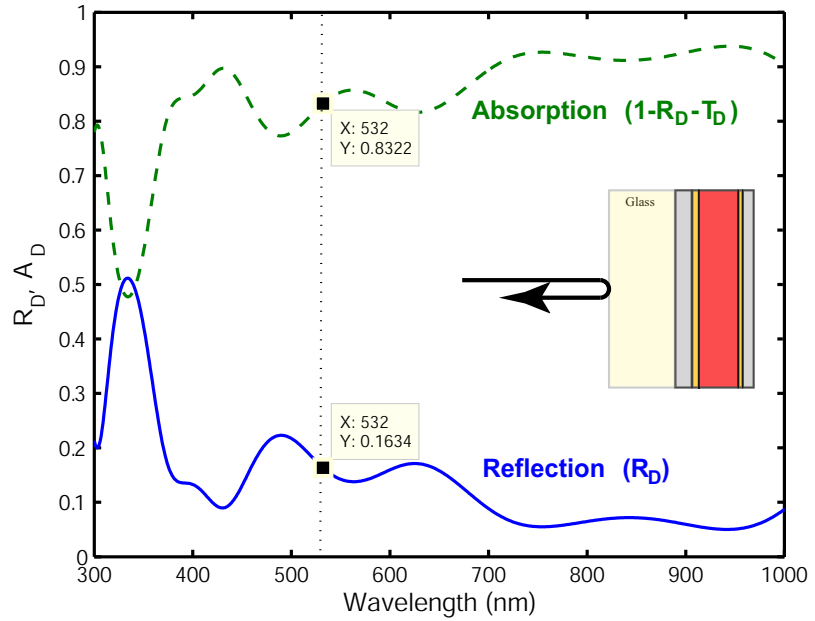


Figure 5.14: Calculation of reflectivity R_D and absorption $A_D = 1 - R_D - T_D$ of the device illustrated in Fig. 5.13 with a bulk heterojunction active layer P3HT/C₆₀ with a thickness 100 nm.

right of the $(i-1)/i$ interface can be written as

$$\mathbf{E}_i(x) = \mathbf{E}_i^+(x) + \mathbf{E}_i^-(x) \quad (5.32)$$

$$= (t_i^+ e^{-jk_0 \tilde{n}_i d_i} + t_i^- e^{jk_0 \tilde{n}_i d_i}) \mathbf{E}_0^+. \quad (5.33)$$

Figure 5.14 depicts the calculated reflectivity R_D and absorption $A_D = 1 - R_D - T_D$ of the bulk heterojunction device from P3HT/C₆₀ with a thickness of 100 nm. Interestingly, at a wavelength of 532 nm, about 16.3% of the total incident photons are reflected at the air/device interface and do not even reach the active layer to generate excitons. This reflectivity is much higher than the 4%

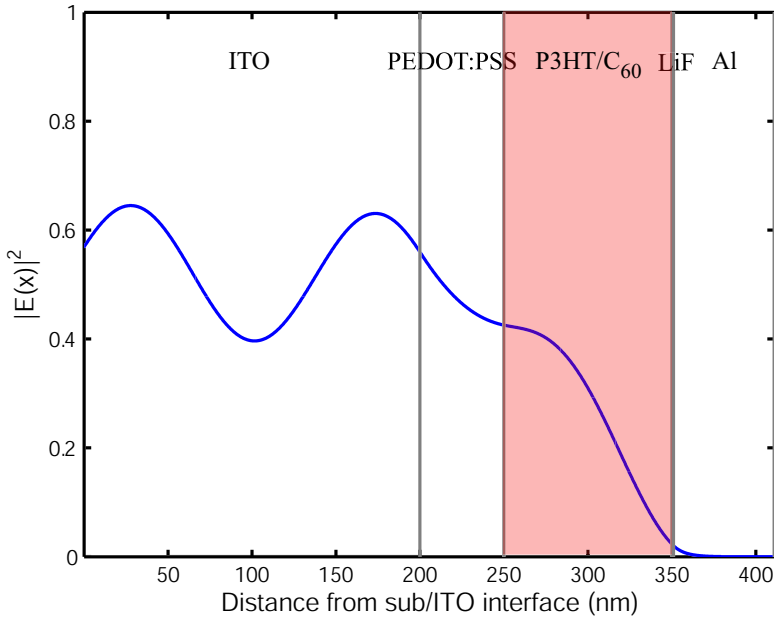


Figure 5.15: Calculation of field distribution as a function of position. Modulus squared of the optical electric field $|E(x)|^2$ is normalized to the incident light field $|E_0^+|^2$.

reflection at a simple air/glass interface, which might have been expected. This calculation directly indicates how strongly the multilayer interference depends on how we construct the practical device structure. It also clearly states that the external quantum efficiency – the fraction of incident photons in the device that can contribute to the photocurrent – can never exceed 83.2%, which is the total light absorption in the entire device. In other words, if all the absorbed photons could contribute to the photocurrent, an EQE of 83.2% would be obtained.

Figure 5.15 shows the calculated field distribution as a function of position. The modulus squared of the optical electric field $|E(x)|^2$ is normalized to the incident

light field $|\mathbf{E}_0^+|^2$.

It is worth pointing out that a detailed field profile within the active layer is very crucial in a bilayer structure because, in order to maximize the number of excitons at the donor/acceptor interface, where the excitons dissociate most efficiently into free carriers, a global peak of $|\mathbf{E}(x)|^2$ needs to be located near the interface [101]. However, this is not the primary factor determining the EQE in the bulk heterojunction device.

Once the optical field profile is found, we can calculate the time-averaged absorbed power or the number of absorbed photons as a function of position, which is directly proportional to the number of excitons generated.

$$\begin{aligned} Q_i(x) &= \alpha_i I_i(x) \\ &= \frac{1}{2} c \epsilon_0 n_i \alpha_i |\mathbf{E}_i(x)|^2 \\ &= \frac{2\pi c \epsilon_0 n_i k_i}{\lambda} |\mathbf{E}_i(x)|^2, \end{aligned} \quad (5.34)$$

where α_i is the absorption coefficient, and $I_i(x)$ is the light intensity in the i -th layer.

Figure 5.16 plots the calculated absorbed power $Q(x)$ as a function of position. Note that the simple exponential model $Q(x) = \alpha I_0 \exp(-\alpha x)$, neglecting multiple reflections and transmissions at the interfaces between the layers, can only give an approximate exciton generation profile [120, 121]. The total absorbed light within the active layer only is given by

$$I_{\text{abs}}^{\text{A}} = \int_{d_{\text{A}}} Q_{\text{A}}(x) dx, \quad (5.35)$$

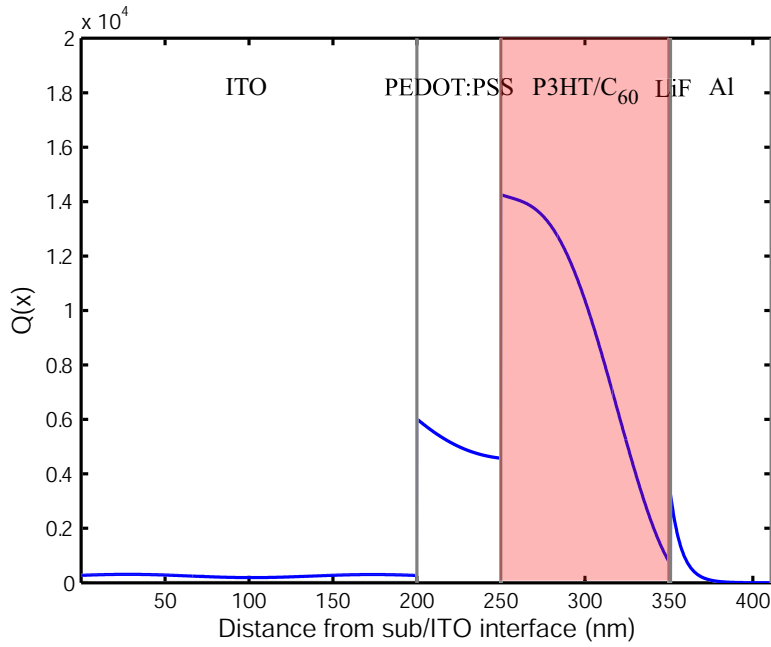


Figure 5.16: Calculation of time-averaged absorbed power $Q(x)$ as a function of position.

and we can define the upper limit to the external quantum efficiency $\eta_{\text{EQE}}^{\text{L}}$ as

$$\eta_{\text{EQE}}^{\text{L}} = \frac{I_{\text{abs}}^{\text{A}}}{I_{\text{inc}}}, \quad (5.36)$$

where I_{inc} is the intensity of the incident light. This $\eta_{\text{EQE}}^{\text{L}}$ represents the theoretical upper limit of EQE that can be achieved from a specific device structure once all the optical properties and thicknesses of individual layers are measured. In other words, we can achieve $\eta_{\text{EQE}}^{\text{L}}$, the maximum incident photons to current conversion efficiency, when all the photons absorbed in the active layer contribute to the photocurrent. This is equivalent to assuming that the internal quantum efficiency η_{IQE} is unity, i.e. the exciton diffusion η_{ED} , exciton dissociation η_{CT} , and charge

collection efficiency η_{CC} in Eq. 5.6 are 100%.

It should be noted that, for a comprehensive theoretical estimation of the EQE, we need to solve the one-dimensional steady-state carrier transport equation and current density equation [122, 123].

$$D \frac{d^2}{dx^2} n(x) + \mu E \frac{d}{dx} n(x) - \frac{n(x)}{\tau} + \frac{\gamma Q(x)}{h\nu} = 0 \quad (5.37)$$

$$J(x) = q\mu E n(x) + qD \frac{d}{dx} n(x) \quad (5.38)$$

where D is the diffusion constant, μ is the charge mobility, E is electric field, $n(x)$ is the carrier density, τ is the carrier life-time, and γ is the carrier generation rate, which is equivalent to $\eta_{ED} \cdot \eta_{CT}$. However, it is not straightforward to solve this carrier transport equation numerically, mainly because it is a multi-point boundary value problem requiring all the boundary conditions at the interfaces. In addition, the field-dependence of the charge mobility cannot be neglected under strong electric fields associated with the applied reverse bias. Therefore determining the charge mobility becomes very crucial in the calculation.

Nevertheless, the η_{EQE}^L is still a very useful quantity for the photodetector under applied fields $E \gg 10^6 \text{V/m}$ because, under such strong fields, η_{CC} can easily reach 80–90%, and this leads to a value of EQE about 80–90% of η_{EQE}^L .

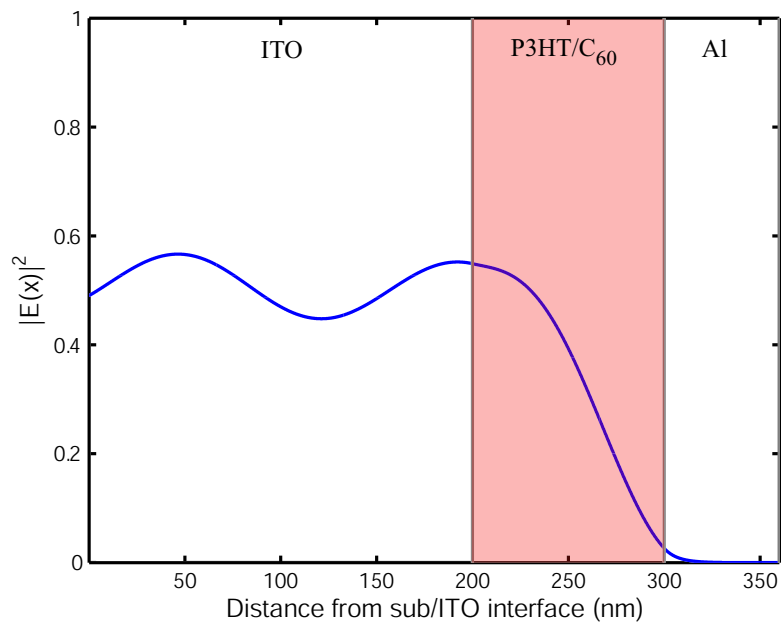
The calculated η_{EQE}^L for the device structure above is 0.69. Therefore, the EQE we obtained ($\eta_{EQE} = 0.6$ at -10V as shown in Fig. 5.10) is 87% of η_{EQE}^L , leading to $\eta_{CC} = 0.87$.

5.5 Improvement of the external quantum efficiency

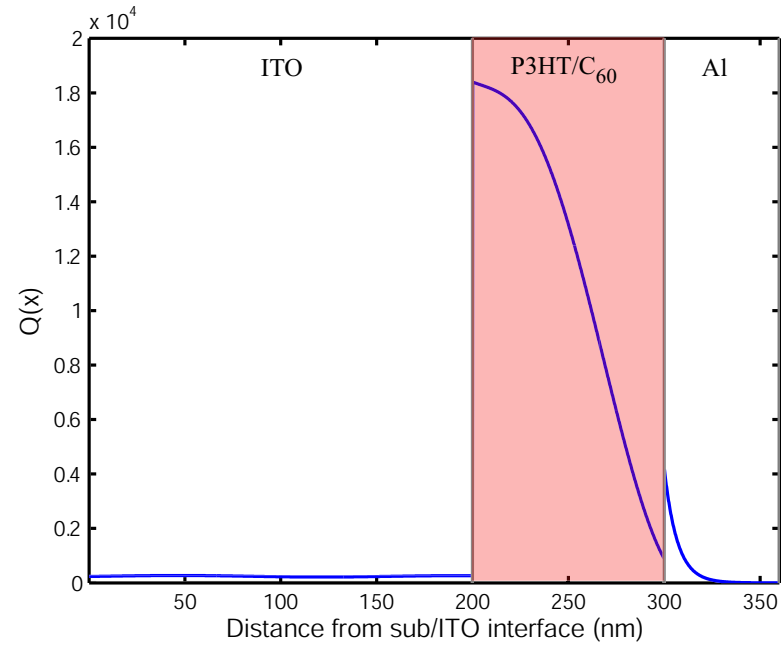
So far, we used PEDOT:PSS and LiF together with ITO and Al, respectively, to form electrodes for more efficient hole and electron injection. This is a desirable approach to achieve high short-circuit currents and high PCE in PV cells by compensating energy level offset or band bending at non-ideal ohmic contacts. In the detector, however, the carriers are expected to have enough energy to overcome these energy level misalignments under a strong applied reverse bias. In addition, the PEDOT:PSS layer absorbs a non-negligible amount of photons and reduces the number of photons absorbed within the active layer.

Figure 5.17 shows the calculated field profile $|\mathbf{E}|^2$ and time-averaged absorbed power Q as a function of position in the case where there is no PEDOT:PSS and LiF. As we might have expected, the upper limit of the external quantum efficiency $\eta_{\text{EQE}}^{\text{L}}$ increases to 87.8% from 69% in the previous case of glass/ ITO/ PEDOT:PSS/ P3HT:C₆₀/ LiF/ Al.

In order to study the active layer thickness d_A dependence on η_{EQE} , we fabricated devices with three different thicknesses shown in Fig. 5.18 with a structure of glass/ITO/P3HT:C₆₀/Al. Figure 5.19 plots the calculation of $\eta_{\text{EQE}}^{\text{L}}$ with (dotted line) and without PEDOT:PSS and LiF (solid line) and measured EQE at -10 V (triangles). Interestingly, when PEDOT:PSS and LiF are used, the EQE has a global peak value of 0.69 at a thickness of 100 nm and has a local minimum of 0.60 at a thickness of about 170 nm, which can be explained by multilayer interference



(a)



(b)

Figure 5.17: Calculation of field distribution $|E(x)|^2$ and time-averaged absorbed power $Q(x)$ as a function of position for the device structure of glass/ITO/P3HT:C₆₀/Al.

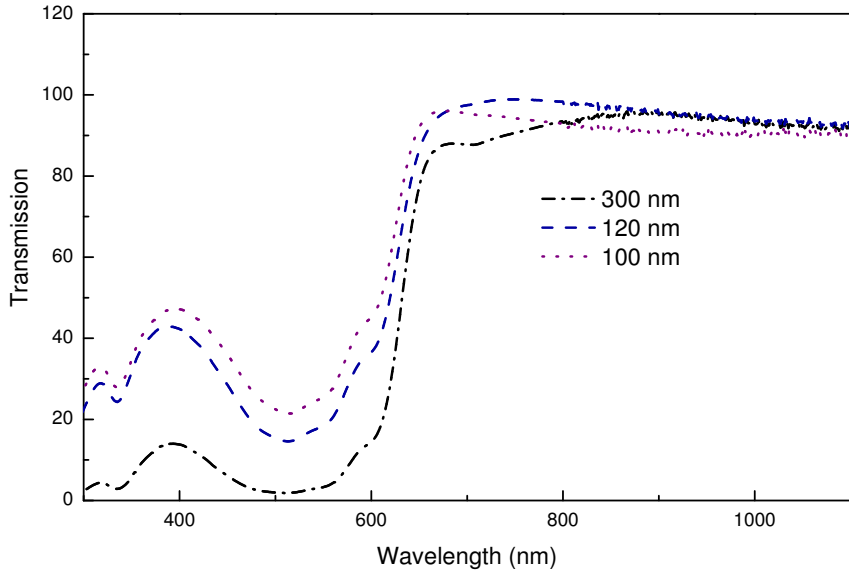


Figure 5.18: UV-Vis-IR transmission spectra for P3HT:C₆₀ samples with three different thicknesses, 100 nm, 120 nm, and 300 nm,

as well. On the other hand, when PEDOT:PSS and LiF layers are eliminated, the active layer thickness dependence is much less noticeable and $\eta_{\text{EQE}}^{\text{L}}$ becomes fairly flat ($0.87 - 0.90$) for the thickness $d_{\text{A}} > 100 \text{ nm}$.

Figure 5.20 shows the measurement results of the EQE as a function of bias voltage and photocurrent at $V = -10 \text{ V}$ as a function of laser intensity at 532 nm, both of which were obtained from I - V characteristics of the device with a thickness $d_{\text{A}} = 300 \text{ nm}$. The value of EQE at short circuit operation is negligibly small because the PEDOT:PSS and LiF layers have been removed. In this case the thickness is considered to be quite large compared to other devices resulting in a small electric field across the device. However, we are primarily interested in the

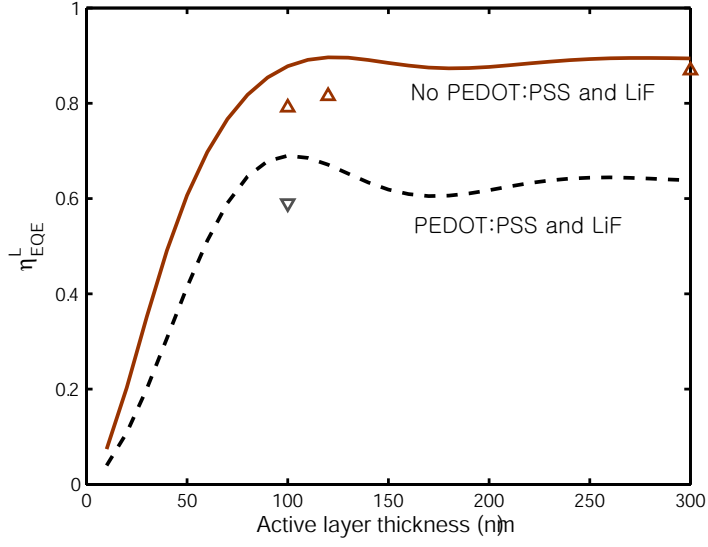


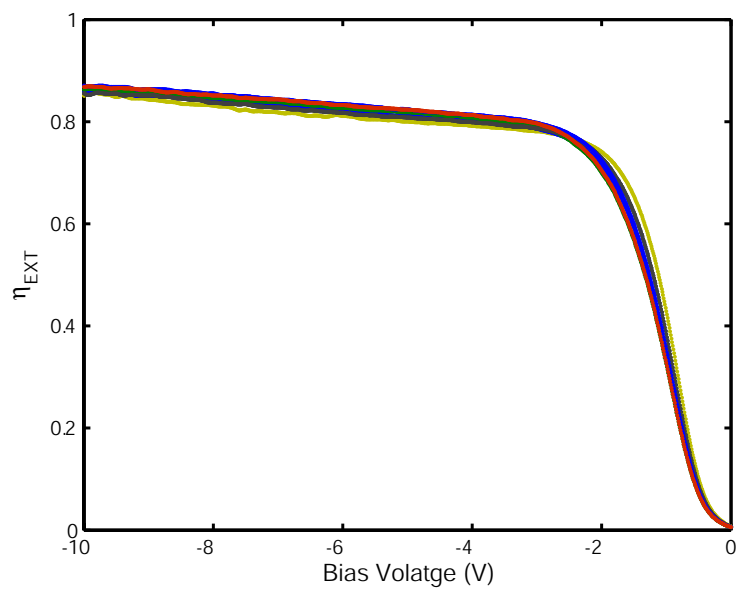
Figure 5.19: Calculated upper limit of the external quantum efficiency $\eta_{\text{EQE}}^{\text{L}}$ as a function of active layer thickness d_{A} (dotted and solid lines) and the measured EQE at bias $V = -10 \text{ V}$ (triangles), with and without PEDOT:PSS and LiF layers.

case that it is under a strong electric field on the order of $\sim 10^7 \text{ V/m}$. Note that, at $V = -10 \text{ V}$, an External quantum efficiency η_{EQE} reaches $87 \pm 2\%$, leading to an internal quantum efficiency $\eta_{\text{IQE}} \approx 97\%$ in this particular example. This indicates that an EQE can indeed reach near $\eta_{\text{EQE}}^{\text{L}}$ and hence a charge collection efficiency across the intervening energy barriers can reach near 100% under a strong electric field. The achieved external quantum efficiency is one of the highest values published so far. Previously, the highest reported values were $\eta_{\text{EQE}} = 75\%$ at $V = -10 \text{ V}$ [91] and $\eta_{\text{EQE}} = 78\%$ at $V = 0 \text{ V}$ [94]. Unfortunately, the full scale dynamic range of the detector could not be investigated due to the limited maximum intensity of the laser, but we did not observe any photocurrent saturation

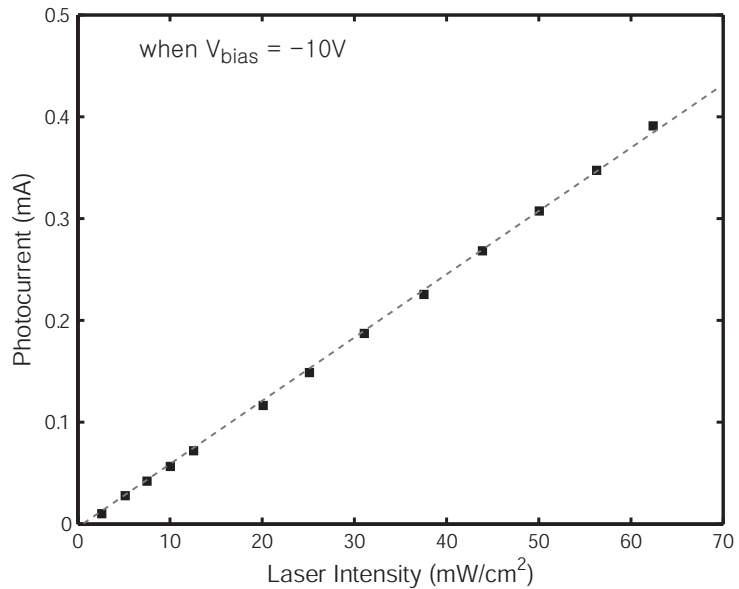
up to an intensity of $I_L = 70 \text{ mW/cm}^2$.

5.6 Summary

In this chapter, we investigated the highly efficient organic thin film bulk heterojunction photodetector fabricated from a blend of conjugated polymer (P3HT) and small molecule (fullerene C₆₀). We have benefited from the ideas developed in the study of OPV cells because the OPD shares fundamental photophysics with the OPV cell in terms of the photocurrent generation process. However, the detector needs a slightly different approach from that used in a photovoltaic cell. We addressed the effect of multilayer thin film interference on the external quantum efficiency. From the numerical modeling to calculate the optical field distribution and absorption of light energy in the layers, based on the characterization of optical properties of individual layers comprising the detector, we proposed a bulk heterojunction photodetector without PEDOT:PSS and LiF layers that are commonly used in photovoltaic cells for high short-circuit current. Through the experimental *I-V* characterization using a CW laser at a wavelength of 532 nm, we demonstrated that it exhibited an external quantum efficiency $\eta_{\text{EQE}} = 87 \pm 2\%$ under an applied bias voltage $V = -10 \text{ V}$, leading to an internal quantum efficiency $\eta_{\text{IQE}} \approx 97\%$. These results show that the charge collection efficiency across the intervening energy barriers can indeed reach near 100% under a strong electric field. The achieved external quantum efficiency is one of the highest values published so far.



(a)



(b)

Figure 5.20: Measured η_{EQE} as a function of applied reverse bias voltage (a) and photocurrent at $V = -10$ V as a function of incident laser intensity (b) for a device with a $d_A = 300$ nm.

CHAPTER 6

CONCLUSIONS

6.1 Summary and accomplishments

This dissertation work was motivated by emerging interests in investigating the technological feasibilities of novel photonic and optoelectronic components fabricated from new classes of organic materials. Due to this nature, the research work was truly a multi-disciplinary subject and has been carried out with a strong collaboration with chemists and physicists. The subject was grouped into three principal parts describing different types of devices that are somewhat independent of each other, but can be integrated into single devices; optical chiral waveguides and magneto-optic materials, waveguides and microring devices from perfluorinated polymer, and organic bulk heterojunction photodetectors from conjugated polymer and fullerene.

First, we studied unique polarization properties of novel organic chiral materials and optical chiral waveguides fabricated from binaphthyl-based chiral single molecular compounds that can be formed into glassy isotropic thin solid films with negligible birefringence. Asymmetric chiral-core planar waveguides were evaluated for viable applications including an integrated-optic polarization rotator. Through

a detailed experimental polarization analysis on the waveguide eigenmodes, we showed that the eigenmodes of the waveguides were indeed elliptically polarized modes with the mode ellipticities on the order of 0.25, which agrees well with the one predicted in the recent theory. The mode ellipticity that we obtained was not large enough to meet the requirement for practical devices such as a polarization rotator – predominant circularly polarized modes – but, to the best of our knowledge, it was the first experimental demonstration of the mode ellipticities of the chiral-core optical waveguides.

We also characterized novel organic magneto-optic materials, which can be viable alternatives to the chiral materials. Measurement of the Verdet constants from organic thin-film samples ($10 - 100 \mu\text{m}$) under a moderate magnetic field can be very challenging and requires a very sensitive measurement technique. We adopted a homodyne balanced detection with a sensitivity that can determine an angle of polarization rotation as small as 0.5×10^{-6} radian and successfully measured the Verdet constants of organic samples provided by Georgia Tech at different wavelengths. We measured Verdet constants of 10.4 and $4.2 \text{ rad}/\text{T} \cdot \text{m}$ at 1300 nm and 1550 nm, respectively, from an organic sample provided by Georgia Tech, which is comparable to that of terbium gallium garnet. This unique observation can lead to a new opportunity to build integrated-optic isolators or circulators from a simple fabrication methodology including spin-casting and photolithography.

Second, we investigated low-loss waveguides and microring resonators fabricated from perfluorocyclobutyl (PFCB) copolymer, which has substantially low

material absorption loss at telecommunication wavelengths. We discussed the design, fabrication, and characterization of those devices. We provided practical design parameters through a waveguide eigenmode analysis, 3-D full vectorial calculation for bending loss estimation, and the coupled mode theory for an estimation of a coupling efficiency. A couple of fabrication challenges, an adhesion and mask cracking problems, were also addressed. From the experimental characterization, we demonstrated the two different types of straight waveguides, a buried channel and pedestal structures, with propagation losses of 0.3 dB/cm and 1.1 dB/cm, respectively. A microring add-drop filter with a maximum extinction ratio of 4.87 dB, quality factor $Q = 8554$, and finesse $\mathcal{F} = 55$ was also demonstrated. In addition, we showed experimentally that all-optical switching with the PFCB microring resonator is possible when it is optically pumped with a femtosecond laser pulse of sufficient energy. For a microring-loaded Mach-Zehnder interferometer (MR-MZI), we demonstrated a modulation window of 30 ps and a maximum modulation depth of 3.8 dB from an optical pump with a pulse duration of 100 fs and a pulse energy of 500 pJ when the signal wavelength is initially tuned to one of the ring resonances.

Finally, we investigated the highly efficient organic bulk heterojunction photodetector fabricated from a blend of conjugated polymer and small molecule, P3HT/PCBM-C₆₀. For a numerical modelling accounting for multilayer interference effects on the external quantum efficiency of a detector, the optical properties and thicknesses of all the individual layers constituting the device were characterized by the spectroscopic ellipsometry and thin film transmission measurement.

Based on the numerical result, we proposed a bulk heterojunction photodetector without containing PEDOT:PSS and LiF layers that are widely used for efficient charge injection in a photovoltaic cell. Experimental I - V characterization at a wavelength of 532 nm exhibited that the external quantum efficiency η_{EQE} could reach near the theoretical upper limit efficiency $\eta_{\text{EQE}}^{\text{L}}$ under a strong electric field. From a P3HT/C₆₀ bulk heterojunction device, we achieved a very high external quantum efficiency $\eta_{\text{EQE}} = 87 \pm 2\%$ leading to an internal quantum efficiency $\eta_{\text{IQE}} \approx 97\%$ under an applied bias voltage $V = -10$ V. These results show that the charge collection efficiency across the intervening energy barriers can indeed reach near 100% under a strong electric field. The achieved external quantum efficiency is one of the highest values obtained so far.

6.2 Future work

We have discussed the technological feasibility of photonic devices based on truly novel organic materials. Therefore, by nature, the work discussed in this thesis is still in progress in many aspects. Most of the materials that were used in this dissertation work are not even commercially available and suffer from incomplete understanding on their physical, optical and electronic properties. By the same token, fabricating devices can be extremely challenging, and sometimes it can take a very long time to develop a new process technique suitable for those materials. Long term reliability is another problem that needs to be resolved for successful commercialization. For these reason, a strong collaboration among engineers,

physicist, and chemist is required.

In order for chiral waveguides to be used as a TE/TM converter or a polarization rotator, the eigenmodes must be predominantly circularly polarized states, achievable by increased material chirality along with negligible birefringence. We showed that, for a given material chirality, the mode ellipticity in a weakly guided waveguide is much higher than a tightly confined waveguide. However, for nearly circularly modes, a chirality at least an order magnitude larger ($\gamma \approx 4\text{ pm}$ or equivalently, bulk $\rho = 60\text{ deg/mm}$) than the one we presented is required. It is also desirable to extend the ORD maxima towards the telecommunication wavelengths for optical communication applications. Certain types of chiral compounds are very sensitive to UV light and they tend to racemize in the air. Therefore, solutions to this photoracemization need to be addressed as well in the future. It should not be an easy task, but developing a numerical technique to analyze the eigenmode and the mode ellipticity in 3D guiding structures can provide a very useful tool for designing a practical integrated optic chiral devices.

The Verdet constants from organic materials we observed were moderate, but this unique observation opens the possibility that integrated optic isolators or circulators can easily be constructed from a simple fabrication methodology including spin-casting and photolithography. However, in order to build practical devices, much work needs to be done to synthesize the materials with even larger Verdet constants, and to investigate the polarization properties of the eigenmodes in magneto-optic waveguides. In addition, a comprehensive theoretical study in-

cluding a quantum mechanical approach is needed to understand the origin of the large Verdet constants from organic materials.

More theoretical and experimental investigation is necessary for the PFCB-based waveguide devices. Although we did not discuss the numerical techniques to calculate the scattering loss, it can be done by modifying our finite difference code properly to employ a radiative scattering source. Aside from achieving a narrower gap, much needs to be done to refine the etch process in order to reduce the scattering loss, which is a dominant source increasing the total loss in the PFCB waveguides. A different etching condition in RIE, or different etching tools including an inductive coupled plasma etching (ICP) can be tried. A post-etching process such as chemical or thermal treatment may allow us to achieve much smoother side wall. In addition, adhesion of fluorinated polymer to other layers can be further improved by, for example, plasma surface treatment, and stress arising from the CTE mismatch can be further eliminated. Other classes of novel materials including electro-optic, semiconducting, and 3rd order nonlinear optical polymer can be used to construct a ring resonator to exploit its multiple device functionality.

Finally, for the development of organic photodetectors, other detector characteristics such as dark current, noise equivalent power, dynamic range, response time needs to be investigated. For long-term reliability, incorporating the encapsulation technology developed for commercial OLEDs needs to be done for practical use. A detector with a high photoresponsivity at infra-red wavelengths is worth

investigating. In particular, more advanced types of devices such as a travelling-wave photodetector fabricated with a low loss polymer waveguide is certainly one of the most interesting possible future developments.

I described several possible directions for future research, but potentially useful devices from organic materials are limited only by the imagination. Didn't I mention that we are already living in the "PLASTIC" world? The future is about to unfold.

BIBLIOGRAPHY

- [1] L. Eldada, “Optical communication components,” *Review of Scientific Instruments*, vol. 75, no. 3, pp. 575–593, 2004.
- [2] H. Ma, K. Y. Jen, and L. R. Dalton, “Polymer-based optical waveguides: Materials, processing, and devices.” *Advanced Materials*, vol. 14, no. 19, pp. 1339–1365, 2002.
- [3] A. J. Heeger, “Nobel lecture: Semiconducting and metallic polymers: The fourth generation of polymeric materials,” *Reviews of Modern Physics*, vol. 73, no. 3, pp. 681–700, 2001.
- [4] S. R. Forrest, “The path to ubiquitous and low-cost organic electronic appliances on plastic,” *Nature*, vol. 428, no. 6986, pp. 911–918, 2004.
- [5] J. McMurry, *Organic Chemistry*, 5th ed. Pacific Grove: Brooks/Cole, 1999.
- [6] N. M. Davies and X. W. Teng, “Importance of chirality in drug therapy and pharmacy practice: Implications for psychiatry,” *Advances in Pharmacy*, vol. 1, no. 3, pp. 242–252, 2003.
- [7] S. F. Mason, “Optical activity and molecular dissymmetry,” *Contemporary physics*, vol. 9, no. 3, pp. 239–256, 1968.

- [8] W. N. Herman, “Polarization eccentricity of the transverse field for modes in chiral core planar waveguides,” *Journal of Optical Society of America, A*, vol. 18, no. 11, pp. 2806–2818, 2001.
- [9] C. Nuckolls, T. J. Katz, G. Katz, P. J. Collings, and L. Castellanos, “Synthesis and aggregation of a conjugated helical molecule.” *Journal of American Chemical Society*, vol. 121, no. 1, pp. 79–88, 1999.
- [10] J. D. Jackson, *Classical Electrodynamics*, 3rd ed. New York: Jone Wiley & Sons, 1999.
- [11] M. P. Silverman, “Refection and refraction at the surface of a chiral medium: comparison of gyrotropic constitutive relations invariant or noninvariant under a duality transformation,” *Journal of Optical Society of America, A*, vol. 3, no. 6, pp. 830–837, 1986.
- [12] J. Lekner, “Optical properties of isotropic chiral media,” *Pure and Applied Optics*, vol. 5, no. 4, pp. 417–443, 1996.
- [13] I. V. Lindell, A. H. Sihvola, S. A. Tretyakov, and A. J. Vitanen, *Electromagnetic Waves in Chiral and Bi-Isotropic Media*, Boston, 1994.
- [14] D. Marcuse, *Theory of Dielectric Optical Waveguides*, 2nd ed. San Diego: Academic Press, 1991.

- [15] S. V. Demidov, K. V. Kushnarev, and V. V. Shevchenko, “Dispersion properties of the modes of chiral planar optical waveguides,” *Journal of Communications Technology and Electronics*, vol. 44, no. 7, pp. 827–832, 1999.
- [16] M. Oksanen, P. K. Loivisto, and I. V. Lindell, “Dispersion curves and fields for a chiral slab waveguide,” *IEE Proceedings H*, vol. 138, no. 4, pp. 327–334, 1991.
- [17] F. Y. Fan, J. C. Mastrangelo, D. Katsis, S. H. Chen, and T. N. Blanton, “Novel glass forming liquid crystals V. Nematic and chiral-neumatic systems with an elevated glass-transition temperature.” *Liquid Crystals*, vol. 27, no. 9, pp. 1239–1248, 2000.
- [18] J.-. W. Park, M. D. Ediger, and M. M. Green, “Chiral studies in amorphous solids: The effect of the polymeric glassy state on the racemization kinetics of bridged paddled binaphthyls.” *Journal of Americal Chemical Society*, vol. 123, no. 1, pp. 49–56, 2001.
- [19] W. N. Herman, Y. Kim, W. L. Cao, J. Goldhar, C. H. Lee, M. M. Green, V. Jain, and M. J. Lee, “Amorphous thin films of chiral binaphthyls for photonic waveguides,” *Journal of Macromolecular Science Part A - Pure and Applied Chemistry*, vol. A40, no. 12, pp. 1369–1382, 2003.
- [20] G. D. Van Wiggeren and R. Roy, “High-speed fiber-optic polarization analyzer, measurements of the polarization dynamics of an erbium-doped fiber

- ring laser,” *Optical Communications*, vol. 164, pp. 107–120, 1999.
- [21] S. T. Tang and H. S. Kwok, “ 3×3 matrix for unitary optical systems,” *Journal of Optical Society of America, A*, vol. 18, no. 9, pp. 2138–2145, 2001.
- [22] Y. P. Svirko and N. Zheludev, *Polarization of Light in Nonlinear Optics*. New York: John Wiley & Sons, 1998.
- [23] M. M. Green, “Personal communications.”
- [24] M. Miyasaka, A. Rajca, M. Pink, and S. Rajca, “Chiral molecular glass: Synthesis and characterization of enantiomerically pure thiophene-based [7]heptalene,” *Chemistry - A European Journal*, vol. 10, no. 24, pp. 6531–6539, 2004.
- [25] A. D. Villaverde, D. A. Donatti, and D. Bozinis, “Terbium gallium garnet Verdet constant measurement with pulsed magnetic field,” *Journal of Physics C: Solid State Physics*, vol. 11, pp. L495–498, 1978.
- [26] P. A. Williams, A. H. Rose, G. W. Day, T. E. Milner, and M. N. Deeter, “Temperature dependence of the Verdet constant in several diamagnetic glasses,” *Applied Optics*, vol. 30, no. 10, pp. 1176–1178, 1991.
- [27] N. P. Barnes and L. B. Petway, “Variation of the Verdet constant with temperature of terbium gallium garnet,” *Journal of Optical Society of America, B*, vol. 9, no. 10, pp. 1912–1915, 1992.

- [28] E. Hecht, *Optics*, 4th ed. Addison Wesley Longman, Inc., 2002.
- [29] W. Kaminsky, “Experimental and phenomenological aspects of circular birefringence and related properties in transparent crystals,” *Reports on Progress in Physics*, vol. 63, pp. 1575–1640, 2000.
- [30] R. J. Potton, “Reciprocity in optics,” *Reports on Progress in Physics*, vol. 67, pp. 717–754, 2004.
- [31] G. Koeckelberghs, T. Foerier, T. Verbiest, and A. P. Persoons, “Chirality and magnetic aspects of molecular nonlinear optics,” *Proceedings of SPIE*, vol. 5935, 2005.
- [32] O. Brevet-Philibert, R. Brunetton, and J. Monin, “Measuring the Verdet constant: A simple, high precision, automatic device,” *Journal of physics E: Scientific Instruments*, vol. 21, pp. 647–649, 1988.
- [33] A. Jain, J. Kumar, F. Zhou, L. Li, and S. Tripathy, “A simple experiment for determining Verdet constants using alternating current magnetic fields,” *American Journal of Physics*, vol. 67, no. 8, pp. 714–717, 1999.
- [34] C. C. Davis, “Building small, extremely sensitive practical interferometers for sensor applications,” *Nuclear Physics B*, vol. 6, pp. 290–297, 1989.
- [35] K. Cho, S. P. Bush, D. L. Mazzoni, and C. C. Davis, “Linear magnetic birefringence measurement of Faraday materials,” *Physical Review B*, vol. 43, no. 1, pp. 965–971, 1991.

- [36] C. C. Davis, *Lasers and Electro-Optics, Fundamentals and Engineering*. Cambridge: Cambridge University Press, 1996.
- [37] A. Yariv, *Optical Electronics in Modern Communications*, 5th ed. New York: Oxford University Press, 1996.
- [38] M. Jhou, “Low-loss polymeric materials for passive waveguide components in fiber optical telecommunication,” *Optical Engineering*, vol. 41, no. 7, pp. 1631–1643, 2002.
- [39] L. Eldada and L. W. Shacklette, “Advances in polymer integrated optics,” *IEEE Journal of Selected Topics in Quantum Electronics*, vol. 6, no. 1, pp. 54–68, 2000.
- [40] S. M. Garner, V. Chuanov, S.-S. Lee, A. Chen, W. H. Steier, and L. R. Dalton, “Vertically integrated waveguide polarization splitters using polymers,” *IEEE, Photonics Technology Letters*, vol. 11, no. 7, pp. 842–844, 1999.
- [41] Y. Wang, Y. Abe, Y. Matsuura, M. Miyagi, and H. Uyama, “Refractive indices and extinction coefficients of polymers for the mid-infrared region,” *Applied Optics*, vol. 37, no. 30, pp. 7091–7095, 1998.
- [42] D. W. Smith Jr., S. Chen, S. M. Kumar, J. Ballato, C. Topping, H. V. Shah, and S. Foulger, “Perfluorocyclobutyl copolymers for microphtotonics,” *Advanced Materials*, vol. 14, no. 21, pp. 1585–1589, 2002.

- [43] J. Ballato, S. Foulger, and D. W. Smith Jr., “Optical properties of perfluorocyclobutyl polymers,” *Journal of Optical Society of America, B*, vol. 20, no. 9, pp. 1838–1843, 2003.
- [44] J. Ballato, S. H. Foulger, and D. W. Smith Jr., “Optical properties of perfluorocyclobutyl polymers. II. theoretical and experimental attenuation,” *Journal of Optical Society of America, B*, vol. 21, no. 5, pp. 958–967, 2004.
- [45] B. M. A. Raman and J. B. Davies, “Vector-H finite element solution of GaAs/GaAlAs rib waveguides,” *IEE Proceedings J*, vol. 132, no. 6, pp. 349–353, 1985.
- [46] Z.-E. Abid, K. L. Johnson, and A. Gopinath, “Analysis of dielectric guides by vector transverse magnetic finite elements,” *Journal of Lightwave Technology*, vol. 11, no. 10, pp. 1545–1549, 1993.
- [47] C. L. Xu, W. P. Huang, M. S. Stern, and S. K. Chaudhuri, “Full-vectorial mode calculations by finite difference method,” *IEE Proceedings J*, vol. 141, no. 5, pp. 281–286, 1994.
- [48] S. Sujecki, T. M. Benson, P. Sewell, and P. C. Kendall, “Novel vectorial analysis of optical waveguides,” *Journal of Lightwave Technology*, vol. 16, no. 7, pp. 1329–1335, 1998.

- [49] M. D. Feit and J. A. Flecker Jr, “Computation of mode properties in optical fiber waveguides by a propagation beam method,” *Applied Optics*, vol. 19, pp. 1154–1164, 1980.
- [50] D. Yevick and B. Hermansson, “New formulations of the matrix beam propagation method: application to rib waveguides,” *IEEE Journal of Quantum Electronics*, vol. 25, no. 2, pp. 221–229, 1989.
- [51] C. L. Xu, W. P. Huang, and S. K. Chaudhuri, “Efficient and accurate vector mode calculations by beam propagation method,” *Journal of Lightwave Technology*, vol. 11, no. 7, pp. 1209–1215, 1993.
- [52] T. E. Murphy, “Design, fabrication and measurement of integrated bragg grating optical filters,” Ph.D, Massachusetts Institute of Technology, 2001.
- [53] A. W. Snyder and J. D. Love, *Optical Waveguide Theory*, 1st ed. London: Chapman and Hall, Ltd., 1983.
- [54] R. R. Rye, A. J. Howard, and A. J. Ricco, “Photolithographic metallization of fluorinated polymers,” *Thin Solid Films*, vol. 262, no. 1-2, pp. 73–83, 1995.
- [55] K. Tanaka, T. Inomata, and M. Kogoma, “Improvement in adhesive strength of fluorinated polymer films by atmospheric pressure glow plasma,” *Thin Solid Films*, vol. 386, no. 2, pp. 217–221, 2001.
- [56] Form No. 618-00200-498, *Processing procedures for Dry-Etch CYCLOTENE Advanced Electronics Resins (Dry-Etch BCB)*. Dow Chemical Co.

- [57] R. G. Hunsperger, *Integrate Optics: Theory and Technology*, 4th ed. New York: Springer, 1995.
- [58] M. Haruna, Y. Segawa, and H. Nishihara, “Nondestructive and simple method of optical waveguide loss measurement with optimisation of end-fire coupling.” *Electronics Letters*, vol. 28, no. 17, pp. 1612–1613, 1992.
- [59] R. G. Walker, “Simple and accurate loss measurement technique for semiconductor optical waveguides,” *Electronics Letters*, vol. 21, no. 13, pp. 581–583, 1985.
- [60] R. J. Deri and E. Kapon, “Low loss III-V semiconductor optical waveguides,” *IEEE Journal of Quantum Electronics*, vol. 27, no. 3, pp. 626–640, 1991.
- [61] N. Agarwal, S. Ponoth, J. Plawsky, and P. D. Persans, “Optimized oxygen plasma etching of polyimide films for low loss optical waveguides,” *Journal of Vacuum Science and Technology A: Vacuum, Surfaces, and Films*, vol. 20, no. 5, pp. 1587–1591, 2002.
- [62] T. Barwicz and H. A. Haus, “Three-dimensional analysis of scattering losses due to sidewall roughness in microphotonic waveguides,” *IEEE Journal of Lightwave Technology*, vol. 23, no. 9, pp. 2719–2732, 2005.
- [63] T. Alder, A. Stohr, R. Heinzelmann, and D. Jager, “High-efficiency fiber-to-chip coupling using low-loss tapered single-mode fiber,” *IEEE Photonics Technology Letters*, vol. 12, no. 8, pp. 1016–1018, 2000.

- [64] K. J. Vahala, “Optical microcavities,” *Nature*, vol. 424, no. 6950, pp. 839–846, 2003.
- [65] B. E. Little, S. T. Chu, H. A. Haus, J. Foresi, and J. P. Laine, “Microring resonator channel dropping filters,” *Journal of Lightwave Technology*, vol. 15, no. 6, pp. 998–1005, 1997.
- [66] P. P. Absil, J. V. Hryniewicz, B. E. Little, R. A. Wilson, L. G. Joneckis, and P.-T. Ho, “Compact microring notch filters,” *IEEE Photonics Technology Letters*, vol. 12, no. 4, pp. 398–400, 2000.
- [67] J. E. Heebner, “Nonlinear optical whispering gallery microresonators for photonics,” Ph.D. dissertation, University of Rochester, 2003.
- [68] R. Grover, “Indium phosphide based optical micro-ring resonators.” Ph.D., University of Maryland, College Park, 2003.
- [69] H. A. Haus, *Waves and Fields in Optoelectronics*. Englewood Cliffs: Prentice-Hall, Inc., 1984.
- [70] D. Marcuse, “Bend loss of slab and fiber modes computed with diffraction theory,” *IEEE Journal of Quantum Electronics*, vol. 29, no. 12, pp. 2957–2961, 1993.
- [71] T. E. Murphy, “Personal communications.”

- [72] N.-. N. Feng, G.-. R. Zhou, C. Xu, and W. P. Huang, “Computation of full-vector modes for bending waveguide using cylindrical perfectly matched layers,” *IEEE Journal of Lightwave Technology*, vol. 20, no. 11, pp. 1976–1980, 2002.
- [73] W. P. Huang, C. L. Xu, and K. Yokoyama, “The perfectly matched layer boundary condition for modal analysis of optical waveguides: Leaky mode calculations,” *IEEE Photonics Technology Letters*, vol. 8, no. 5, pp. 652–654, 1996.
- [74] H. A. Haus, W. P. Huang, S. Kawakami, and N. A. Whitaker, “Coupled-mode theory of optical waveguides,” *Journal of Lightwave Technology*, vol. LT-5, no. 1, pp. 16–23, 1987.
- [75] W. Y. Chen, R. Grover, T. A. Ibrahim, V. Van, W. N. Herman, and P. T. Ho, “High-finesse laterally coupled single-mode benzocyclobutene microring resonators,” *IEEE Photonics Technology Letters*, vol. 16, no. 2, pp. 470–472, 2004.
- [76] W. Cao, W. Y. Chen, J. Goldhar, P. T. Ho, W. N. Herman, and C. H. Lee, “Optical bistability and picosecond optical switching in bisbenzocyclobutene (BCB) polymer microring resonators,” in *Optical Fiber Communication Conference, 2004.*, 2004.

- [77] C. H. Lee, P. S. Mak, and A. P. DeFonzo, “Optical control of millimeter-wave propagation in dielectric waveguides,” *IEEE Journal of Quantum Electronics*, vol. QE-16, no. 3, pp. 277–288, 1980.
- [78] C. H. Lee, *Picosecond Optoelectronic Devices*. London: Academic Press, 1984.
- [79] V. Van, T. A. Ibrahim, K. Ritter, P. P. Absil, F. G. Johnson, R. Grover, J. Goldhar, and P. T. Ho, “All-optical nonlinear switching in GaAs-AlGaAs microring resonators,” *IEEE Photonics Technology Letters*, vol. 14, no. 1, pp. 74–76, 2002.
- [80] V. Van, T. A. Ibrahim, P. P. Absil, F. G. Johnson, R. Grover, and P. T. Ho, “Optical signal processing using nonlinear semiconductor microring resonators,” *IEEE Journal of Selected Topics in Quantum Electronics*, vol. 8, no. 3, pp. 705–713, 2002.
- [81] T. A. Ibrahim, W. Cao, Y. Kim, J. Li, J. Goldhar, P. T. Ho, and C. H. Lee, “All-optical switching in a laterally coupled microring resonator by carrier injection,” *IEEE Photonics Technology Letters*, vol. 15, no. 1, pp. 36–38, 2003.
- [82] W. Cao, M. Du, Y. Kim, W. N. Herman, and C. H. Lee, “Ultrafast transient photoconductivity of bisbenzocyclobutene (BCB) polymer films,” in *OSA, Ultrafast Electronics and Optoelectronics*, 2003, pp. 49–52.

- [83] T. A. Ibrahim, W. Cao, Y. Kim, J. Li, J. Goldhar, P. T. Ho, and C. H. Lee, “Lightwave switching in semiconductor microring devices by free carrier injection,” *IEEE Journal of Lightwave Technology*, vol. 21, no. 12, pp. 2997–3003, 2003.
- [84] V. Van, W. N. Herman, and H. Ping-Tong, “Linearized microring-loaded Mach-Zehnder modulator with RF gain,” *Journal of Lightwave Technology*, vol. 24, no. 4, pp. 1850–1854, 2006.
- [85] J. H. Burroughes, D. D. C. Bradley, A. R. Brown, A. R. Marks, K. Mackay, R. H. Friend, P. L. Burns, and A. B. Holmes, “Light-emitting diodes based on conjugated polymers,” *Nature*, vol. 347, no. 6293, pp. 539–541, 1990.
- [86] D. Braun and A. J. Heeger, “Visible light emission from semiconducting polymer diodes,” *Applied Physics Letters*, vol. 58, no. 18, pp. 1982–1984, 1991.
- [87] C. W. Tang, “Two-layer organic photovoltaic cell,” *Applied Physics Letters*, vol. 48, no. 2, pp. 183–185, 1986.
- [88] D. Wohrle and D. Meissner, “Organic solar cells,” *Advanced Materials*, vol. 3, no. 3, pp. 129–138, 1991.
- [89] C. J. Brabec, N. S. Sariciftci, and J. C. Hummelen, “Plastic solar cells,” *Advanced Functional Materials*, vol. 11, no. 1, pp. 15–26, 2001.

- [90] H. Hoppe and N. S. Sariciftci, “Organic solar cells: An overview,” *Journal of Material Research*, vol. 19, no. 7, pp. 1924–1945, 2004.
- [91] P. Peumans, A. Yakimov, and S. R. Forrest, “Small molecular weight organic thin-film photodetectors and solar cells,” *Journal of Applied Physics*, vol. 93, no. 7, pp. 3693–3723, 2003.
- [92] P. Schilinsky, C. Waldauf, and C. J. Brabec, “Recombination and loss analysis in polythiophene based bulk heterojunction photodetectors,” *Applied Physics Letters*, vol. 81, no. 20, pp. 3885–3887, 2002.
- [93] G. Yu, Y. Cao, J. Wang, J. McElvain, and A. J. Heeger, “High sensitivity polymer photosensors for image sensing applications,” *Synthetic Metals*, vol. 102, no. 1-3, pp. 904–907, 1999.
- [94] P. Schilinsky, C. Waldauf, J. Hauch, and C. J. Brabec, “Polymer photovoltaic detectors: progress and recent developments,” *Thin Solid Films*, vol. 451-452, pp. 105–108, 2004.
- [95] A. Tsumura, H. Koezuka, and T. Ando, “Macromolecular electronic device: Field-effect transistor with a polythiophene thin film,” *Applied Physics Letters*, vol. 49, no. 18, pp. 1210–1212, 1986.
- [96] F. Ebisawa, T. Kurokawa, and S. Nara, “Electrical properties of polyacetylene/polysiloxane interface,” *Journal of Applied Physics*, vol. 54, no. 6, pp. 3255–3259, 1983.

- [97] J. H. Burroughes, C. A. Jones, and R. H. Friend, “New semiconductor device physics in polymer diodes and transitors,” *Nature*, vol. 335, no. 6186, pp. 137–141, 1988.
- [98] T. W. Kelley, D. V. Muyres, P. F. Baude, T. P. Smith, and T. D. Jones, “High performance organic thin film transistor,” in *Material Research Society Symposium Proceeding*, vol. 771, 2003, pp. L6.5.1–L6.5.11.
- [99] J. J. M. Halls, K. Pichler, R. H. Friend, S. C. Moratti, and A. B. Holmes, “Exciton diffusion and dissociation in a poly(p-phenylenevinylene)/C₆₀ heterojunction photovoltaic cell,” *Applied Physics Letters*, vol. 68, no. 22, pp. 3120–3122, 1996.
- [100] T. Stubinger and W. Brutting, “Exciton diffusion and optical interference in organic donor–acceptor photovoltaic cells,” *Journal of Applied Physics*, vol. 90, no. 7, pp. 3632–3641, 2001.
- [101] L. A. A. Pettersson, L. S. Roman, and O. Inganäs, “Modeling photocurrent action spectra of photovoltaic devices based on organic thin films,” *Journal of Applied Physics*, vol. 86, no. 1, pp. 487–496, 1999.
- [102] N. S. Sariciftci, L. Smilowitz, A. J. Heeger, and F. Wudl, “Photoinduced electron transfer from a conducting polymer to buckminsterfullerene,” *Science*, vol. 258, no. 5087, pp. 1474–1476, 1992.

- [103] C. H. Lee, G. Yu, and A. J. Heeger, “Persistent photoconductivity in poly(p-phenylenevinylene): Spectral response and slow relaxation,” *Physical Review B*, vol. 47, no. 23, pp. 15 543–15 553, 1993.
- [104] L. Smilowitz, N. S. Sariciftci, R. Wu, C. Gettinger, A. J. Heeger, and F. Wudl, “Photoexcitation spectroscopy of conducting-polymer/C₆₀ composites: Photoinduced electron transfer,” *Physical Review B*, vol. 47, no. 20, pp. 13 835–13 842, 1993.
- [105] K. Lee, R. A. J. Janssen, N. S. Sariciftci, and A. J. Heeger, “Direct evidence of photoinduced electron transfer in conducting-polymer C₆₀ composites by infrared photoexcitation spectroscopy,” *Physical Review B*, vol. 49, no. 8, pp. 5781–5784, 1994.
- [106] B. Kraabel, D. McBranch, N. S. Sariciftci, D. Moses, and A. J. Heeger, “Ultrafast spectroscopic studies of photoinduced electron transfer from semiconducting polymers to C₆₀,” *Physical Review B*, vol. 50, no. 24, pp. 18 543–18 552, 1994.
- [107] M. C. J. M. Vissenberg and M. Matters, “Theory of the field-effect mobility in amorphous organic transistors,” *Physical Review B*, vol. 57, no. 20, pp. 12 964–12 967, 1998.
- [108] J. S. Kim, R. H. Friend, and F. Cacialli, “Improved operational stability of polyfluorene-based organic light-emitting diodes with plasma-treated

- indium–tin–oxide anodes,” *Applied Physics Letters*, vol. 74, no. 21, pp. 3084–3086, 1999.
- [109] T. M. Brown, J. S. Kim, R. H. Friend, F. Cacialli, R. Daik, and W. J. Feast, “Built-in field electroabsorption spectroscopy of polymer light-emitting diodes incorporating a doped poly(3,4-ethylene dioxythiophene) hole injection layer,” *Applied Physics Letters*, vol. 75, no. 12, pp. 1679–1681, 1999.
- [110] P. K. H. Ho, J.-S. Kim, J. H. Burroughes, H. Becker, S. F. Y. Li, T. M. Brown, F. Cacialli, and R. H. Friend, “Molecular-scale interface engineering for polymer light-emitting diodes,” *Nature*, vol. 404, no. 6777, pp. 481–484, 2000.
- [111] S. E. Shaheen, C. J. Brabec, N. S. Sariciftci, F. Padinger, T. Fromherz, and J. C. Hummelen, “2.5% efficient organic plastic solar cells,” *Applied Physics Letters*, vol. 78, no. 6, p. 841, 2001.
- [112] R. P. Barber, M. Breban, R. D. Gomez, W. N. Herman, and D. B. Romero, “Organic photocells based on block copolymer /C₆₀ blends,” *Proceedings of SPIE*, vol. 5938, pp. 341–348, 2005.
- [113] R. P. Barber, R. D. Gomez, W. N. Herman, and D. B. Romero, “Characterization of organic photovoltaic devices based on a block copolymer / fullerene blend,” *Organic Electronics*, to appear.

- [114] L. S. Hung, C. W. Tang, and M. G. Mason, “Enhanced electron injection in organic electroluminescence devices using an Al/LiF electrode,” *Applied Physics Letters*, vol. 70, no. 2, p. 152, 1997.
- [115] G. E. Jabbour, Y. Kawabe, S. E. Shaheen, J. F. Wang, M. M. Morrell, B. Kippelen, and N. Peyghambarian, “Highly efficient and bright organic electroluminescent devices with an aluminum cathode,” *Applied Physics Letters*, vol. 71, no. 13, pp. 1762–1764, 1997.
- [116] A. L. Farrenbruch and R. H. Bube, *Fundamentals of Solar Cells: Photovoltaic Solar Energy Conversion*. San Diego: Academic Press, 1983.
- [117] A. D. Rakic, A. B. Djurisic, J. M. Elazar, and M. L. Majewski, “Optical properties of metallic films for vertical-cavity optoelectronic devices,” *Applied Optics*, vol. 37, no. 22, pp. 5271–5283, 1998.
- [118] M. A. Ordal, L. L. Long, R. J. Bell, S. E. Bell, R. R. Bell, R. R. Alexander, and C. A. Ward, “Optical properties of the metals Al, Co, Cu, Au, Fe, Pb, Ni, Pd, Pt, Ag, Ti, and W in the infrared and far infrared,” *Applied Optics*, vol. 22, no. 7, pp. 1099–1120, 1983.
- [119] R. A. Synowicki, “Spectroscopic ellipsometry characterization of indium tin oxide film microstructure and optical constants,” *Thin Solid Films*, vol. 313-314, pp. 394–397, 1998.

- [120] A. K. Ghosh and T. Feng, “Merocyanine organic solar cells,” *Journal of Applied Physics*, vol. 49, no. 12, p. 5982, 1978.
- [121] A. Desormeaux, J. J. Max, and R. M. Leblane, “Photovoltaic and electrical properties of Al/Langmuir-Blodgett Films/Ag sandwich cells incorporating either chlorophyll a, chlorophyll b, or zinc porphyrin derivative,” *Journal of Physical Chemistry*, vol. 97, pp. 6670–6678, 1993.
- [122] S. M. Sze, *Physics of Semiconductor Devices*. New York: Jone Wiley & Sons, 1981, vol. 2nd.
- [123] L. J. A. Koster, E. C. P. Smits, V. D. Mihailetti, and P. W. M. Blom, “Device model for the operation of polymer/fullerene bulk heterojunction solar cells,” *Physical Review B (Condensed Matter and Materials Physics)*, vol. 72, no. 8, 2005.

